Head Motion Artifacts in Functional Imaging-based Brain Connectivity Analysis

Ph.D. thesis

Tamás Spisák

Supervisor: Dr. Miklós Emri

University of Debrecen

Doctoral Committee of Natural Sciences
Doctoral School of Computer Sciences

Department of Nuclear Medicine

Debrecen, 2015.

Ezen értekezést a Debreceni Egyetem Természettudományi Doktori Tanács Informatikai Tudományok Doktori Iskola ”Az informatika ipari és tudományos alkalmazásai” programja keretében készítettem a Debreceni Egyetem természettudományi doktori (PhD) fokozatának elnyerése céljából.

Debrecen, 2015.
....
Spisák Tamás
jelölt

Tanúsítom, hogy Spisák Tamás doktorjelölt 2011 - 2015. között a fent megnevezett Doktori Iskola ”Az informatika ipari és tudományos alkalmazásai” programjának keretében irányításommal végezte munkáját. Az értekezésben foglalt eredményekhez a jelölt önálló alkotó tevékenységével meghatározóan hozzájárult. Az értekezés elfogadását javasolom.

Debrecen, 2015.
....
Dr. Emri Miklós
témavezető

Head Motion Artifacts in Functional Imaging-based Brain Connectivity Analysis

Értekezés a doktori (Ph.D.) fokozat megszerzése érdekében az
informatika tudományágban

Írta: Spisák Tamás okleveles programtervező matematikus

Készült a Debreceni Egyetem Informatikai Tudományok doktori
iskolája "Az informatika ipari és tudományos alkalmazásai"
programja keretében

Témavezető: Dr. Emri Mikós

A doktori szigorlati bizottság:

elnök: Dr. ....
tagok Dr. ....
Dr. ....

A doktori szigorlat időpontja: 2015. ... ...

Az értekezés bírálói:

Dr. Hajdu András ....
Dr. Gál Viktor ....

A bírálóbizottság:

elnök: Dr. ....
tagok Dr. ....
Dr. ....
Dr. ....
Dr. ....

Az értekezés védésének időpontja: 2015. ... ...

Contents

List of Figures

List of Tables

Abbreviations

BOLD	**B**lood-**O**xygen-**L**evel **D**ependent
CBF	**C**erebral **B**lood **F**low
CBV	**C**erebral **B**lood **V**olume
CMRO$_2$	**C**erebral **M**etabolic **R**ate of **O**xygen
CCPR	**C**omponent and **C**omponent-**P**lus-**R**esidual plot
COMPCOR	**COMP**onent based noise **COR**rection
DVARS	temporal **D**erivate of RMS signal **VAR**iance
FD	**F**rame-wise **D**isplacement
FDR	**F**alse **D**iscovery **R**ate
fMRI	**f**unctional **M**agnetic **R**esonance **I**maging
GLM	**G**eneralized **L**inear **M**odel
GSREG	**G**lobal **S**ignal **REG**ression
HPC	**H**igh-**P**erformance **C**omputing
M3I	**M**ultimodal**M**edical **I**maging software library system
MVC	**M**odel-**V**iew-**C**ontroller design pattern
M6	regression of **6** **M**otion parameters
NOREG	**NO** nuisance signal **REG**ression
RD	**R**egional **D**isplacement
RDI	**R**egional **D**isplacement **I**nteraction
ROI	**R**egion **O**f **I**nterest
rs-fcMRI	**r**esting-**s**tate **fMRI** **c**onnectivity
SAT36	**SAT**terthwaite **36**-parameter correction model
SPN	**S**tatistical **P**arametric **N**etwork
TR	**T**ime of **R**epetition
VIF	**V**ariance **I**nflation **F**actor
WMCSF	regression of **W**hite **M**atter and **C**elebro**S**pinal **F**luid signal

1 Introduction

> *"The whole is greater than the sum of its parts"*
> */Aristotle [1]/*

> *"The brain is more than the sum of its parts"*
> */ Munakata [2]; following Aristotle /*

The human brain is one of the most complex known systems [3] which produces a staggering cognitive capacity and a wide variety of human behavior. As a network of interacting neurons and cortical units, a cornerstone of its understanding might be the theory of complex networks which went through an extraordinary development in the past decades [4–6]. This novel concept has been proven to be effective in characterizing complex systems [7] like various social (e-mail, social network sites [8]), economical (stock ex-change [9]), technological (world wide web, internet [10]) and biological (genetics, genomics, cell metabolism [11]) networks. Despite the classical "localizationist" paradigm which aims to assign functions of the brain to its distinct parts, the concept of "connectivity" explains cognitive processes by network patterns of interconnected and synchronously operating ("integration"), but, at the same time autonomous neural entities ("segregation"). Thus, in case of pathological conditions characterized by dysfunction of brain, the focus sets on the role of the malformation within the whole network instead of its spatial location [12]. This novel concept, besides studies aiming to understand the healthy functioning brain, showed significant remarkable results in examining diseases like sclerosis multiplex [13], schizophrenia [14], autism [15–17] and epilepsy [18–21], Alzheimer's [22, 23] and Parkinson's disease [24].

In the past decades, the dynamic development of brain imaging techniques has provided the opportunity for the in-vivo non invasive examination of the anatomical and physiological properties of the brain. While structural or anatomical connections ("highways") can be investigated, for instance, by Diffusion Tensor Imaging (DTI), functional networks ("traffic on the highways") can be mapped among others by functional Magnetic Resonance Imaging (fMRI) or electro- and magnetoencephalograph (EEG and MEG) measurements. These imaging and mapping techniques are not able to measure the micro- (e.g. individual cells' synaptic connections and action potentials) or meso-scale (e.g. fine-structure and local field potential of cortical layers and columns) structure and function. Instead, they usually gain information on the macro-scale (sulci, gyri, Brodmann-areas) with a typical spatial resolution of 0.1-50 mm (MRI <M/EEG) and temporal sampling of brain function between 0.01 - 100 Hz (M/EEG <fMRI).

Functional brain network analysis consists of three major issues: (i) defining the network nodes, (ii) determining connections (edges) between nodes and (iii) graph theoretical analysis of the reconstructed network [25, 26]. Following an early definition [27] two brain regions would be functionally connected, if their neural activity was synchronized. Thus, the functional connection between regions A and B (defined by digital neuroanatomical brain atlases or data-driven functional parceling methods) can be modeled by an appropriate similarity measure between the activation time series of A and B. Modeling methods described in the literature can be distinguished in the manner they handle indirect A - C - B scheme connections (e.g. does not handle: correlation, does handle: partial correlation, inverse covariance) or whether they can model the direction of the connections ($A \rightarrow B$, $B \rightarrow A$ or $A \leftrightarrow B$) (e.g. Bayes-networks, Granger causality, Structural Equation Modeling, Dynamic Casual Modeling) [26]. From a mathematical point of view, we have to deal with undirected graphs in the former case and directed, weighted graphs in the latter case. Latest findings have demonstrated that the brain - similarly to several other complex networks - shows properties of scale-freeness and is organized into small world topology [28], thus characterized simultaneously by segregation and integration properties which allow efficient information processing and parallel computing capabilities.

Network analysis consists of three levels: global (the whole graph is described by one parameter, e.g. small-worldness, global and local efficiency, edge density, etc.), modular (nodes organized into clusters, clicks or communities) and regional (role of a given node within the whole network, e.g. nodal strength, nodal efficiency, clustering coefficient, betweenness centrality, various hub-scores) [25]. While global measures are expected to alter only in case of immoderate pathological malformations, modular organization and regional parameters can sensitively detect phenomena which were not examinable by classical methods in neuroradiology [29].

Functional magnetic resonance imaging (fMRI) is one of the most effective techniques for mapping the functional macro-connectivity of the brain. Despite the vast number of promising results, one should be careful when drawing conclusions since some artifacts in fMRI are not well understood and might appear as a systematic confound in fMRI connectivity analysis [30]. One potential source of systematic error are the motion artifacts caused by small movement of the patient's head during the scan. However, these artifacts were intensively studied in the past decade [17,31–46], the direct link between the degree of head displacement and the caused artifactual change in signal intensity is not well understood [45]. Thus, motion artifacts might be even more problematic in emerging techniques like functional connectivity analysis where the relation between artifactual signal changes and outcome variables is more complex. For instance, rotational components of head motion cause different displacement at different sampling points (voxels), and thus, might result in complex spatio-temporal motion artifact patterns. Unlike traditional hypothesis-driven methods, connectivity analysis investigates the link among different loci with possibly different artifact pattern. Therefore, the estimated connectivity strength might be biased in the subject space or between subjects.

In the followings, after a brief overview on the basic concepts of biomedical background, measurement technique and analysis strategies, our current knowledge about functional MRI motion artifacts is

Table 1. Most important milestones in the development of MRI

1944	Isidor Isaac Rabi	**Nobel prize**: phenomenon of magnetic resonance
1952	Herman Carr	PhD thesis: one-dimensional NMR spectrum
1952	Felix Bloch and Edward Mills Purcell	**Nobel prize**: NMR resonance frequency and nuclear precession
1971	Paul C. Lauterbur	PhD thesis: MR gradient imaging
1972	Raymond Damadian	U.S. patent #3,789,832: NMR tumor detection
1977	Peter Mansfield	echo planar imaging (EPI)
1977	Richard S. Likes	U.S. patent #4,307,343: k-space imaging
1990	Seiji Ogawa	BOLD effect (functional MRI)
2003	Lauterbur and Mansfield	**Nobel prize**: MRI

summarized and the goals of the present study are defined.

1.1 Magnetic Resonance Imaging

Magnetic Resonance Imaging (MRI) is an in-vivo and basically non-invasive medical imaging procedure producing cross-sectional and three-dimensional images of internal structures in the body. Although MRI is nowadays a widespread technique in radiology and medical diagnosis, the technology itself has a complex physical basis. Several results of the 1900's physical sciences have had an important role in the invention of MR imaging (See Table 1 for a brief summary of the most important milestones).

The theory of nuclear magnetic resonance describes how atomic particles react to electromagnetic energy within external magnetic fields. Due to their inner structure and dynamics, particles generate an own small magnetic field. Due to the phenomenon called Larmor precession [], the external magnetic field exerts a torque on the magnetic moment. The angular momentum vector precesses about the external field axis with an angular frequency, known as the Larmor frequency. This interaction is determined by strict energetic rules and reaches a thermal equilibrium exhibiting a certain ratio of nuclei in high- (anti-parallel) and low-energy (parallel) states. Some of the particles can be excited and forced to switch to the high-energy state, using a radio-frequency impulse matching the energy difference between the two states (aka. having a Larmor frequency). Since the thermal equilibrium is disrupted by this excitation, immediately after this irradiation, the excess spins at the higher energy level return to the lower level. During this reception or relaxation period, the spins emit electromagnetic energy that can be detected by a radio-frequency coil. Several properties of the detected decaying signal depends on the molecular environment of the spins. Applying a gradient (spatially varying) magnetic field causes spins at different locations to precess at different frequencies in a controlled fashion. By measuring changes in magnetization as a function of precession frequency, the total MR signal can be parsed into components associated with different frequencies. The acquired MR signal is collected with a notation scheme called k-space. The inverse-Fourier transformation of the k-space data yields the image in the spatial domain.

Compared to other methods in neuroimaging, MRI is extraordinarily versatile. A wide variety of anatomical and physiological tissue characteristics can be distinguished by applying certain image contrasts. Contrasts can be divided into three types: static contrasts, motion contrasts and exogenous contrasts [47].

Static contrasts are sensitive to the type, number and relaxation properties of atomic nuclei within a voxel. These contrast can provide information about density (proton density), relaxation time (e.g. T_1, T_2,T_2^*), content of a particular molecular type (e.g. small or large molecules detected by magnetization transfer) and general chemical content (spectroscopy).

Motion contrasts are sensitive to the movement of atomic nuclei and the dynamic characteristics of proton pools in the brain. By these contrasts, blood flow (perfusion imaging and angiography) and water diffusion (Diffusion Weighted Imaging, DTI) can be measured.

Exogenous contrasts are not based on the intrinsic properties of the biological tissue, instead it depends on the presence of foreign substances that have been introduced into the body. An example for this Dynamic Contrast-Enhanced MR imaging, where a fast bolus of T_2^*-decreasing contrast agent (e.g. gadolinium) is administered into the body and the cerebral perfusion is characterized by the dynamics of the perfusion of the contrast-agent containing blood.

1.2 Functional Magnetic Resonance Imaging

Various contrasts make it possible to indirectly monitor the neural activity, mostly by measuring some parameter being in relation with the amount, dynamics or oxygenation of cerebral blood and taking advantage of the phenomenon of neurovascular coupling. In the focus of this thesis is the so-called Blood Oxygen-Level Dependent (BOLD) signal. In the followings, after a short introduction to the underlying neurobiological mechanisms (function hyperemia and neurovascular coupling), the physical background and the biological correlates of the BOLD MR signal will be reviewed.

Neurobiological background

The information processing in the human brain is implemented by the complex interplay among the vast number of neurons (approximately 20 billion just in the neocortex [48]). One neuron is interconnected with hundreds of other neurons, forming a complex network with more than 10^{12} connections. Neurons have a complex structure, with an intricate tree of fine dendrites extending outward from the cell body and a single axon that carries outgoing signals. The axon divides into many branches and a branch makes contact with a dendrite or cell body of another neuron at a synapse. Most of these connections through synapses are formed between nearby neurons, but some connections are much longer, providing this network with the ability of segregated parallel information processing with a globally integrated flow of information (the so-called small-world property, introduced in [4] and [5] and described in the brain by [12]).

A key aspect of neurons (and in general, all types of cells) is the membrane potential. This property is the medium of the neuronal signaling: it is the physiological property altered in one neuron when it receives a signal from another one. An action potential (or spike, as referred to by its electrophysiological appearance) is a transient disturbance of that potential, a rapid depolarization of the membrane near the origin of the axon. This action potential propagates down the axon until it reaches a junction with another neuron at a synapse.

At the synapse, the action potential triggers the release of neurotransmitter molecules into the synaptic cleft separating the pre- and post-synaptic membranes. The neurotransmitters diffuse across this thin gap (20-40 nm) and bind to receptor sites at the post-synaptic membrane. Binding the neurotransmitter makes the receptor change or modulate the post synaptic neuron and trigger an excitatory or inhibitory post-synaptic potential. Each neuron has the capacity to integrate the inputs from many other neurons through their cumulative effect on the post-synaptic potential. A new action potential is generated by the post-synaptic neuron if the region where the axon originates becomes sufficiently depolarized. As a result, the membrane potential of the neuron quickly recovers to the default level and the newly triggered action potential spreads towards other neurons.

Although, the above description is obviously an oversimplified model of information propagation during neural information processing (for a more detailed description, see e.g. Part IA in [49]), systems with similar simplicity, known as artificial neural networks, successfully demonstrate the computational ability of such a construct [50]. These computational models share the principles of non-linear, distributed, parallel and local adaptive processing and besides their use in theoretical computer sciences, statistics, artificial intelligence and expert systems, nowadays they also have an important role in cognitive psychiology, theoretical neuroscience and computational neuroscience.

From a thermodynamic point of view, each step of neural signaling is a downhill reaction in which a system held far from equilibrium (and thus, having free energy) is allowed to approach closer to equilibrium. Thus, with each action potential and release of neurotransmitter at a synapse, the available free energy is reduced. Returning the neurons to their prior state, with the original ion gradients and neurotransmitter distributions, requires and essential process: the energy metabolism.

Theoretical estimates of energy metabolism and energy budget of different aspects of neuronal signaling can be considered as a superposition of these processes: (i) maintenance of the cell at rest, (ii) the generation and axonal propagation of an action potential, (iii) recovery on the pre-synaptic side of the synapse and (iv) recovery from post-synaptic potentials. While the first process can be considered as basic housekeeping of the cell, the other three components are directly related to signaling, broken down as the spiking activity and pre- and post-synaptic activity. According to Attwell et al. [51], for the primate brain, the dominant energy cost is recovering from post-synaptic potentials (74%). Thus the overall energy cost of neuronal signaling will depend on the actual spiking rate and the number of synapses reached by each action potential.

This time varying and regionally specific energy metabolism requires glucose and oxygen which are delivered by the cerebral blood flow (CBF). Complex and flexible biological autoregulation processes ensure that the required amount of glucose and oxygen is available and yet, the system stays cost-effective. For instance, through the so-called neurovascular coupling the vascular system regulates the velocity, volume and flow of cerebral blood, causing a transient functional hyperemia in regions of increased neuronal activity and by this, supplying the required amount of glucose and oxygen during increased activity. The exact mechanism behind neurovascular coupling is not completely understood; several parallel re- and pro-active pathways and feedback and feedforward mechanisms have been suggested to regulate the vascular resistance, depending on the neuronal demands [49, 52].

Nevertheless, neuronal activity is followed by a hemodynamic response: changes in vascular resistance, changes in volume, flow, velocity and other parameters of the cerebral blood (such as O_2 and CO_2 concentration) and thus, can be considered to reflect the underlying neural activity. The neurovascular response is an acute, but not prompt reaction. Thus, when measuring hemodynamic parameters in regions of the brain, one should consider that the underlying changes of neural activity become convolved with the so-called hemodynamic response function, and in general, are only an indirect indicator of it (Figure 1).

Blood-oxygen level dependent signal

Magnetic resonance imaging provides several image contrasts which can be used for functional imaging of neuronal activity. These imaging techniques mostly take advantage of the neurovascular coupling and measure local transient changes in the dynamics and/or biophysical properties of cerebral blood. This work focuses on functional MR imaging based on the so-called blood-oxygen level dependent signal (BOLD) contrast.

The physical basis of BOLD sensitivity of the MR signal is that deoxyhemoglobin alters the magnetic susceptibility of blood. The magnetic properties of hemoglobin, and their dependence on the oxygenation state of the heme groups has been known since 1936 [53]. Deoxyhemoglobine is paramagnetic and when O_2 binds to the heme group the paramagnetic effect is reduced. As a result, the magnetic susceptibility of blood varies linearly with the blood oxygenation [54]: the T_2^* shortens and the measured signal decreases with an estimated maximum of approximately 8% at 1.5T. However through the neurovascular coupling, neuronal activation leads to increase in blood flow and blood volume. This increase is much larger than in oxygen metabolism, so the net oxygen extraction fraction drops with activation. With less deoxyhemoglobin, the magnetic susceptibility of blood moves closer to the susceptibility of the surrounding tissue, the T_2^* becomes longer and the signal measured with a T_2^*-weighted pulse sequence contrast increases by a small percentage. The effect of increased oxygen metabolism can only be seen before the functional hyperemia, as an initial dip in the signal (tipcally on high magnetic field, see Figure 1).

Due to this complex relationship, the BOLD effect depends on multiple physiological changes: alterations in cerebral blood flow (CBF), cerebral metabolic rate of oxygen ($CMRO_2$) and venous cerebral blood volume (CBV) all affect the local deoxyhemoglobin content. During neural activation, CBF increases dramatically, venous CBV increases moderately and delayed, and the cerebral metabolic rate of oxygen increases to a much smaller extent. These physiological parameters have conflicting effects on BOLD signal during activation. The increase in CBF produces a positive BOLD response, but the increase in $CMRO_2$ partially counteracts it. Increased venous CBV also tends to decrease the signal. As a summation of these effects, the BOLD signal increases during neuronal activation. The increase is approximately 3-5%, compared to the baseline (Figure 1).

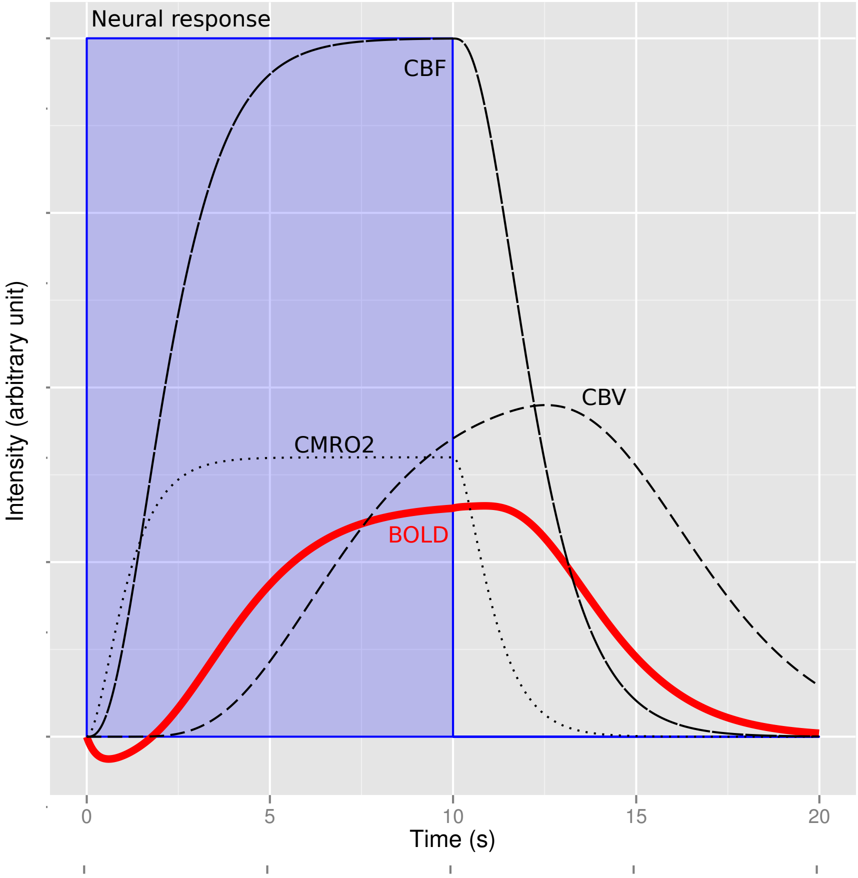

Figure 1. Schematic representation of changes in blood flow in response to neuronal activation
Local neuronal activity (during the time interval denoted by the blue area) triggers metabolic activity, which in turn triggers a large increase in cerebral blood flow (CBF), a moderate increase in cerebral blood volume (CBV) and a small increase in the cerebral metabolic rate of oxygen (CMRO2). The response curves of each quantity suggest ways in which the stimulus shape is altered in the progression of the BOLD response. The overshoot in CBF and CBV response, compared to CMRO2, triggers a decreased oxygen extraction fraction during activation and thus decreases the oxyhemoglobin/deoxyhemoglobin ratio. Therefore, the combined changes in CBF, CBV and CMRO2 create the BOLD signal change.

1.3 Preprocessing of Image Data

Medical image

According to the standard definition [55] (also used in [56]), an m-level digital image is the function

$$f : X \to Y \quad (Y = \{0, 1, ..., m-1\}, m \in \mathbb{N}, m \geq 2) \tag{1}$$

where coordinate-set X is an n-dimensional digital set ($X \subseteq \mathbb{Z}^n, X \neq \emptyset$) and Y is the valueset of the image.

The ordered pair $(\mathbf{x}, f(\mathbf{x}))$, where $\mathbf{x} \in X$, is called a pixel ($n = 2$) or voxel ($n \geq 3$), where $\mathbf{x} = (x_1, \dots x_n)$ is the coordinate of the pixel (voxel) and $f(\mathbf{x})$ is the value (or brightness, intensity) of $\mathbf{x}$ ($x_i \in \mathbb{Z}, i = 1 \dots n$). In medical image analysis, this general definition usually simplifies to the cases $n \in \{2, 3, 4, 5\}$ and extends with some additional properties, which assign real-world values to voxel locations and values, as follows:

- The function g, which defines the assignment between voxel value and measured information (which can be relative or quantitative, viz. may or may not have unit assigned to it):

$$g : Y \to Q \quad (Q \subseteq \mathbb{R}, Q \neq \emptyset) \tag{2}$$

- The matrix M defining the image orientation (in accordance to a reference coordinate system) with an affine coordinate transformation t:

$$t : X \to W \quad (W \subseteq \mathbb{R}^n, W \neq \emptyset) \tag{3}$$

  and t is of the form:

$$\mathbf{x} \to M\mathbf{x} + \mathbf{b} \quad (\mathbf{x} \in X, \mathbf{b} \in W) \tag{4}$$

In practice, the function g is defined by the image contrast and acquisition sequence, and is of high importance in analysis of quantitative medical images. X and W finite-dimensional vector spaces have the same dimension n and M is an $n \times n$ affine transformation matrix. The real-world unit assigned to the coordinate system of W is usually mm.

The most common value of the dimension of the image is $n = 3$, representing the three-dimensional space, although depending on the imaging contrast, higher dimensional images are also possible. In functional MRI, a three-dimensional image is acquired, where the fourth dimension is the acquisition time.

In contrast with the above described formulation, four dimensional fMRI data is often considered as a series of three dimensional images. Therefore, in many application, an fMRI volume series is denoted as:

$$Y = \{\mathbf{y_i}\}_{i=1}^{M} \tag{5}$$

where $\mathbf{y_i}$ is the observed voxel time series and the index i identifies the voxel and M is the number of voxels considered in analysis. Each voxel time series $\mathbf{y_i}$ consists of T fMRI observations [57]. To make the link with definition (1), the $\mathbf{y_i}$ time series can be written as:

$$\mathbf{y_i} = (f(x_1, \ldots, x_n(t_1)), \ldots, f(x_1, \ldots, x_n(t_T))) \tag{6}$$

where f is the n-dimensional digital image, i is the index corresponding to the 3D voxel with coordinates $(x_1, \ldots, x_{n-1})$ and the n^{th} dimension is time.

Image segmentation

In computer vision, image segmentation is the process of partitioning a digital image into multiple segments (sets of pixels or voxels) by assigning labels to every element (pixel or voxel) such that elements with the same label share certain characteristics.

In the context of medical image analysis, segmentation often aims to identify anatomical or functional parts on the image. For instance, common segmentation tasks in neuroimaging are brain extraction and tissue-segmentation.

Many segmentation problems in neuroimaging are complex and therefore, require elaborated statistical optimization techniques, like finite mixture models, hidden Markov random field models and moreover, often incorporate a-priory information (See some examples in [58, 59]).

Spatial co-registration

BOLD fMRI images are designed to be sensitive to function, thus usually have a relatively rough spatial resolution (typically 3-4 mm in human and 0.5-1 mm in small animal imaging) and a poor anatomical contrast. On the other hand, functional information needs to be mapped to the subject's anatomy, or, in population-level studies, to the other subjects' anatomy. However, this mapping is not trivial. On the population-level, due to the morphological diversity of the subject's brains and the different patient positioning during scanning, the point-to-point spatial correspondence is not present. Even on the individual level, functional and anatomical scans, even after resolving differences in the M transformation (due to image sampling), spatial correspondence might be disturbed by image distortions and subject motion.

Therefore, in several steps of the image processing pipeline, images need to be spatially matched, and the corresponding geometric transformation needs to be obtained. In the terminology of medical imaging, this procedure is called spatial image co-registration and can be defined as finding the transformation that minimizes the difference between the images. The choice of the difference measure (or distance measure) depends on the image contrasts (unimodal, multimodal) and the type of registration problem (intra-subject, inter-subject). The conventional medical image co-registration software tools usually implement label difference, least squares difference, spatial correlation ratio and (normalized) mutual information. Some advanced co-registration approaches utilize secondary image features, like edge- and boundary-detection.

Co-registration problems also differ in the type of transformation to estimate. Typically, during intra-subject registration, a rigid-body transformation needs to be obtained (rotation and translation). In some cases, image distortions need to be corrected using scaling and shears, thus we obtain an affine-transformation. This is the case, when aligning fMRI images to high-resolution anatomical (T_1, T_2) images of the same subject.

Spatial standardization

In population-level studies, individual high-resolution images are usually transformed into a common standard space defined by a conventional standard space image template, representing the "average" brain for that population. The high degree of individuals' morphological diversity makes global image transformation insufficient. In this case localized, elastic transformations are estimated; deformation fields, which assign a different 3D displacement vector for each voxel. These approaches are referred to as nonlinear co-registration approaches [60].

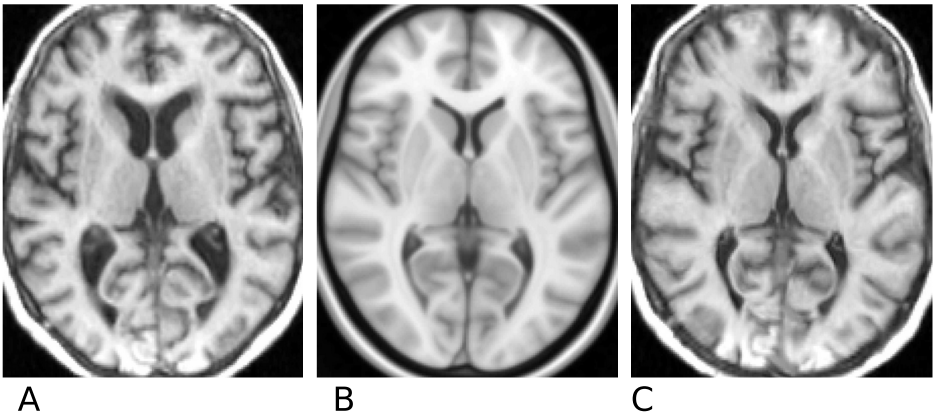

Figure 2. Nonlinear spatial standardization of high-resolution anatomical MR images T_1-weighted anatomical MR image of a demonstrative subject co-registered linearly (affine-transformation) (A) and non-linearly (C) to the MNI-152 standard brain template image (B).

Image realignment-based motion correction

A special type of spatial image co-registration tasks during fMRI preprocessing is motion correction. An fMRI scan typically lasts for 30-60 minutes and a 3D image is obtained every few seconds (depending on TR). Besides vast abrupt subject motion, relatively small head movements caused by respiration and circulation can also cause artifacts during acquisition and spatial mismatch in time. Thus dealing with in-scanner head motion is an essential step of every fMRI preprocessing workflow. Spatial mismatch can be resolved by co-registration of time-frames (3D images) to a reference image (e.g. the middle image in time or a separate position-identical T_2-weighted image) [35]. This image realignment-based methods are considered to be able to properly correct spatial mismatch caused by motion, but do not correct for intensity confounds caused by head displacement in the gradient field. In this study, realignment-based motion correction is utilized to account for spatial mismatch and to estimate the temporal and spatial pattern of subject motion. Intensity-based retrospective motion-correction techniques are discussed in detail in section 1.6.

1.4 Resting-state Brain Activity and BOLD signal

The small but specific BOLD signal change during neuronal activation can be utilized to capture and map brain activity corresponding to specific stimuli or tasks. Due to the relatively low signal-to-noise ratio, these mapping methods require repetition of the investigated condition and extensive signal preprocessing and statistical analysis to determine how unlikely is that signal increases co-occurring with stimuli have been occurred only by chance. Areas, where significant activities were measured can be considered as the loci or the center areas for the given tasks. These localization-oriented task-based approaches have produced many promising neuroscience results and have proven to be useful in basic research and in studying neuropathological conditions, as well (for a review, see [61] and [62]).

In contrast with task-based methods, a new area of application of BOLD-fMRI investigates the spontaneous BOLD fluctuation of the ”resting” brain, in absence of any explicit task. While task-based approaches aim to eliminate any signal component which is not directly related to the task, resting-state approaches aim to characterize the general neural functioning. No explicit tasks are performed and moreover, the neural correlates of known stimuli during scanning are often subject of elimination. Instead of localizing the neural activity associated with some conditions or stimuli, resting-state fMRI (rs-fMRI) studies aim to estimate the functional connectivity between distinct brain areas, based on the synchronization of their spontaneous fluctuation in the BOLD signal, induced by spontaneously fluctuating neuronal firing-rate.

Biswal and colleagues [63] were the first to demonstrate that during rest the left and right hemispheric regions of the primary motor network are not silent, but show a high correlation between their BOLD time series; suggesting ongoing information processing and ongoing functional connectivity between these regions, even in the absence of patients' significant motor activity. Several studies have replicated and extended this findings by showing a high level of resting-state functional co-activation between regions of other functional subnetworks, like visual cortex, auditory network and higher order cognitive networks. These studies marked that during rest the brain is not idle, but rather shows a vast amount of spontaneous activity that is highly correlated between multiple brain regions.

Due to the nature of BOLD signal, of special interest are the low frequency oscillations (0.01 - 0.1 Hz) of rs-fMRI time series. The true neuronal basis of these low frequency rs-fMRI oscillations is not yet fully understood. In the past years there has been an ongoing debate on whether these resting-state BOLD signals result from physiological processes, like respiratory and cardiac oscillations or these correlations originate from co-activation in the underlying spontaneous neuronal activation patterns, measured through the hemodynamic response function. Typically, fMRI protocols have a low temporal resolution (2-3 s per scan, called repetition time or TR), causing high frequency oscillations to be aliased back into the lower frequencies. Another spurious source of rs-fMRI oscillations might be motion artifacts. However, support for a possible neuronal basis of resting-state fMRI signals comes from the observation that most of the resting-state connectivity patterns tend to overlap with functional neuroanatomy [64]. Several studies report on an association between the amplitude profiles of rs-fMRI correlations and electrophysiological recordings of neuronal firing [65]. Furthermore, cardiac and respiratory oscillations have been reported to have a different frequency pattern than the frequency of interest in rs-fMRI studies. Taken together, more and more studies are in support of a neuronal basis of rs-fMRI signal. However the contribution of physiological sources and motion artifacts cannot be ruled out [46].

In general, the function and purpose of resting state brain activity is currently poorly understood and is subject for intensive research.

Also, a practical but very important consideration makes the investigation of resting-state brain activity very engaging: measurements can be performed in non-collaborative subjects (particular pathological conditions, sleeping or anesthesia and animal experiments). BOLD fMRI-based brain connectivity analysis provides a promising tool in this research perspectives.

1.5 Functional MRI-based Brain Connectivity Analysis

In contrast with task-based analysis methods where changes in the BOLD signal are subject to be explained with an a-priori hypothesis about the task, a new area of application of BOLD-fMRI is to investigate the relationship or connectivity between spatially distinct regions. This concept has multiple advantages over task-based analysis. On one hand as described in the previous section, it provides the opportunity to investigate resting-state brain activity. On the other hand, while task-based methods follow the "localizationist" point of view and in general, aim to assign brain areas to various functions, investigating functional connectivity might provide an integrative insight into brain function by applying the recent advances of network scinece.

In a mathematical point of view, brain networks can be represented as graphs: an ordered pair $G = (V, E)$, where V is the set of vertices or nodes, which macro-scale functional units in the brain, and E is a set of edges representing a sort of measure of functional connectivity between two nodes.

Thus, functional brain network analysis consists of three major issues: defining the nodes of the network, determining connections (edges) among nodes and graph theoretical analysis of the reconstructed network [25, 26] (Figure 3).

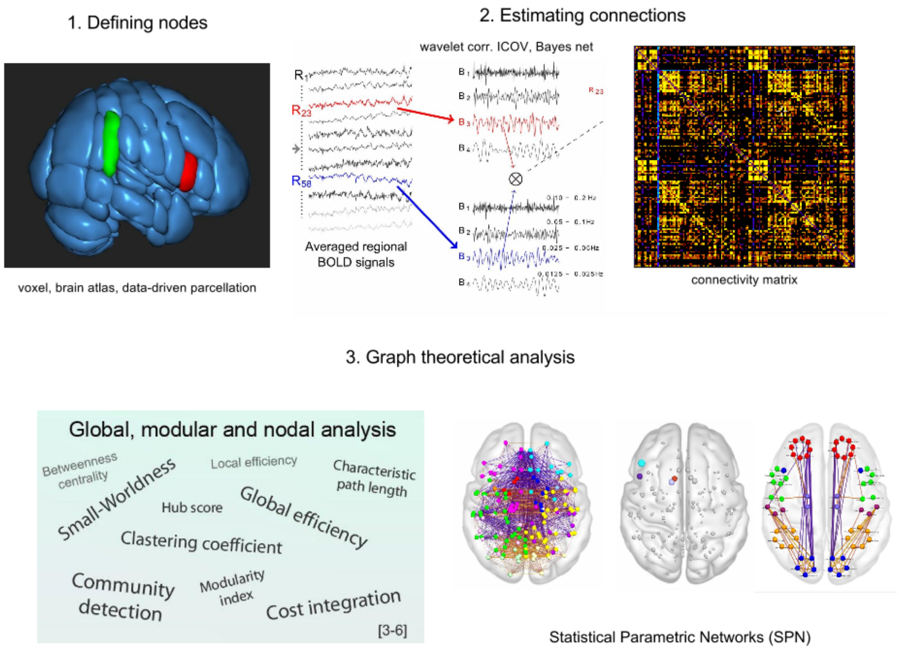

Figure 3. Graphical overview of the basic steps in a typical functional MRI-based brain connectivity analysis pipeline
Functional brain network analysis consists of three major steps: defining the nodes of the network, determining connections (edges) among nodes and graph theoretical analysis of the reconstructed network

Definition of Nodes

Following the notation in section 1.3, fMRI data can be considered as multiple time series $\mathbf{y_i}$. As a first approximation, each sampling point i could be considered as a node in the network. However in practice, voxel-wise network analysis is rarely applied in fMRI brain connectivity analysis. There are several deliberations behind this:

- signal-to noise ratio is poor in individual voxels,

- voxel time series are not independent: anatomically or functionally neighboring voxels often show coherent activity, which suggests that some data-reduction should be considered,
- voxel-wise analysis would mean a graph consisting of approximately 10^8 edges. Such big data is computationally hard to handle, particularly when the several NP-hard problems in graph theory are considered [66].

Therefore, voxels are usually ordered to form larger disjunct regions-of-interest (ROI) [26]. These ROIs can be formed with the aid of a-priory information on functional neuroanatomy, encompassed in digital brain atlases [67], or using data-driven parcellation methods which identify functionally coherent voxel sets [68]. After the formulation of region system, the constructed ROIs represent the nodes of the network to form. Based on the voxels in the given region R, a regional time series can be constructed (henceforward denoted as $\mathbf{y_R}$). The most common way to do it is simply taking the average $\mathbf{y_R} = \sum_{i \in R} \mathbf{y_i}/|R|$, where $R \subset X$ is the brain region defined as a set of sampling points. Other, more elaborated calculations are also possible (for instance taking the first principal component of $\mathbf{y_i}$, $(i \in R)$.

Estimation of connectivity strength

Following an early definition [27] two brain regions would be functionally connected, if their neural activity was synchronized. Thus, functional connection between regions A and B (defined by digital neuroanatomical brain atlases or data-driven functional parceling methods) can be modeled by an appropriate similarity measure between the activation time series $\mathbf{y_A}$ and $\mathbf{y_B}$. Modeling methods described in the literature can be distinguished by the manner they handle indirect $A - C - B$ scheme connections (e.g. does not handle: correlation, does handle: partial correlation, inverse covariance, Patel's τ) or whether they can model direction of the connections (

$A \to B$, $B \to A$ or $A \leftrightarrow B$) (e.g. Bayes-networks, Granger causality) [26]. From a mathematical point of view, we must deal with undirected graphs in former case and directed, weighted graphs in latter case. For its simplicity, the most common similarity measure in the corresponding literature is Pearson correlation. Also, some evidences [69] point to the conclusion that correlation outperforms methods based on higher order statistics, phase or temporal lag. A possible reason for that is that the BOLD signal is relatively close to being Gaussian, i.e., most of the useful signal lies in the variance. This is primarily because the hemodynamic blurring (see section 1.2) removes much of the structured signal of interest from the original neural processes. However, correlation assumes linearity and stationarity in the data, while resting state activity is clearly nonlinear and non-stationary. Therefore, more complex measures of connectivity are subject of intensive research.

Graph-theoretical analysis

Latest findings have demonstrated that the brain - similarly to several other complex networks - shows properties of scale-freeness and is organized into small world topology [28], thus characterized simultaneously by segregation and integration properties which allows efficient information processing and parallel computing capabilities. Such networks can be analyzed by means of complex network theory [4–6]. Network analysis consists of three level [25]:

- global analysis: the whole graph is described by one parameter, e.g. small-worldness, global and local efficiency, edge density, etc.,
- modular analysis: nodes organized into clusters, clicks or communities, and
- regional or ”nodal” analysis: role of a given node within the whole network, e.g. nodal strength, nodal efficiency, clustering coefficient, betweenness centrality, various hub-scores.

While global measures are expected to alter only in case of radical pathological malformations, modular organization and regional parameters can describe the fine-structure of the underlying network and might be able to sensitively detect phenomena which were not examinable by classical methods in neuroimaging [29]. More information on graph theoretical brain network analysis can be found in reviews [5–7, 12, 25] and in section 3.8.

1.6 Motion Artifacts in fMRI Connectivity Analysis

MR images carry various types of artifacts. Usually geometric distortions and variations in signal intensities can be experienced. These two types of artifacts can be considered as macroscopic and microscopic effects and are caused by inhomogeneities in the magnetic field. Large-scale inhomogeneities will lead to changes in spin frequency. Since the position of a voxel is encoded in its spin frequency, these inhomogeneities will cause spatial shifting of voxels. Small scale inhomogeneities cause spins within a voxel to lose coherence due to T_2^* effects. This reduces the total magnetization available within a voxel and thus reduces signal intensity.

Similar changes can be caused by the motion of the subjects' head during scanning. Large movements cause mispostioning of subsequent MR images and differential effect of magnetic field inhomogeneities in various spatial locations. Small movements can cause intensity drops by introducing discrepancy between the excited volume and the subsequent readout of the MR signal. While artifacts originating from the static inhomogeneities of the magnetic field are more constant and thus can be handled easier, subject motion introduces a temporally and spatially varying source of MR artifacts. Thus, motion artifacts are problematic for all types of MRI including resting-state functional MRI.

Therefore motion correction is a vital step in every work-flow during fMRI analysis. According to population-level analysis and group comparisons, retrospective motion related artifact removal strategies can be performed at five different stages of the data processing pipeline: (i) motion correction of fMRI time series by realignment to a reference image (using automatic co-registration approaches) [32]; (ii) censoring data to exclude periods of high motion (scrubbing, de-spiking) [40, 41]; (iii) modeling the effect of motion-related nuisance parameters on blood oxygen level dependent (BOLD) signal [33,36,70,71]; (iv) temporal filtering of BOLD timecourses to discard frequencies encumbered by motion artifacts and (v) correct for subject-specific motion effects on population-level (descriptive summary statistics of subject-specific motion as second-level model regressors) [16, 39, 42].

Traditional realignment-based correction approaches ensure that different time-points of the BOLD signal correspond to the same location. However, such methods do not handle voxel-level intensity confounds originating from the establishment of magnetic gradients and subsequent readout of the BOLD signal [31,41]. Furthermore, automatic co-registration approaches may introduce spurious displacements in intervals of relatively low motion [34]. Nonetheless, subject movement is often measured with parameters based upon the resulting image realignment transformations.

Large BOLD intensity confounds (spikes) in time-frames with extreme, abrupt movement can be eliminated from the analysis by simply dropping the corrupted data (”scrubbing”) [41] or by spike-regression [37]. However, the reduction in time points is associated with an increase in the likelihood of high correlation scores [42]; moreover, recent findings [42, 45, 72] suggest that in population-level functional connectivity studies, scrubbing can be omitted from the analysis when using proper second-level correction.

Intensity confounds originating from micro-movements (as small as 0.1 mm from one time point to the next) can also disrupt results, especially in case of correlation based connectivity analysis methods, where such small but temporally concordant noise leads to spurious increase in connectivity strength [39, 41, 43]. Nuisance signal regression approaches aim to eliminate the signal components of non-neuronal origin from the raw BOLD data utilizing linear regression. These confounder signals can be defined by dedicated physiological monitoring devices during the scan, calculated from motion parameters extracted during spatial realignment based motion correction or derived directly from the data itself, using a ”noise ROI” [33, 36, 38].

Temporal filtering is also a crucial step in the reduction of fMRI brain connectivity artifacts, including motion confounds. Most connectivity studies apply a band-pass filter with a high-pass cutoff of 0.008-0.01 Hz and a low-pass threshold of 0.08-0.1 Hz [73]. While there is evidence that resting-state networks are present at a relatively broad band in the frequency spectra [74], slight modifications in the frequency band have been suggested [40].

Some of these techniques can effectively reduce not only motion-related effects, but also physiological noise (e.g. cardiac or respiratory confounds) or hardware drifts and instabilities. However, recent studies [40, 42, 75] report that clear artifacts remain in the data even after such regression and filtering approaches, and that these artifacts have systematic effects upon resting-state functional MRI connectivity (rs-fcMRI) patterns.

When performing group comparisons in functional connectivity studies, one can account for these motion-related residual artifacts during the second-level analysis by inclusion of motion-related, subject-specific covariates into the population-level model. A common choice is to include a measure of the average patient movement [16, 39, 42]. Alternatively, the value of global voxel-to-voxel correlation (GCOR) can be utilized as confounder, as in [75], although the latter quantity can also carry valuable neurological information.

Due to in-scanner head rotation, the effect of patient movements on the BOLD signal is not spatially constant in the whole brain; however, this local relationship is poorly understood and is rarely considered in brain connectivity studies. The pattern of voxel-wise motion not only varies among different loci of the same subject, but also among subjects. According to Satterthwaite et al. [39], between-subject differences of motion are stable and hence, in-scanner head motion should be considered as a trait. Thus, the effect of the subject-specific spatio-temporal motion pattern on the BOLD signal could bias group analysis when different groups have different tendencies in their spatio-temporal motion patterns. This is particularly problematic in studies when regional connectivity deficits are associated with a pathological condition, and thus, limits the usability of functional connectivity as a biomarker of disease. These biases in the functional connectivity pattern can lead to invalid conclusions regarding biomedical hypotheses, as denoted by [30] and demonstrated by [75], especially in pathholological conditions associated with hyperkinetic patients (epilepsy, attention deficit hyperactiviy disorder, some forms of autism). Group-wise inconsistencies in motion patterns can arise from different patient positioning and multi-center studies are also challenging in this regard.

2 Purposes

As a basis of the present work, here we hypothesize that certain artifactual effects in resting-state fMRI connectivity analysis may originate from the complex voxel-wise spatio-temporal nature of head displacements, and can be modeled more efficiently when incorporating this information, compared to handling motion artifacts as spatially homogeneous confounds.

The possibility of utilizing the voxel-wise nature of in-scanner motion in artifact removal approaches has not been intensively investigated, as yet. As recently reported by two studies [40, 45] and confirmed by our preliminary analysis, including voxel-wise displacement parameters as voxel- or region-wise covariates in the appropriate nuisance signal regression model (”regressing out” motion from the signal) does not significantly improve motion artifact removal, compared to the usual technique, the regression of spatially averaged global displacement parameters. However, Yan et al. in [45] also bring up the possibility that an appropriate correction technique may have greater success in using the rich information encapsulated by voxel-specific indices.

This study was designed to **characterize the impact of voxel-wise head motion artifacts in population-level rs-fcMRI brain connectivity studies** and **investigate how this local information on displacement can be utilized for artifact removal**. These purposes are to achieve by investigating the followings:

- Based on the latest results and suggestions in the corresponding literature, we aim to **establish a complex image processing pipeline** and the required software infrastructure. When available, open source software libraries are utilized. Several components of the processing pipeline, like **parallel implementation** of computationally intensive processes, **graph theoretical analysis**, special graph **visualization** tools and problem-specific **segmentation** approaches are developed based on our in-house developed MultiModal Medical Imaging (M3I) software library system. The developed software infrastructure is designed to be a **high-throughput** system to allow analysis of image databases consisting of more than one hundred subjects.

- Using the developed software tools, we demonstrate the **local correspondence between head displacement and the changes in the resting state functional MR signal**. We then aim to investigate how functional connectivity strength is affected by the deviations in the average regional spatial displacements on the population-level.
- We **propose** Regional Displacement Interaction (RDI), a **novel modeling approach** for second-level brain connectivity analysis, which provides the opportunity to incorporate voxel-wise motion information into the population-level model and to account for corresponding artifactual effects.
- **The effectiveness of this motion artifact reduction technique** is evaluated by investigating the variance explained by the proposed confound covariates in the model. The method is than demonstrated in group comparisons of cohorts with differing average voxel-wise displacement patterns.
- Due to the disagreement [40, 45, 75, 76] about the optimal first-level nuisance signal regression technique, we perform a **comparison of prevailing first-level nuisance signal regression approaches** and characterize their interference with the proposed method.
- Finally, to **test** whether the proposed method preserves group differences of neuronal origin, a comparison of autistic and control groups is performed. Results might give valuable extra information regarding potential false positive results in brain connectivity studies of autism (raised by Deen and Pelphrey in [30]).

3 Establishment of Methodological Background

3.1 Institutional Development Background

In the Department of Nuclear Medicine at the University of Debrecen, in the past two decades intensive research and development has been proceeded in the field of multimodal image analysis. As a result, the MultiModal Medical Imaging (M3I) C++ software library system[1] has been developed which provides software infrastructure for various medical imaging tasks from image processing and segmentation to state-of-the-art 2D and 3D visualization. We routinely use the high performance computing (HPC) capabilities available at the University of Debrecen.

Our workgroup has a several-year experience also in the field of brain connectivity analysis. As a result of our methodological developments we deployed the software tools BrainLOC [77], BrainMOD [78], BrainNetTools and BrainCON[2] [79]. Due to the definite multidisciplinar nature of the topic, our corresponding research projects are realized as a strong collaboration between medical experts and physicists, mathematicians and computer scientists, both from Hungary and from abroad. Several software development task was performed in collaboration with one of our most important collaborating partners: the Kempenhaghe Expertise Center for Epileptology, Sleep Medicine and Neurocognition, Heeze, The Netherlands (www.kempenhaghe.nl, Dr. Pauly Ossenblok).

These software tools and components are not directly related to the findings introduced in this thesis however, serve as a basis the applied methodology of the presented work, as well as other research projects.

---

[1] http://www.minipetct.hu/m3i

[2] http://www.minipetct.hu/software

3.2 MultiModal Medical Imaging (M3I) Software Library System

Reusability is a very important principle in software design, especially for academic development teams where the human and financial assets belonging to a single R&D project are usually limited. Object-oriented programming languages, well-documented and properly designed software components, distributed revision control systems and agile development methods provide the possibility of writing reusable software with maximal cost-efficiency.

In the Department of Nuclear Medicine software development has multiple purposes: (i) it should provide an simple framework for building special applications in service of *clinical research and routine data processing* tasks and (ii) it should serve as a basis for rapid developments of *state-of-art methods* according to the latest findings in the intensively growing neuroimaging literature.

The basic platform for this agile software development in our institute is the MultiModal Medical Imaging [3] (M3I) software library system. It is being developed since 2000 and is being written in ANSI/ISO C++, extended with in-house coding convention rules. The whole system currently consists of almost half a million line of codes (487109 lines on 2015.05.05.) and approximately 8000 class definitions. The system is designed by applying various sophisticated design patterns but for a brief introduction its architecture can be simplified in terms of the Model-View-Controller (MVC) architectural pattern. Below the main libraries of the system are introduced:

- plat - platform independent library: a collection of global symbols, classes, macros and directives which hides low-level platform dependent code snippets and allows easy platform independent coding for its users in higher level libraries. Currently plat handles differences between 32 and 64 bit architectures and furthermore, Windows Xp, 7, 8 systems and various Linux

---

[3] www.minipetct.com/m3i

distributions. This library also implements software licensing, version control and error handling.

- mdtl - multi-dimensional template library: a library containing special data structures for medical images implemented in C++ template classes with vector-like operator functions to allow uniform representation with flexible base data type. It implements the main part of the model layer.

- vpp - C++ based volumetric library: implements all functionality related to handling data structures of mdtl by deriving classes and implementing abstract functions. The implemented functionality ranges from conversion and advanced indexing tools to segmentation, transformation, surface reconstruction and volume rendering algorithms and related data structures. Vpp also implements several abstract classes which serve as interfaces for OpenGL-based visualization and graphical user interface components.

- vvl.nfusion - volumetric visualization library: implements real-time 2D and 3D visualization features based on OpenGL [4] (v3.3). rendering of high-resolution 3D volumetric data is accelerated by using special hardware extensions, like 3D textures and shader programs for rendering basic graphical objects and 3D meshes. OpenGL rendering is nested into the graphical base components of the Qt cross-platform application and user interface (UI) development framework [5]. The library also contains some abstract low-level UI components and so called "slot" classes which implement the controller level between the GUI (view-layer) and data handling and representation (model-layer).

- m3t - M3I tools: Contains interfaces linking vpp-level algorith-

---

[4] www.opengl.org

[5] www.qt.io

mic components and data-structures to non-graphical command-line utilities.

- BrainCAD: computer aided brain diagnosis application library: its main class, bcApplication composes the application framework which allows the easy, prompt and cost-effective development and deployment of user-friendly GUI applications, utilizing the software components of libraries in deeper layers. This library also implements re-usable Qt-based GUI components.

3.3 Third Party Libraries

Open-source medical image analysis software libraries, like FSL (FMRIB Software Library System[6] [80, 81]), SPM (Statistical Parametric Mapping[7] [70]) and MINC toolbox (Medical Imaging NetCDF[8] [82]) are routinely used in our research projects and are also utilized in the present work. Some of our utilities developed for brain connectivity analysis uses several packages of the R programming environment, like FdrTool, ggplot2, parallel.

3.4 Software Developments for Brain Connectivity Analysis

For brain connectivity analysis, multimodal medical imaging data can be processed with a specialized software pipeline, which consists of special third party software tools (FSL, MINC toolbox, etc.) and multi-purpose applications based upon the MultiModal Medical Imaging software library system and application framework.

All of the software tools developed in our institute have dedicated interfaces which provide a modular brain connectivity analysis work-flow. After standard image processing steps (motion cor-

---

[6] http://fsl.fmrib.ox.ac.uk

[7] http://fil.ucl.ac.uk/spm

[8] http://en.wikibooks.org/wiki/MINC/Introduction

rection, co-registration, segmentation, spatial standardization), functional images are loaded into BrainLOC for brain atlas-based region definition or fParc for data-driven functional parallelization. The resulting region system and corresponding meta-data is than loaded in BrainMOD, which generates sets of Butterworth or wavelet filtered regional time series and exports those in a dedicated format. Graph formulation and graph theoretical analysis and statistical modeling is then performed by the scriptable command-line utilities of the package BrainNetTools, using parallel computing techniques. Temporary and final results are stored in text files. Further analysis can be performed with any of the well-known statistical programming environments (R, MatLab, SPSS, etc.) and visualized in BrainCON. An overview of these software components is presented on Fig. 5.

From the point of view of user requirements, multiple levels of users should be considered: (i) developers of new methods, typically colleagues in the institute and university students, (ii) researchers who apply the system for brain connectivity processing (experts of bioinformatics and medical sciences) and (iii) clinical end-users with limited programming knowledge (biomedical interpretation of results). In the followings, these software components are introduced, focusing on developments carried out as part of my PhD project in order to build our brain connectivity pipeline.

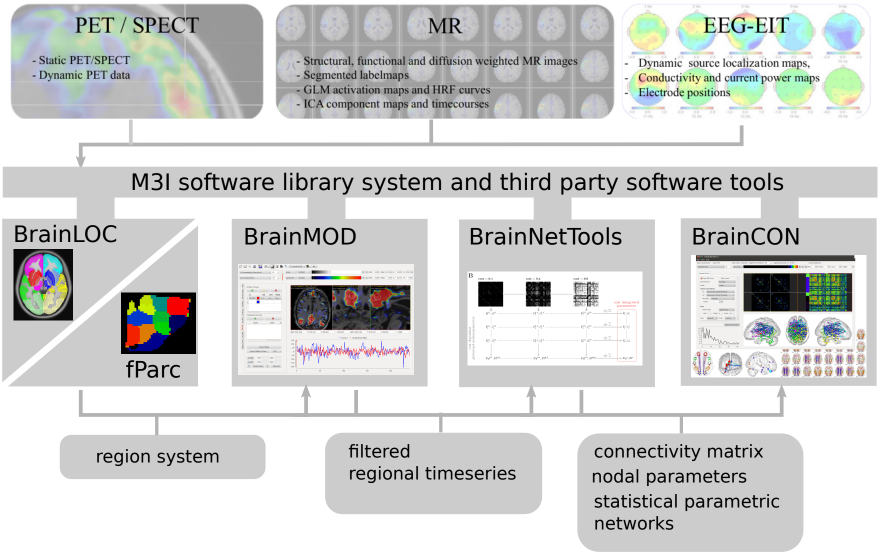

Figure 4. M3I software tools in service of brain connectivity analysis

Multimodal medical imaging data can be processed with a specialized software pipeline, which consists of third party software tools (FSL, MINC toolbox, etc.) and applications based upon the MultiModal Medical Imaging software library system and application framework. All of the software tools developed in our institute have dedicated interfaces to allow a modular brain connectivity analysis work-flow. After standard image processing steps (motion correction, coregistration, segmentation, spatial standardization), functional images are loaded into BrainLOC for brain atlas-based region definition or fParc for data-driven functional parcellation. The resulting region system and corresponding meta-data is than loaded in BrainMOD, which generates Butterworth or wavelet filtered regional time series and exports those in a dedicated format. Graph formulation and graph theoretical analysis and statistical modelling is then performed by the scriptable command-line utilities of the package BrainNetTools, using parallel computing techniques. Temporary and final results are stored in text files. Further analysis can be performed with any of the well-known statistical programming environments (R, MatLab, SPSS, etc.) and visualized in BrainCON.

3.5 BrainLOC: multi-atlas based region analysis and management

Digital brain atlas technique is a valuable and increasingly used tool, applying different purposes in neuroimaging [67,83,84]. Brain atlases can be considered as a database linking spatial loci in the brain to various information, like neuroanatmoy, function, pathological conditions, aging, genetics, etc. Due to the lack of standardized formalism for publishing brain atlas databases, the utilization and the management of the stored information is considerably different in such properties as the applied nomenclature, used file formats or coordinate-system conventions.

During the development of this software tool, our goal was to establish a “uniform brain atlas framework” for handling the most common web-accessible human and small animal brain atlases, and deploy a user-friendly application and utility package, based on this framework and our M3I software system. A number of available atlases (Table 2) were integrated to our database applying a novel standardization scheme to modify, store and describe the different kind of atlas components, including hierarchical, probabilistic (PM), and maximum probability representation (MPM) of brain structures [84]. This standardization allowed us to expand all the adapted atlases with so-called multi-level Maximum Probability Maps, and Volume-of-Interests (VOI) database.

Our proposal for the novel multi-level maximum probability map (MPM) brain atlas representation was published as oral presentations at conferences [77] and [85].

This data representation approach compresses the N volumetric image of regional PMs into an L-level MPM, which consists of a predefined L ($L << N$) number of volumetric image pairs, representing the i^{th} most probable brain structure ($i = 1 \dots L$) in each locus and the corresponding probability, respectively. In BrainLOC, three main services are available: (i) the software computes an interactive localization output, depending on the parameters specified by the user,

(ii) provides means for creating, handling and modifying atlas-based and own VOIs, and (iii) calculates VOI statistics on multi-atlas based region systems.

Table 2. Brain atlases integrated into the multi-atlas database of BrainLOC

PRIMER ATLAS	N	R	template	Image files	Meta-data	license
TALAIRACH	1	280	Talairach	NifTI	txt	BrainMap
MNI STRUCTURAL	50	9	MNI152	NifTI	xml	FSL
ICBM PROBABILISTIC	53-59	50	ICBM452	NifTI	txt	LONI2.0
LPBA-40	40	56	ICBM452	NifTI	txt	LONI2.0
CYTO ANATOMY	10	62	aMNI152	NifTI	mat	FSL
FIBER TRACTS	10	13	aMNI152	NifTI	mat	FSL
ICBM-DTI-81	81	50	MNI152	NifTI	txt	LONI2.0
JHU TRACTOGRAPHY	28	20	MNI152	NifTI	xml	FSL
HARVARD-OXFORD CORTICAL	37	48	MNI152	NifTI	xml	FSL
HARVARD-OXFORD SUBCORT.	37	21	MNI152	NifTI	xml	FSL
CEREBELLAR	20	28	MNI152	NifTI	xml	FSL
OXFORD THALAMIC CONN.	8	7	MNI152	NifTI	xml	FSL
MOUSE MINIMAL DEF.	11	52	LONI Mouse	NifTI	txt	LONI2.0
MOUSE NEONATAL MRI	8	13	LONI P0 Average	NifTI	txt	LONI2.0

N denotes the number of subjects used while creating the atlas. R denotes the number of structures the atlas consists of. The primer atlases can have either deterministic or probabilistic label maps (which is equivalent to MPM). Some deterministic atlases do not have label map at all. The structures of probabilistic atlases are usually represented by probabilistic structure maps and either uni- (left and right separately) or bilaterally (left and right together). The individual atlases have various coordinate-spaces with a corresponding template. The implementation of the mapping function can also differ: in some cases the necessary data is stored in a simple text (txt), or Xml file while in others a MatLab structure carries it in the software's own format (.mat). Finally, the base data is often stored in NIfTI file format but not always. The proper license is also given in the table. For more information about it please consult the competent licensure advisor. In several cases the uniforming procedure of one primer atlas was resulting in more adaptive atlases.

3.6 fParc: Data-driven Markov Random Field Segmentation with graph-cuts

Brain atlas-based region definition has an obvious disadvantage: atlases represent the population-level average neuroanatomy and are not directly linked to individual-level brain function. We aimed to develop a data-driven segmentation approach which defines regions based on the fMRI data itself, so that time series in the same region have a maximal, while time series in different regions have minimal temporal coherence. Such an algorithm might solve the problems of *mixed internal inputs* (two or more neural sources within one region) and *shared external input* (one neural sources gets divided into multiple regions) [26]. Our implementation is based on the work of Ryali et al. [57] with the modifications:

- the number of regions is predefined instead of estimated,
- the volume of regions is regulated by an appropriate constrain (their variance is minimized).

Generative model for parcellation

According to Eq. (5) (section 1.3), let $Y = \{\mathbf{y_i}\}_{i=1}^{M}$ be the preprocessed and *normalized* voxel time series ($||\mathbf{y_i}|| = 1$). Furthermore, let $X = \{x_i\}_{i=1}^{M}$ be the unknown labels of each voxel ($x_i \in \Lambda, \Lambda = \{1, 2, \ldots, L\}$ is a discrete label set).

The preprocessed and normalized BOLD fMRI time series belonging to the same label $x_i = l, L \in \Lambda$ is modeled in each voxel by a T-variate von Mises-Fisher distribution [86]:

$$f(y_i | x_i = l, \mu_l, \kappa_l) = c(\kappa_l) e^{\kappa_l (\mu_l y_i)}, i = 1, 2, ..., M, \tag{7}$$

where μ_l and κ_l are the mean direction and concentration parameters of the distribution and $c(\kappa_l)$ is the normalizing constant. Methods for estimating $c(\kappa_l)$ can be found in [57].

The prior distribution of unknown cluster labels X is than modeled as a discrate Markov Random Field (MRF) [87]. Let $S = \{1, 2, \ldots, N\}$ be the set of indices and $N = \{N_i, i \in S\}$ be the given neighbourhood system whereein N_i is the set of sites neighboring the voxel i. Then the random field X is an MRF on S with a neighborhood system N if and only if [88]:

$$P(X) > 0, \tag{8}$$

$$P\left(X_i | \{X_j\}_{j=1, j \neq i}^{M}\right) = P(X_i | X_{N_i}), \tag{9}$$

By the Hammersley-Clifford theorem [88], an MRF can be represented by a Gibbs distribution:

$$P(X) = \frac{1}{Z} e^{-(U_S(X)+U_v(X))}, \tag{10}$$

where, Z is the normalizing constant, $U_S(X)$ is the energy function which imposes spatial regularization. In the original work $U_S(X)$ was defined based on the Potts potential with weigh β_l [57] which makes the preference of neighboring voxel to have the same label. To penalize regions with different volume, **we extended this energy function by incorporating the function:**

$$U_v(X) = \beta_s \sum_{i=1}^{L} \left(\frac{M}{L} - \sum_{j=1}^{M} \phi_i(x_j) \right)^2 \tag{11}$$

where:

$$\phi_i(x_j) = \begin{cases} 1 & \text{if} \quad x_j = i, \\ 0 & \text{otherwise.} \end{cases} \tag{12}$$

and β_l is the weight for this regional volume constraint.

The posterior distribution of X given the data Y and model parameters $\Theta = [\beta_s, \beta_l, \{\mu_l, \kappa_l\}]$

$$P(X|Y,\Theta) \propto \prod_{i=1}^{M} p(y_i|x_i) P(X) \tag{13}$$

and can be represented by the equivalent Gibbs distribution:

$$P(X|Y,\Theta) = \frac{1}{Z} e^{-U_{X|Y}(Y,X)} \tag{14}$$

where Z is the normalizing constant. The posterior potential $U_{x|Y}(Y,X)$ can be represented in terms of three components: (i) data cost ($U_D(Y)$), (ii) smoothness cost ($U_s(X)$, based on the Potts potential) and volume cost ($U_v(X)$). The data cost is given by $U_D(Y) = -\sum_{i=1}^{M} logp(y_i|x_i)$.

The estimation of Θ latent labels and parameters were implemented analogous to [57].

Cluster labels and model parameters are estimated by an iterative expectation maximization (EM) procedure wherein the latent cluster labels are computed using α-expansion, a state-of-art graph cut solver (see [89] for details).

fParc was implemented in C++, based on the M3I software library system and validated on simulated and real data, similar to as in [89] (data not shown).

3.7 BrainMOD: Multi-purpose Medical Image Processing and Visualization

The main goal of BrainMOD is the interactive state of the art 2D and 3D visualization of post-processed multi-modal medical imaging data with aid of user-friendly graphical user interface. The imaging modalities involved are: PET, MRI, EEG, EIT. The visualization functionality should focus on techniques that can take advantage of multi-source post-processed data and help interpreting intra-modal relationships. Besides 2D and 3D visualization techniques, BrainMOD also explicitly handles 4D data-sets.

BrainMOD was developed under the scope of the Central Nervous System Imaging (CSI) project of the ENIAC consortium. The above described purposes of BrainMOD are completely coherent with the corresponding work package tasks of the ENIAC CSI project. The project ended in October 2013. The developed software gained honorable mention by the review board assigned by the European Committee in the project review report.

The whole software specification document is attached in Appendix A*III*.

Besides its role as a common data processing and visualization platform in the CSI project, BrainMOD was designed to be a multi-purpose multimodal medical image analysis and visualization tool and is playing an important role in many research project at the

University of Debrecen as well as at our partner institutes at the University of Kaposvár, Gedeon Richter Plc. and the Kempenhaghe Expertise Center for Epileptology, Sleep Medicine and Neurocognition in Heeze, the Netherlands.

By implementing significant modifications, the software was extended with features required for fMRI-based brain connectivity analysis. These features involve:

- interface for reading and handling region systems as exported by BrainLOC and fParc,
- handling large 4D datasets (>2Gb) by a dedicated memory swapping procedure specially developed for volumetric image data,
- multi core computation of regional descriptive statistics, based on OpenMP[9],
- explicit curve management and visualization
- temporal filtering approaches and multiresolution wavelet decomposition on time-series data (maximum overlap discrete wavelet transformation [90] with a Daubechies least asymmetric wavelets, default: LA(8) wavelet), reimplemented to exploit multi-core capabilities (OpenMP),
- curve export for BrainNetTools,
- toolbox system with automatically generated GUI based on factory design pattern[10], for the use of external software and scripts.

The software was build upon the M3I software library system. The corresponding developments were published in [78] and [91].

---

[9] www.openMP.org

[10] stackoverflow.com/questions/5120768

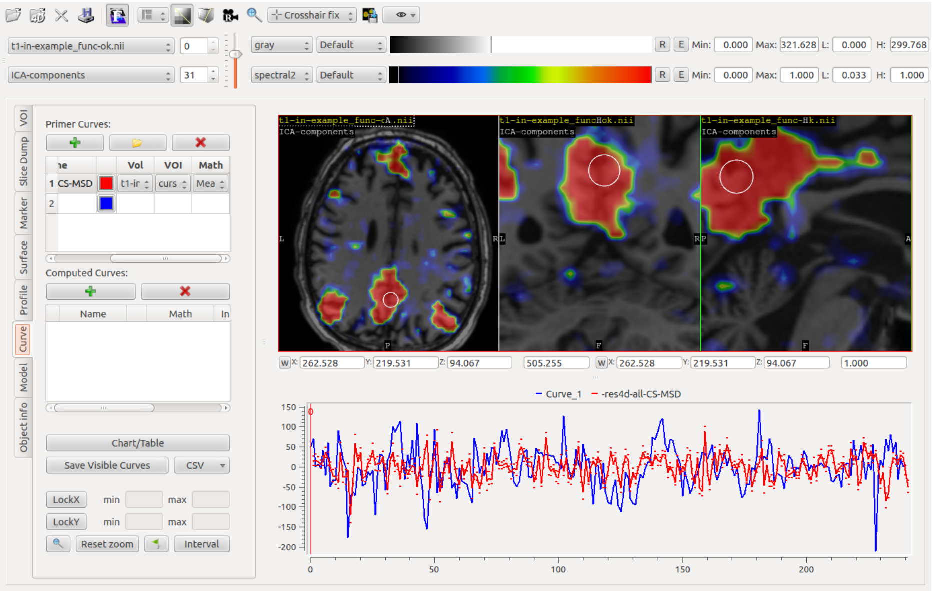

t1-in-example_func-ok.nii 0 gray Default Min: 0.000 Max: 321.628 L: 0.000 H: 299.768

ICA-components 31 spectral2 Default Min: 0.000 Max: 1.000 L: 0.033 H: 1.000

t1-in-example_func-cA.nii ICA-components

t1-in-example_funcHok.nii ICA-components

t1-in-example_func-Hk.nii ICA-components

X: 262.528 Y: 219.531 Z: 94.067 505.255 X: 262.528 Y: 219.531 Z: 94.067 1.000

Figure 5. Screenshot of BrainMOD
The time-course of the so-called default-mode resting-state brain network (red blobs in the top viewer and red curve in the bottom plot) and an on-line computed curve based on the cursor environment (blue curve). On the GUI, the "Curve" Toolbox is selected, which is only one of the 8 toolboxes in BrainMOD.

3.8 BrainNetTools: Modular Brain Connectivity Analysis Toolkit

The central element of the software system for our brain connectivity analysis work-flow is the software package BrainNetTools: a modular, scalable collection of command-line programs and scripts. This package implements all the features needed for estimating connectivity matrices from regional BOLD time series and analyze it by means of complex graph theory. The modular architecture allows rapid integration of new methods to our work-flow and provides a platform for methodological research and development. Due to the considerable computational complexity, several components of the system are parallelized and optimized for use on high-performance computing cluster.

The components of BrainNetTools were validated by the following external software: Brain Connectivity Toolbox [11] (release 29/03/2012), igraph[12] (v0.6 R-package), wavelets[13] (v0.2-7 R-package) and NetworkAnalysis[14] (v0.3-1 R-package). The software tool was published in [16], [92] and [79].

Below we discuss some of the most important algorithms and concepts implemented in BrainNetTools.

Nuisance signal correction techniques

Nuisance signal correction techniques aim to reduce artifactual components in the regional BOLD signals by evaluating a linear regression model with one or more confounder variables which are believed to describe the temporal structure of noise and considering the residuals as corrected signal. The confounder variables can be acquired from multiple sources, for instance by measuring physiological parameters during scan (pulse-oxymetry, respiration monitoring). Alternatively, it can be extracted form the data itself, for example by image realignment-based motion correction procedures, or other advanced methods which try to identify spurious sources of variation from so-called noise-ROIs (see [36] for a description of one of the implemented techniques). In BrainNetTools, we have implemented more than 10 different nuisance correction technique.

Estimating connectivity strength

Functional connectivity is defined [27] as synchronized neural activity between two brain regions. In BrainNetTools, sychronity between

---

[11] http://www.brain-connectivity-toolbox.net

[12] http://igraph.sourceforge.net

[13] http://cran.r-project.org/web/packages/wwavelets

[14] http://cran.r-project.org/package=NetworkAnalysis

BOLD time series can currently be calculated by Pearson correlation, partial correlation, coherence and phase synchronization.

Graph theoretical analysis of functional connectivities

In graph theory, the mathematical abstraction of a network is a G graph containing a set of N nodes and M edges. This graph can be represented as an $N \times N$ square A adjacency matrix with elements $a_{ij} = 1$ or 0, depending on whether an edge does (1) or does not exists (0) between nodes i and j. In the case of weighted networks the W connectivity/weight matrix containing w_{ij} elements represents the strength of connections between nodes i and j. In MRI-based functional brain network analysis the adjacency and weight matrices are zero-diagonal, symmetric matrices $(wij = a_{ij} = 0, w_{ij} = w_{ji}, a_{ij} = a_{ji})$ since modeling regional self-connections $(i = j)$ and directed regional connections $(w_{ij} \neq w_{ji}, a_{ij} \neq a_{ji})$ are meaningless. These matrix properties correspond to undirected binary (so called unweighted) or undirected weighted graphs, depending on the used edge model (binary, weighted). In the case of weighted functional brain network without losing generality we assume that the weights of edges (i.e. the strength of connections) lie in the unit interval, [0,1].

Measurement of graph sparsity

The number of maximum edges of an undirected graph is $M_C = N(N-1)/2$, i.e. the number of elements of the upper-triangle of adjacency or weight matrix. The C index stands for ”complete graph” in which every pair of nodes are connected. In the case of binary undirected graphs the

$$K(G) = \frac{M}{M_C} \tag{15}$$

ratio defines the edge density or wiring cost of G. It is obvious that this parameter lies in the unit interval, $[0, 1]$, while the number of edges of empty and complete graphs is 0 and M_C, respectively.

Substituting M and M_C into formula of $K(G)$:

$$M = \frac{1}{2} \sum_{i,j=1,\ldots N, i \neq j} a_{ij} \tag{16}$$

and so

$$K(G) = \frac{\sum_{i,j=1,\ldots N, i \neq j} a_{ij}}{N(N-1)} \tag{17}$$

results in the fact that the wiring cost is the mean of values of the off-diagonal elements of the adjacency matrix.

Network topology: global graph features

Using the described graph theoretical notation we can formulate a large set of parameters that characterize the global, nodal or modular properties of the investigated networks, as reviewed by Rubinov and Sporns [93]. It is known from the literature that functional human brain networks show small-world characteristics, therefore during the implementation we focused on quantifying only those nodal and global parameters that may have an influence on this property. Latora and Marchiori [94] introduced the efficiency-based characterization of small-world networks, which, due to its computational benefits, was proved to be more effective than the classical characteristic path length and clustering coefficient based calculation methods [95]. The efficiency was introduced as the measure of the effectiveness of information exchange between nodes, while the average efficiency of nodes of a G graph was defined as global efficiency (E_g), which gives a normalized measure (lies in $[0, 1]$) of the information transfer efficiency of parallel systems. The normalized local efficiency (E_l) of the network measures how efficient the local communication between first neighbors of a node is if this node is faulted or removed (fault tolerance). Latora and Marchiori also showed that the small-world behavioral network has high global and local efficiency [94].

Nodal parameters of unweighted graphs

The k_i node degree [93] is defined as the sum of edges of node i:

$$k_i = \sum_{j=1...N, i \neq j} a_{ij} \tag{18}$$

The efficiency coefficient of the path (path efficiencies) between node i and j is defined as the inverse of the l_{ij} shortest distance between these nodes [93]. The shortest path length l_{ij} between nodes i and j means the minimum of all possible path lengths between nodes i and j, and can be calculated from the adjacency matrix by Dijksra's [96] or Floyd's [97] algorithms. Using these definitions the efficiency of node i is defined as the average of the path efficiencies of the given node:

$$e_i = \frac{1}{N-1} \sum_{j=1...N, i \neq j} \frac{1}{l_{ij}} \tag{19}$$

Global graph parameters of unweighted graphs

Global efficiency E_g is given as the mean of nodal efficiencies and gives a normalized measure (lies in $[0, 1]$) of the information transfer efficiency of the network:

$$E_g = \frac{1}{N} \sum_{i=1...N} e_i \tag{20}$$

Local efficiency of an unweighted graph is defined as the average global efficiency of sub-graphs of nodes, thus, it measures how efficient the local communication is between the first neighbors of a node if this node is faulted or removed:

$$E_l = \frac{1}{N} \sum_{i=1...N} E_g(G_i) \tag{21}$$

where G_i denotes the subgraph composed from the neighbors of node i, and by definition does not contain node i.

Cost-integrated measurement of topological metrics

One of the critical points of functional brain network analysis is the connection (edge) selection or the thresholding procedure. The fundamental aim of this process is to eliminate weak connections from the graph representation of network by an arbitrarily chosen weight threshold. The result can be a weighted graph containing only edges with higher weight than the applied threshold or it can be an unweighted graph containing only thresholded edges. Thresholding will change the wiring cost of graphs, or in other words, it changes the topology of the investigated network.

In the functional brain network assays we have an illusory solution to avoid this problem if we use the evaluated, unthresholded primary networks for any population level analysis. However, the primary networks differ in their average correlation coefficients and they also differ in their mean weights and wired-costs [98], which makes difficult to compare their topology parameters. Although, the adaptive thresholding technique [99] could guarantee the same weighted or unweighted wired cost for all networks in the population by uniquely selected thresholds, it generates new questions: which wired cost is the best for the analysis and how the selected cost affects the results? Since there is currently no consensus in the literature regarding selection of threshold for weighted graph analysis we applied a *cost-integrated technique* as introduced by Ginestet et al. in [100]. Following the definition of this paper we calculate the cost-integrated values of any {X} topological parameter of the graph {G} by this formula:

$$X^* = \sum_{k \in \Omega} X(G^k) p(k) \tag{22}$$

where k is a cost value from the Ω set (set of all possible cost values), and $p(k)$ the denotes the probability of the occurrence of k cost. The G_k is an unweighted graph having k wired cost and it is generated from G by an appropriate threshold and $X(G_k)$ is the value of the X topological parameter calculated on G_k (See table 7). We assumed that k has uniform distribution, which means that the $p(k) = 1/M_c$, so the cost-integrated version of any X can be calculated as follows:

$$X^* = \frac{1}{M_c} \sum_{k=1 \dots M_c} X(G^k) \tag{23}$$

Typically the number of nodes is greater than 80 ($M_c > 3160$). In these cases a Monte-Carlo (MC) based estimation can be applied to calculate cost integrated values (described also in [100]). According to our preliminary analysis, 200 MC-sample gave correct E_g and E_l values, so this sample rate was set as default in the software. MC sampling is parallelized and optimized for supercomputer use with the aid of OpenMPI[15] technique.

---

[15] www.open-mpi.org

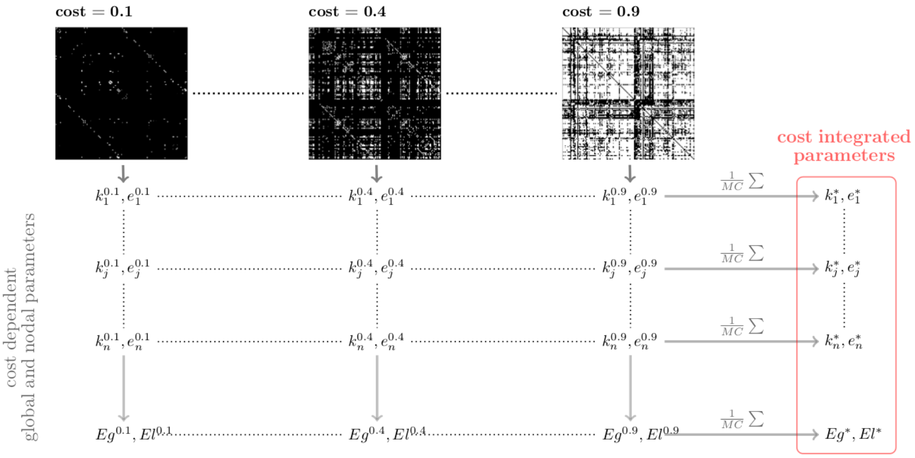

Figure 6. Schematic overview of the cost-integration technique

Three adjacency matrices are shown with wired costs 0.1, 0.4 and 0.9. These matrices were generated from the weighted connectivity matrix by different weight thresholds. Vertical gray arrows represent the calculation procedure of nodal and global network parameters at different cost levels. The horizontal gray arrows demonstrate the final step of Monte-Carlo based cost-integration procedure in which the summed parameters are divided by the integration steps (MC).

3.9 BrainCON: Brain Connectivity Visualizer and Graph Analysis Tool

Brain connectivity analysis requires special visualization techniques, because on one hand, standard neuroimaging visualization software tools are not able to handle graph visualization and on the other hand, standard graph and network visualization tools are not able to display neuroanatomical correlates. Although there are some recently developed software for brain connectivity visualization, our experiences pointed to the conclusion that these tools are either not general and flexible enough, or have a poorly design graphical interface which might mean a significant drawback in clinical collaborations.

BrainCON was designed to be a user-friendly, real-time connectome visualizer, which is able to handle large datasets with appropriate memory management procedures, and beneath real-time display, produces high resolution image files for scientific publishing purposes. Besides visualization features, BrainCON is able to compute several graph parameters in quasi real-time by utilizing multi-core parallelization implemented using the POSIX Threads Programming[16] (pthread) standard. Graph visualization was programmed in OpenGL, the GUI was developed in Qt and the whole application was based on the bcApplication framework of the M3I software library system.

For BrainCON, multiple display modes have been developed:

- quasi-3D anatomical plot: 3D spheres and lines denote nodes and links, rendered above a 2D ”glass brain” which helps interpreting anatomical meaning.
- 10-20 system plot: developed typically for EEG-based electrode-space connectivity analysis. Nodes are placed corresponding to the schematic structure of the 10-20 electrode system.
- circular plot: to a clearer display of dense graphs, the position of nodes does not follow the true anatomical projection, instead, nodes are rendered in concentric circular positions, with cortical structures in the outer and subcortical structures in the inner circle.
- abstract plot: the position of the nodes is dependent on some parameters of the graph, thus visualizes also structural pattern and modularity (under development).

In all of these display modes, the size and the color of nodes and edges can denote any graph parameter. The software explicitly supports the display of statistical parametric networks (SPNs). By SPNs,

---

[16] www.computing.llnl.gov/tutorials/pthreads

nodal and edge parameters are results of an arbitrary population-level statistical test.

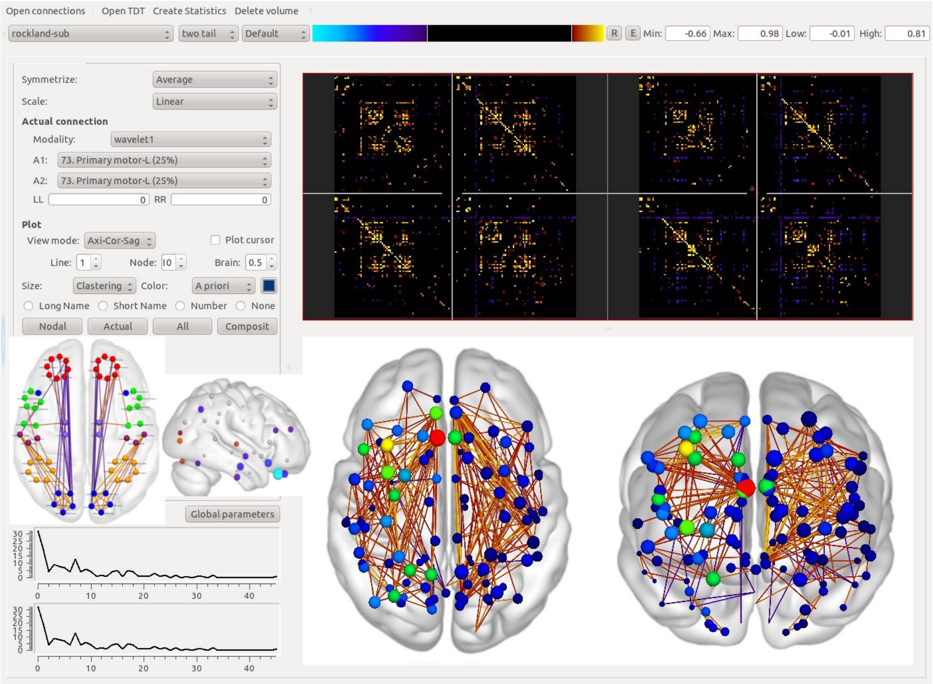

rockland-sub | two tail | Default | Min: -0.66 | Max: 0.98 | Low: -0.01 | High: 0.81

Symmetrize: Average
Scale: Linear
Actual connection
Modality: wavelet1
A1: 73. Primary motor-L (25%)
A2: 73. Primary motor-L (25%)
LL 0 RR 0
Plot
View mode: Axi-Cor-Sag ☐ Plot cursor
Line: 1 Node: 10 Brain: 0.5
Size: Clastering Color: A priori
○ Long Name ○ Short Name ○ Number ○ None

Figure 7. Screenshot of the BrainCON software
In the top viewer thresholded connectivity matrices (population-level statistical parametric networks) are displayed. On the bottom panel, quasi-3D anatomical "glass brain" visualizations of the network are plotted. The graphs on the bottom left panel show the degree-distribution of the thresholded network.

4 Materials and Methods

4.1 Autism Brain Imaging Dataset Exchange

Analysis was performed on the resting-state fMRI data of 184 patients obtained from the Autism Brain Imaging Dataset Exchange database [72, 101, 102] (ABIDE). All of the images were acquired at the NYU Langone Medical Center using a 3 Tesla Siemens Magnetom Allegra syngo MR 2004A. A T1-weighted sagittal MP-RAGE structural image was obtained (TE=3.25 ms, TR=2530 ms, TI=1100 ms, flip angle=7°, 256 slices with 1.3x1x1.3 mm voxels). Functional images were obtained using a BOLD contrast sensitive gradient echo echo-planar sequence (TE=15 ms, flip angle=90°, in-plane resolution=3x3mm; volume TR=2000 ms). Whole-brain coverage for the functional data was obtained using 33 contiguous interleaved 4mm axial slices. During the resting-state fMRI scan, most participants were asked to relax with their eyes open, while a white cross-hair against a black background was projected on a screen. However, data were also included for some individuals who were asked to keep their eyes closed; and, in a few cases, participants closed their eyes regardless of instructions to keep them open.

The population sample consisted of 79 patients with autism spectrum disorders (7.1-39.1 years) (53 Autistic Disorder, 21 Asperger's Disorder, 5 Pervasive Developmental Disorder-Not Otherwise Specified) and a group of 105 typical control subjects. The distribution of age and gender was not significantly different between the groups).

Data collection for the ABIDE dataset was approved by the institutional review boards of the New York University School of Medicine and New York University. Prior to participation, written informed consent and assent (for participants>18 years) were obtained from all participants and their parents/legal guardians (for participants<18 years). Participants received monetary compensation for completing the study. In this study, the patient data were analyzed anonymously.

4.2 Image Preprocessing and Definition of Regions-of-interest

Image data processing was performed in the conventional way described in current fMRI literature (Fig. 8 A.), except novel steps in the pipeline (estimating voxel-wise motion, regional displacement timecourses, regional DVARS, graph formulation, Fig. 8 B.))

Image Preprocessing

FMRI time series were co-registered and frame-wise estimation of head displacement was performed using FSL McFlirt [35, 103]. Matrices defining the rigid-body (three translation and three rotation parameter) transformation that fit each frame to the reference frame (at the middle time-point) were saved for further use. The first five volumes of each dataset were discarded from further analysis to allow for T1 equilibration effects. BET was used to remove non-brain areas [58]. The resulting pre-processed fMRI data were linearly co-registered to the brain-extracted anatomical image, and then, spatially standardized to the MNI152 space using the FLIRT and FNIRT utilities [104] of the FSL package, to achieve spatial correspondences for group analysis. Since further processing steps utilized averaged regional time courses, no smoothing was applied on the images.

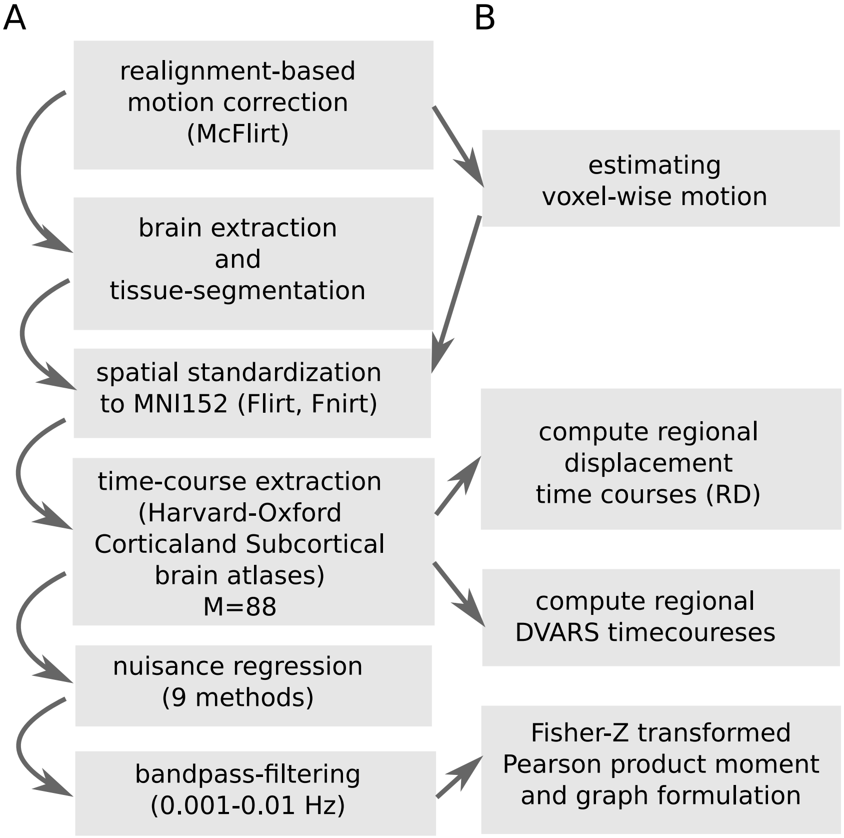

Figure 8. Image data processing pipeline

ROI definition

In order to improve the signal-to-noise ratio and reduce the amount of data to analyze, all regional timecourses (regional BOLD signal, temporal derivate of its root mean squared variance, regional displacement) and corresponding correlation coefficients presented in this paper were drawn from a set of ROIs (M=88) that were defined based on the Harvard-Oxford Cortical and Subcortical brain atlases [105]. Probability maps for all regions were accessed and region borders were delineated by retaining voxels with a probability greater than 25%. Voxels associated with multiple regions (in case of overlapping regions) were assigned to the region in which the underlying probability was higher. To avoid very small regions with poor signal-to-noise ratio, ROIs having a volume less than 30 cm^3 were merged into neighboring ROIs. A complete list of the brain regions and the modifications are summarized in Table 7. Fig. 9 presents the axial projection of brain regions in the glass-brain plot used to demonstrate results.

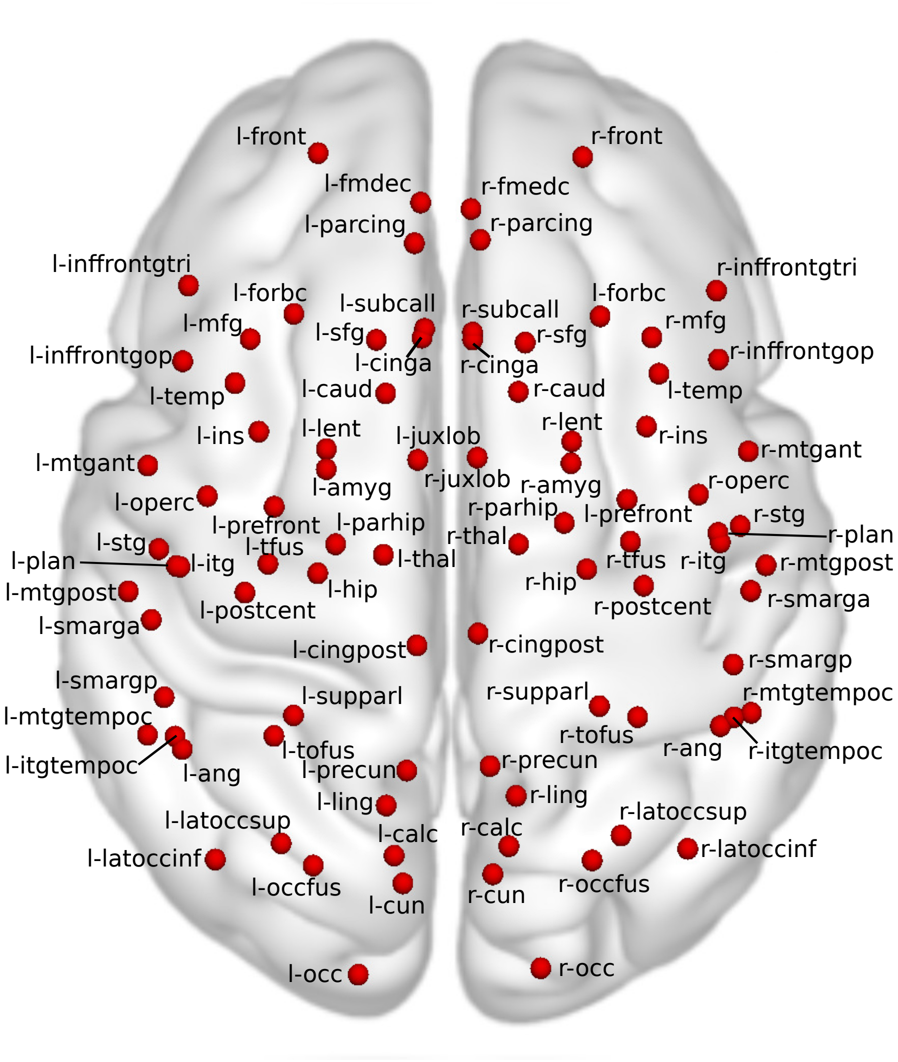

Figure 9. Brain atlas regions

Short names of atlas regions in the glass brain plot used to demonstrate results. Full names and additional information about regions can be seen in Table 7 of Appendix A*I*. Red spheres imply the axial projection of the center of mass of brain regions. Note that this plot does not indicate the axial depth of the regions.

4.3 Voxel-wise Motion Artifacts

Calculation of voxel-wise displacement

With an in-house-developed utility based on the m3i software library system [92], transformation matrices outputted by McFlirt were converted to world coordinate origin. The respective inverse transformations were applied to each frame of the fMRI time series and the root mean squared voxel position change in world coordinates was calculated for each voxel of each frame. The first derivate of the resulting local displacement time series was saved in NIfTI format dynamic images in the same space as the fMRI time series (see Fig. 10 for demonstrative images), and then realigned to standard space.

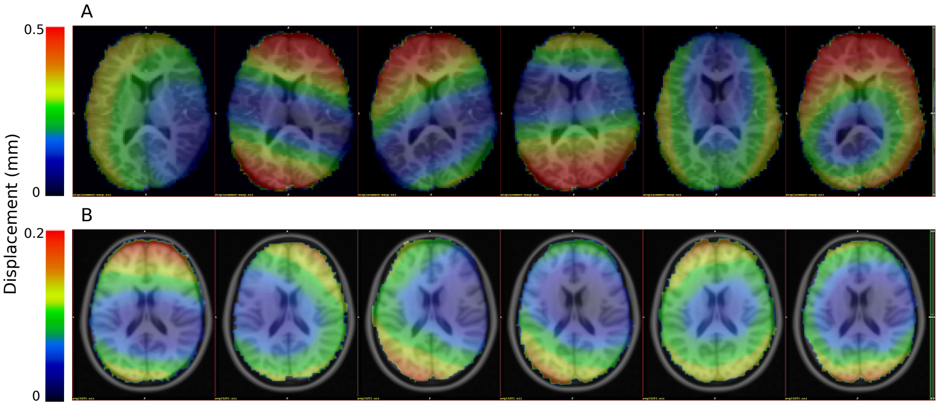

Figure 10. Voxel-wise characteristics of head motion during an fMRI scan
Examples of different patterns of voxel-wise displacement within the time frames of one illustrative subject (A) and temporally averaged voxel-wise displacement of six illustrative subjects (B).

Calculation of regional and frame-wise displacement

We defined two metrics of displacement: regional and frame-wise displacement (RD and FD). RD time-courses were calculated as averaged voxel-wise displacements over ROIs, while FD is the analogous measurement for the entire brain. This method of calculating FD and RD is analogous to the parameter FD_{vox} described in [45].

Quantification of global and regional BOLD intensity change

While DVARS (D referring to temporal derivative of timecourses and VARS referring to RMS variance over voxels, first introduced in [106]) indexes the rate of change of BOLD signal across the entire brain at each time-point of the data, Regional DVARS (RDVARS) shows the same rate for each ROI:

$$DVARS(Y)_t^R = \sqrt{\langle (y_i(t) - y_i(t-1))^2 \rangle^{(R)}} \tag{24}$$

where $y_i(t)$ is the image intensity at locus i on frame t, angle brackets $\langle \bullet \rangle^{(R)}$ denote the spatial average over all voxels i within ROI R ($R = 1 \ldots 88$) and $t = 2 \ldots T$ where T is the number of time-frames. In order to effectively relate RDVARS to RD, RDVARS was calculated on the time series following re-alignment, but prior to confound regression and filtering.

Investigating the effect of regional displacement on DVARS

We reproduced results showing global motion-related BOLD changes [41, 43, 45] by computing the correlation coefficient between FD and DVARS. Then, to distinguish global from local effects, we defined two measures, residual RD and residual RDVARS (denoted with ΔRD and $\Delta RDVARS$), as follows:

$$\Delta RD_t^{(R)} = RD_t^{(R)} - FD_t \tag{25}$$

and

$$\Delta RDVARS_t^{(R)} = RDVARS_t^{(R)} - DVARS_t \tag{26}$$

where $t = 2 \ldots T$, T is the number of time-frames and R ($R = 1 \ldots M$) identifies the region. After computing these measures for every subject and every ROI, we computed their correlation coefficient and investigated whether it depends on the degree of the global motion-BOLD relationship among subjects.

4.4 Functional Connectivity Processing and Graph Formation

For rs-fcMRI analysis, additional preprocessing steps were utilized on regional BOLD timecourses to reduce spurious variance that was unlikely to reflect neural activity. These steps included: (i) multiple regression of nuisance variables; and (ii) a temporal band-pass filter on residual data using a standard fourth-order Butterworth band-pass filter, retaining frequencies between 0.01 and 0.1 Hz.

The detailed data processing steps involved in the following strategies are discussed in the relevant works. Here, we only summarize the protocols based on basic criteria, such as the sources of nuisance signal, the number of such signal time-courses and whether global signal regression was performed.

1. NOREG: No nuisance regression,
2. WMCSF: average BOLD signals of eroded white matter and cerebrospinal fluid ROI-s, segmented using FAST [58],
3. GSREG: regression of whole-brain global signal as a covariate,
4. COMPCOR: Nuisance regression of five principal components of a noise ROI, defined based on the temporal signal-to-noise ratio, as proposed in [36],
5. NOREG+M6: NOREG + six motion parameters,
6. WMCSF+M6: WM+CSF regression + six motion parameters,
7. GSREG+M6: GSREG + six motion parameters,
8. COMPCOR+M6: COMPCOR + six motion parameters,

9. SAT36: A 36-parameter nuisance regression model proposed in [40] (incorporating global signal regression).

To ensure that neighboring regional BOLD time courses do not show spurious increase in connectivity strength, no smoothing was applied. Connectivity strength between pairs of preprocessed regional time series were calculated as the Fisher-Z transformed Pearson product moment ($z = atanh(\rho)$), and ordered into 88x88 correlation matrices for each subject (henceforward referred to as C_i for subject i) and for each nuisance regression technique, resulting in a total of 184*9= 1656 matrices.

4.5 Group Formation and Second-level Statistical Analysis

Group formation

One subject with extreme in-scanner motion (average FD greater than 0.7mm) was excluded from further analysis. The remaining 183 subjects were arranged into various groups:

- Autistic and normal control groups. Based on the clinical neuropsychological diagnostic tests for autism, as detailed in the original study description of the ABIDE dataset [72]. A group of 49 autism subjects and a neurotypical control group (n=105) were defined.

- Groups of healthy control subjects with different average voxel-wise displacement patterns, based on the group mean voxel-wise displacement maps. The healthy control group was divided into two sub-groups randomly. Temporally averaged standard-space voxel-wise displacement maps were averaged across subjects of both sub-groups separately and the spatial Pearson correlation coefficients for the group-mean voxel-wise displacement maps were calculated between the sub-groups (henceforward referred to as ρ_{WD}). This random group formation defined by Algorithm 1 was repeated 5000 times. The histogram of observed ρ_{WD} values can be seen in Fig. 17 of Appendix A*II*. Group-pairs were chosen so that the corresponding ρ_{WD} values are relatively low, meaning that the subjects in one sub-group tend to have different voxel-vise displacement patterns than in the other. We chose eight pairs of groups with ρ_{WD} coefficients between 0.89-0.95 (Table 3). ρ_{WD} was also computed for the autism-related group-pair.

Algorithm 1: Random group formulation

```
Data: D: N subjects' 3D voxel-wise displacement maps
Result: a simulated sample for estimating the distribution of $\rho_{WD}$ by random
        grouping
group : vector of labels, consisting of N/2 times "A" and N/2 times "B";
$\rho_{WD}$ : vector of real;
for i in 1 to maxiter do
    permute group;
    init 3D maps A and B with 0s;
    for j in 1 to N do
        if group[j] equals "A" then
            foreach voxel in A: A = A + D[j]
        else
            foreach voxel in B: B = B + D[j]
    foreach voxel in A: A = A / N / 2;
    foreach voxel in B: B = B / N / 2;
    $\rho_{WD}[i]$ = spatial correlation of 3D maps A and B;
return $\rho_{WD}$ ;
```

The healthy control group was divided into two sub-groups randomly. Temporally averaged standard-space voxel-wise displacement maps were averaged across subjects of both sub-groups separately and the spatial Pearson correlation coefficients for the group-mean voxel-wise displacement maps were calculated between the sub-groups. The Histogram of ρ_{WD} represents the distribution of the inter-group correlation of voxel-wise motion patterns (See Fig. Fig. 17 in Appendix A*II.*)

Table 3. Voxel-vise displacement-dependent groups

ρ_{WD}	FA_1	FA_2	$p_{FA_1=FA_2}$	$\max VIF^{STD}_{GRP}$	$\max VIF^{STD+RDI}_{GRP}$
0.89	0.06 (±0.03)	0.08 (±0.04)	0.011	1.11	1.2
0.90	0.07 (±0.04)	0.07 (±0.03)	0.46	1.24	1.09
0.91	0,07 (±0.03)	0.07 (±0.04)	0.99	1.36	1.00
0.92	0.07 (±0.03)	0.07 (±0.04)	0.11	1.37	1.08
0.93	0.07 (±0.03)	0.08 (±0.04)	0.12	1.41	1.07
0.94	0.07 (±0.02)	0.07 (±0.04)	0.78	1.38	1.1
0.95	0.07 (±0.03)	0.07 (±0.04)	0.67	1.23	1.02
0.96	0.07 (±0.03)	0.07 (±0.03)	0.82	1.21	1.01

Formation of voxel-wise displacement related groups. N=105 healthy control patients were divided into group-pairs randomly, 5000 times. Eight pairs of groups were chosen so that correlation between the group-mean voxel-wise displacement maps (ρ_{WD}) were 0.89, 0.9, 0.91, 0.92, 0.93, 0.94, 0.95 and 0.96. FA_1 and FA_2 denotes the mean (± standard deviation) FD of the group-pairs (in mm) and $p_{FA_1=FA_2}$ denotes the probability that the groups are identical regarding FD (obtained using permutation test). MaxVIF^{STD}_{GRP} and max$VIF^{STD+RDI}_{GRP}$ denotes the obtained maximal variance inflation factor (VIF) (throughout all connections) corresponding to the grouping factor, in models STD and STD+RDI, respectively. None of the groups introduce multicollinearity in the models. (however there is a slight difference between the FDs of the group-pairs with a spatial voxel-wise displacement correlation of 0.98).

Group comparisons

Group comparisons were performed by fitting Generalized Linear Models (GLM) [107] and arranging statistical parameters into differential statistical parametric networks (SPNs) [108]. We investigated the effect of the grouping variable on functional connectivity strength. Additional covariates that might significantly influence functional connectivity, and thus, disturb comparison, were also included in the models. These are phenotypic covariates describing age, full-scale Wechsler Abbreviated Scale of Intelligence (full IQ), gender, and subject-specific mean FD. All covariates in each applied model were zero-centered. Connectivity strength is therefore modeled as:

$$c_i^{(A,B)} = \alpha + \beta GRP_i + \gamma_1 AGE_i + \gamma_2 FIQ_i + \gamma_3 SEX_i + \gamma_4 FD_i + \epsilon_i \tag{27}$$

where $c_i^{(A,B)}$ is the measured connectivity strength between regions A and B for subject i (element at the A^{th} row and B^{th} column of the C_i matrix), GRP_i is the dummy variable coding groups to compare, and AGE_i, FIQ_i, SEX_i and FD_i are the aforementioned subject-specific confounder variables, α, β and γ_is are the coefficients to estimate, and ϵ_i is the the i^{th} independent identically distributed normal error. Models were fitted utilizing an iteratively reweighted least squares (IWLS) algorithm. T-scores and p-values of the effect of interest were obtained by dividing the β coefficient of interest by the estimated standard error.

Regional Displacement Interaction - RDI

According to our hypothesis, differences in the mean RDs of region-pairs A and B may have an important effect on the population-level distribution of correlation coefficients corresponding to the given connection. This can be tested by adding new terms to the linear model: the temporally averaged RDs of regions A and B and, furthermore, the interaction term between these two covariates. Since RDs are strongly correlated with each other and with the global FD, we introduced $\overline{\Delta RD}$ which is an alternative to the average RD, but with FD subtracted, in order to avoid multicollinearity in the model. Accordingly, $\overline{\Delta RD}$ for subject i and region R can be defined as follows:

$$\overline{\Delta RD}_i^{(R)} = \frac{\sum_{t=1}^{T_i} RD_{i,t}^{(R)} - \sum_{t=1}^{T_i} FD_{i,t}}{T_i} \quad |i = 1 \dots N \tag{28}$$

where $RD_{i,t}^{(R)}$ denotes $RD_t^{(R)}$ for subject i and T_i denotes the number of time frames in the fMRI time series of subject i (after exclusion of first five volumes). Using the terminology of equation (25):

$$\overline{\Delta RD}_i^{(R)} = \frac{\sum_{t=1}^{T_i} \Delta RD_{i,t}^{(R)}}{T_i} \tag{29}$$

where, alternatively to $RD_{i,t}^{(R)}$, $\Delta RD_{i,t}^{(R)}$ denotes $\Delta RD_t^{(R)}$ of subject i.

Thus, in case of a GLM model for the connection between regions A and B, equation (27) extends to:

$$c_i^{(A,B)} = \alpha + \beta GRP_i + \gamma_1 AGE_i + \gamma_2 FIQ_i + \gamma_3 SEX_i + \gamma_4 FD_i + \\ + \gamma_5 \overline{\Delta RD}_i^{(A)} + \gamma_6 \overline{\Delta RD}_i^{(B)} + \gamma_7 \overline{\Delta RD}_i^{(A)} \overline{\Delta RD}_i^{(B)} + \epsilon_i \quad (30)$$

Henceforward, we refer to the model specified in equation (27) as a standard (STD) model and, to the terms $\gamma_5 \overline{\Delta RD}_i^{(A)} + \gamma_6 \overline{\Delta RD}_i^{(B)} + \gamma_7 \overline{\Delta RD}_i^{(A)} \overline{\Delta RD}_i^{(B)}$ as *regional displacement interaction* (RDI) and, to the model defined by equation (30) as an STD+RDI model.

Characterization of the RDI effect

To investigate the RDI interaction effect on connectivity strength we utilized the following models:

$$c_i^{(A,B)} = \alpha + \gamma_1 AGE_i + \gamma_2 FIQ_i + \gamma_3 SEX_i + \gamma_4 FD_i \\ + \gamma_5 \overline{\Delta RD}_i^{(A)} + \gamma_6 \overline{\Delta RD}_i^{(B)} + \gamma_7 \overline{\Delta RD}_i^{(A)} \overline{\Delta RD}_i^{(B)} + \epsilon_i \quad (31)$$

and

$$c_i^{(A,B)} = \alpha + \gamma_1 AGE_i + \gamma_2 FIQ_i + \gamma_3 SEX_i + \gamma_4 FD_i + \epsilon_i \quad (32)$$

which are alternative versions of models (30) and (27), respectively, with GRP variable excluded. Since models (31) and (32) are nested, we can compare the reduction in deviance to residuals utilizing an F-test under the null hypothesis that none of the additional RDI covariates in the STD+RDI model is related to the measured connectivity strength. The resulting statistical parameters for each connection were ordered into nine differential SPNs for each nuisance regression model, showing connections significantly related to RDI. Model (31) was also used to demonstrate RDI in case of a single, representative connection.

We furthermore fitted a model defined as:

$$C_j = \alpha + \gamma_1 AGE_j + \gamma_2 FIQ_j + \gamma_3 SEX_j + \\ + \gamma_4 FD_j + \gamma_5 \overline{\Delta RD}_k + \gamma_6 \overline{\Delta RD}_l + \beta \overline{\Delta RD}_k \overline{\Delta RD}_l + \epsilon_j \quad (33)$$

where $C_j = C_i^{(A,B)}$ so that $j = iM^2 + AM + B$ and $\overline{\Delta RD}_k = \overline{\Delta RD}_i^{(A)}$ so that $k = iM^2 + AM$ and $\overline{\Delta RD}_l = \overline{\Delta RD}_i^{(B)}$ so that $l = iM^2 + B$, or, in other words, the dependent and independent variables of model (31) are concatenated following the A and B ($A = 1 \ldots M, B = 1 \ldots M$) atlas regions. In contrast to the previously introduced models, here, we utilize one model for all connections of all subjects. The effect of interest is the RDI interaction term. This model was used to analyze the overall nature of the interaction term.

To avoid the disturbing effect of autistic differences when characterizing the interaction term, only the healthy control population was involved when applying models defined by Eqs. (31), (32) and (33).

Voxel-wise motion-related group comparison

Differences between low and high motion groups were investigated by two GLM models for every connection: STD (Eq. (27)) and STD+RDI (Eq. (30)) models were applied where GRP was a dummy variable that defined the motion-related groups as listed in Table 3. Results were ordered into 8*9*2 t-score SPNs, summarizing motion-related group differences (eight pairs of motion-related groups, nine first-level nuisance regression methods, and two second-level regression models [STD and STD+RDI]). Since, in these comparisons, the variable of interest (grouping factor) and the motion-related covariates (FD and the RDI covariates) are potentially related, we computed the variance inflation factor (VIF) [109] for each model. VIF values suggest that these modeling approaches are free from multicollinearity issues. (Maximal observed VIF values for the variable of interest are reported in Table 3.)

Autistic-control comparison

We tested the proposed RDI second-level interaction covariate set by comparisons of autistic and control groups defined by phenotypic information that was provided with the Autism Brain Imaging Dataset Exchange database. Results were arranged into 9*2 SPNs for nine nuisance regression methods and two second-level regression methods (STD and STD+RDI).

Computations and network visualization

Computations in this study, when not specified otherwise, were performed using R statistical programming language [110], using the packages ”glm” [111], ”fdrtool” [112, 113], ”HH” [114] and ”visreg” [115]. Differential SPNs were thresholded and visualized with the inhouse developed software BrainCON (www.minipetct.com/braincon) [92].

5 Results and Discussion

5.1 Development of software and establishment of pipeline

The moudular software system described in section 3. provides the opportunity of establishing fMRI-based brain connectivity analysis pipelines in a flexible manner and well-structured form.

BrainMOD was used for the construction of filtered regional time series, and also, for quality check of temporary results throughout the analysis. Developments regarding the role of BrainMOD were presented at [78, 91].

The region system applied for data-reduction was constructed using BrainLOC (previously published in [77, 85]). To produce comparable results, fParc was not applied in this study, however our extensional energy term (Eq. (11)) in the MRF model described by Ryali et al. in [57] seems to yield very promising results in other applications. With this modification, the general data-driven segmentation approach is adapted the requirements of fMRI-based graph theoretical brain connectivity analysis and might mean a significant step towards the solution of node-definition problem [26].

The parallelized procedures, mainly implemented in BrainNetTools, together with the high-performance computing capabilities[17] available in Debrecen, Hungary, allowed the fast and automatic analysis of the vast amount of data. We applied BrainNetTools also in several other studies [16–21].

All the network plots were visualized using BrainCON. The real-time direct visualization of the data played a very important role in drawing several of our conclusions. BrainCON was presented at interactive software exhibits at [79, 92] and besides being the main visualization tool, also played critical role in collaboration between co-authors in our studies [16, 19–21] and [18].

---

[17] https://www.niif.hu/szolgaltatasok/szuperszamitastechnika/niif_szuperszamitogep_szolgaltatas

5.2 The Spatial Predisposition of fMRI Motion Artifacts

As noted by Power et al. [41,44], the effect of motion appears to scale with the amplitude of the displacement over the whole brain: frames with greater amplitude displacements are associated with a greater change in BOLD signal. As a first step, we reproduced these results by observing a $\rho = 0.485$ ($p<10^{-6}$) correlation between frame-wise displacement FD and DVARS.

Our results also show that this effect is not spatially constant. Although as also reported in [40], RD time courses show high correlation in the entire brain of one subject, if the global effect is subtracted from the regional measures (FD from RD and DVRAS from RDVARS, respectively) the resulting residual measures $\Delta RD_i^{(R)}$ and $\Delta RDVARS_i^{(R)}$ (Eqs. (25) and (26)) still show a significant correlation of $\rho = 0.278$ ($p<10^{-4}$). In addition, as presented in Fig. 11, the correlation of these residual regional measures increases with the global motion-BOLD relationship throughout subjects.

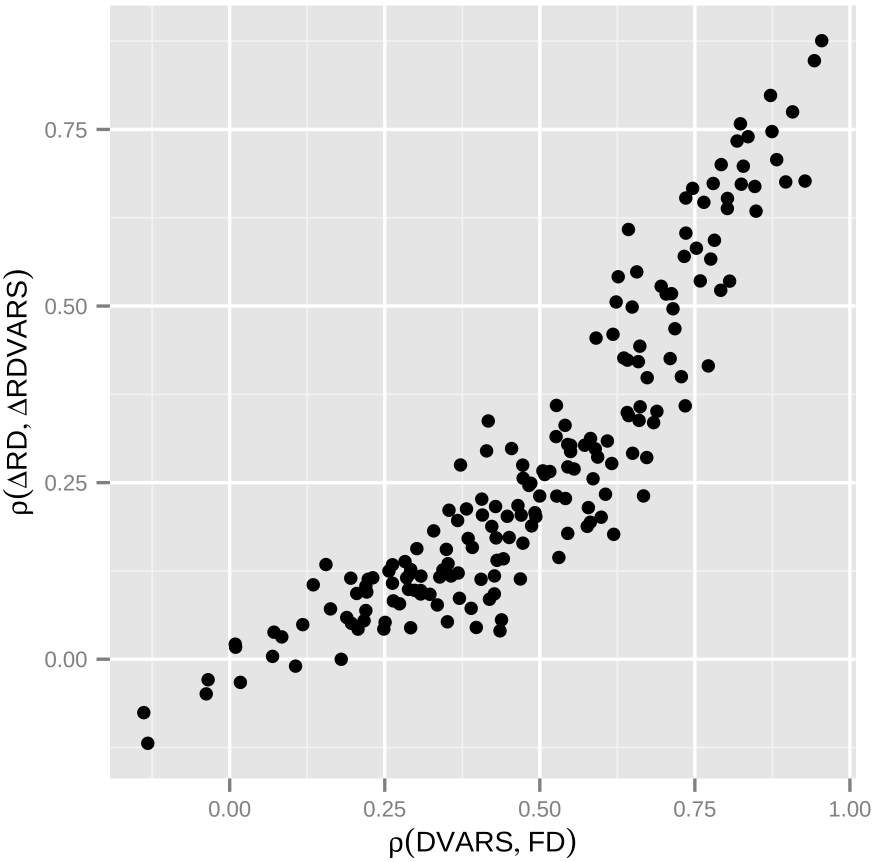

Figure 11. Regional motion-BOLD relationship scales with the global motion-BOLD relationship

Within-subject correlation of $\Delta RD_i^{(R)}$ and $\Delta RDVARS_i^{(R)}$ (horizontal axis) plotted against the correlation of FD and DVARS (vertical axis) for all brain regions and time frames of N=183 subjects. The regional effect of motion on BOLD seems to scale with the global relationship which is correlated ($\rho = 0.485$ (p<0.000001) with the mean FD.

In-scanner head motion consists not only of translations. Rotational components make the displacement diverse in distinct locations: it becomes greater when moving further from the center of rotations. A plausible explanation of the reported regional relationship is that this complex spatio-temporal pattern of displacement implicitly affects local BOLD signal changes.

These results can also yield a potential explanation of the phenomenon that motion tends to increase connectivity for locally adjacent nodes, but reduces connectivity between distant nodes [39, 41–43, 45]: neighboring regions having more similar RD will share more similar motion artifacts than regions being far from each other and this effect biases the distance dependence of connectivity strength.

However, we should point out that all the discussed voxel-wise and regional displacement measures are only "apparent displacements": their estimated values may have been affected by phenomena other than head motion, including physiological noise, magnetic field inhomogeneities, instrumental instabilities, as well as BOLD activity of neuronal origin. This effect should be more pronounced for regional displacements than for the frame-wise displacements. Furthermore, the computation of RD implicitly include integrating of motion effects within each fMRI volume. Rapid head movements occurring on time scale shorter than the fMRI repetition time TR may affect different slices within an fMRI volume differently [116]. Effects of such rapid movements cause slice-specific image distortions that cannot be accurately taken into account by the volume realignment-based procedure, but can still affect fMRI functional connectivity results. Averaging over all time frames and within time frames is a simplification in modeling the spatial predisposition of head motion. However, as suggested by the significant correlation between $\Delta RD_i^{(R)}$ and $\Delta RDVARS_i^{(R)}$, this simplification seems to be reasonable. Nevertheless, sub-TR frequency components of in-scanner motion deserve more attention and their voxel-wise effect should be investigated in more detail in future publications.

5.3 The Inter-regional Interaction Effect of Regional Displacements

The interaction of regional displacements affects measured connectivity strength

Evidences of a spatially non-constant motion artifact in brain connectivity analysis, like an increase in short-range and a decrease in long-range connectivity, or the special pattern of related changes in connectivity strength reported in [39, 41–43, 45], suggest that the reported local relationship between motion and BOLD signal changes should be considered when performing correction techniques. This is especially true for correlation-based functional connectivity analysis, where the similarity of two regional BOLD time courses can be increasingly affected by these small but systematic variations.

However, including voxel-wise motion parameters in nuisance signal regression does not seem to be efficient (as reported by [40,45] and also found in our preliminary analysis). Yan et al. [45] used voxel-wise displacement as a reference to evaluate the differential region-specific impact of motion on the BOLD signal. Although these authors presented significant correlations with a spatial pattern similar to that previously reported, it is still not clear whether those patterns can be explained only by locally differential BOLD answers to a global motion effect, or, alternatively, by a real local relationship with the spatio-temporal motion pattern.

To investigate this question, we defined RDI, a set of second-level regression covariates that models the interaction effect between the temporally averaged regional displacements of the regions involved in the connection. In regression analysis, an interaction effect is said to exist when the effect of the focal independent variable on the dependent variable differs depending on the value of a third variable [117], called the moderator variable. (Statistically, the choice of which of the two independent variables should be the moderator variable is unimportant.) The proposed RDI interaction term in the second-level GLM model defined by Eq. (33) was found to be significant

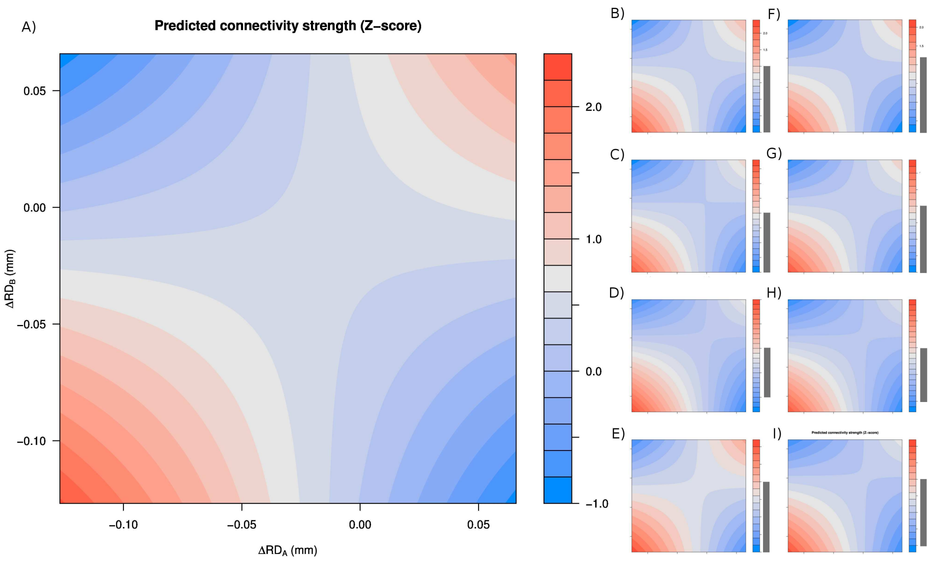

Figure 12. Filled contour plots visualizing the Regional Displacement Interaction (RDI) effect The predicted connectivity strength (color-coded) changes depending on the simultaneously varying values of $\overline{\Delta RD}_i^{(A)}$ and $\overline{\Delta RD}_i^{(B)}$, in case of no nuisance regression (A:NOREG) and all investigated first-level nuisance regression methods, i.e., NOREG+M6 (E), WMSCF (B), COMPCORR (C), GSREG (D), WMSCF+M6 (F), COMPCORR+M6 (G), GSREG+M6 (H), and SAT36 (I). Vertical and horizontal axes of plots B-I are the same as those of plot A. Gray bars next to the legends indicate the (-1,1) interval to ease interpretation of color-coded Z-score values.

($p<0.000001$) for all first-level nuisance regression methods), which means that the effect of the average RD of one region on the dependent variable (connectivity strength) changes when the average RD of the other region changes.

The effect is visualized in Fig. 12. by the filled contour plots. The predicted connectivity strength changes depending on the simultaneously varying values of $\overline{\Delta RD}_i^{(A)}$ and $\overline{\Delta RD}_i^{(B)}$, in case of all investigated first-level nuisance regression methods. These results imply that throughout the population, connectivity strength between two brain regions tends to increase if the average RD of the regions is similar (e.g. both are larger or smaller than the average FD) and tends to decrease otherwise.

This effect is demonstrated for a representative connection (occipital fusiform gyrus - prefrontal gyrus) in Fig. 13. While the presented partial residual plot reveals no significant relationship between connectivity strength and ΔRD_A, the $\Delta RD_A \Delta RD_B$ interaction effect is significant implying that the effect of ΔRD_A on connectivity strength differs depending on the value of ΔRD_B. This is demonstrated by dividing the data into four groups based on the value of ΔRD_B and visualizing the corresponding cross-sectional CCPR (component and component-plus-residual) plots, which reveal that in each group the relationship between ΔRD_A and partial residual connectivity strength is significant in all cases but the regression lines have different slopes. Thus, this latent relationship is not observable without accounting for the interaction of the regional displacement covariates.

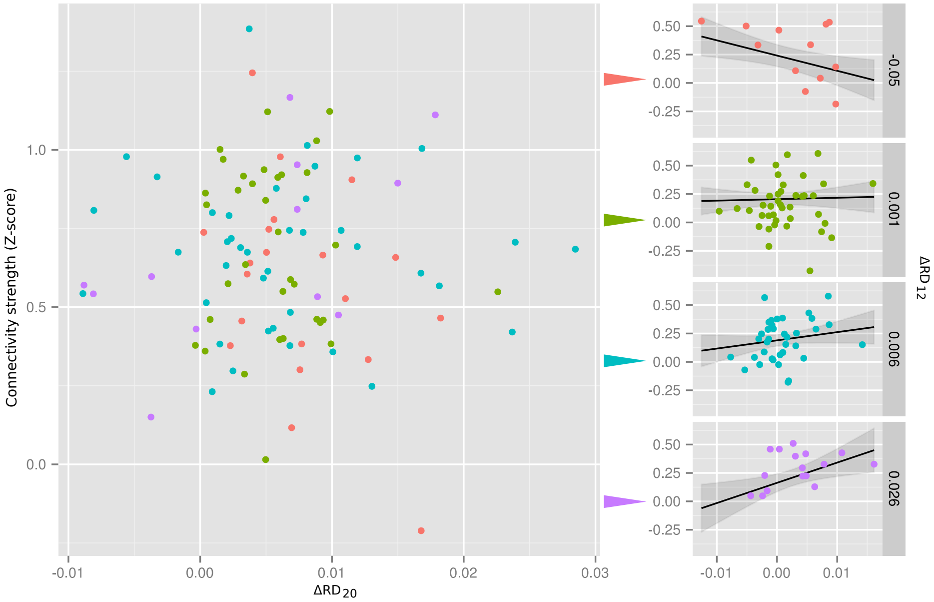

Figure 13. RDI effect in case of a demonstrative connection

Connectivity strength between the occipital fusiform gyrus (A=20) and the prefrontal gyrus (B=12). On the left, the partial residuals for ΔRD_A from the model defined by Eq. (31) (dependent variable: connectivity data of the healthy control population (N=105), without nuisance signal regression (NOREG)) are plotted against ΔRD_A. Although the model reveals no significant relationship (t=-1.46,p=0.15) between connectivity strength and ΔRD_A, the $\Delta RD_A \Delta RD_B$ interaction effect is significant (t=3.31, p=0.0013), implying that the effect of ΔRD_A on connectivity strength differs depending on the value of ΔRD_B. This is demonstrated by dividing the data into four groups based on the value of ΔRD_B (color-coded on the left plot) and visualizing the corresponding cross-sectional CCPR (component and component-plus-residual) plots (on the left). Mean value of ΔRD_B corresponding to the cross-section is indicated. Partial residuals are plotted with colored dots corresponding to the cross-section group. The corresponding regression line estimated from the full model fit and the corresponding 95% confidence interval is displayed in black and gray, respectively. The horizontal and vertical axes of the cross-sectional CCPR plots are the same as those of the partial residual plot on the left. Cross-sectional CCPR plots imply that in each group the relationship between ΔRD_A and partial residual connectivity strength is significant but the regression lines have different slopes, which makes this latent relationship not observable without accounting for the interaction of the regional displacement covariates.

To characterize how this phenomenon is related to the spatial patterns of measured functional connectivity and to what extent it is present in case of the applied first-level nuisance signal regression techniques, we performed a comparison of the STD (Eq. (31)) and STD+RDI (Eq. (32)) models. The model comparison was realized by F-tests between the models and resulted in the SPNs shown in Fig. 14. In this figure, connections are visualized, where the STD+RDI model explains significantly more variance than the STD model (the null hypothesis of the F-test can be rejected) with a false discovery rate of $q<0.05$. The proposed method, RDI proved to be the most efficient with nuisance signal regression methods NOREG, WMCSF, WMCSF+M6, GSREG, and COMPCOR+M6. The explanatory power added by RDI is most pronounced typically in case of middle- and long-range connections of the temporal poles.

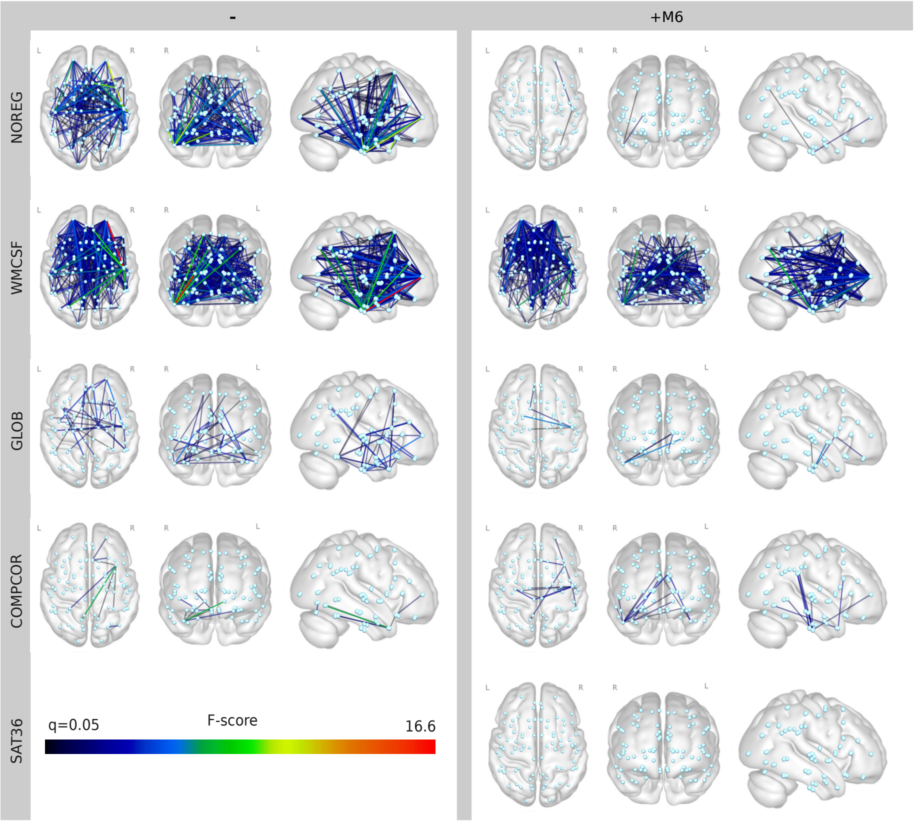

Figure 14. Network pattern of connections where utilizing RDI significantly improves second-level modeling

Statistical parametric networks presenting the model comparison performed by F-tests between the STD and STD+RDI models (Eq. (32) and (31)). Connections are only visualized, when the STD+RDI model explains significantly more variance than the STD model (the null hypothesis of the F-test can be rejected) with a false discovery rate of $q<0.05$. The proposed STD+RDI method proves to be most efficient with the nuisance signal regression methods NOREG, WMCSF, WMCSF+M6, GSREG, and COMPCOR+M6, and seems to demonstrate no significant improvement in case of SAT36, after correction for multiple comparison.

The interaction of regional displacements may bias functional connectivity group comparisons

The correlation coefficient of two regional BOLD time courses can be sensitive to the regional displacement time course (RD) of both regions. Even if the motion-related artifactual component is small, it still can significantly affect correlations, depending on the degree to which it is shared between the time courses.

This phenomenon becomes even more problematic on the population-level. Satterthwaite et al. [39] reported that between-subject differences in head motion are stable: subjects who tend to move on one occasion tend to move on another occasion. This means that analyses of functional connectivity needs to consider the possibility that *certain aspects of head motion behave as a trait.* Accordingly, even if the above-mentioned effect is otherwise small, it can disturb group comparisons and lead to erroneous conclusions, since it is of non-neural origin.

This assumption can be admitted easily by considering two patient cohorts where region A and B have similar RD within each subject of one group (e.g., due to relatively smaller rotations), and different RD in the subjects of the other (e.g., more prevalent rotations with a center to which A and B are located asymmetrically). The significant RDI interaction effect means that the corresponding correlation coefficient will be biased, and tends to be larger in the first group, even in the absence of a real functional difference. However, it is still not clear how different grouping conditions interfere with the tendency of motion patterns.

One can hypothesize that the spatio-temporal pattern of motion can be significantly different between groups that were defined by a factor in relation to motion. This could be the case in group comparisons in several physiological and pathological conditions co-occurring with hypo- or hyperkinetic signs.

5.4 The Proposed Correction Technique: Regional Displacement Interaction

As presented in the followings, our results show that the spatio-temporal pattern of head motion biases measured connectivity strength on the population level, and, practically speaking, *the proposed second-level covariates (RDI) can be utilized as a method to incorporate these individual regional differences of in-scanner head motion into the model, and thus, reduce artifactual variance in the data.*

Including RDI as a covariate in second-level regression efficiently reduces group differences caused by differences in voxel-wise motion

To demonstrate the reported confounding effect of voxel-wise motion on population-level analysis, we performed eight group comparisons (See Table 3.) where the groups to compare have different average voxel-wise displacement patterns.

Results are summarized in Table 4.

Table 4. Motion-related group differences

ρ_{WD}	0.89	0.90	0.91	0.92	0.93	0.94	0.95	0.96
NOREG	106 (1)	12	12	5	8	3	4	0
NOREG+RDI	63	3	6	3	3	2	0	0
WMCSF	139 (2)	5	26	9	5	11	17	1
WMCSF+RDI	84	2	15	8	1	4	2	0
GSREG	11	46	30	75 (1)	30	63	17	38
GSREG+RDI	11	29	33	58	29	40	12	33
COMPCOR	35	16	40	17	21	7	104 (2)	12
COMPCOR+RDI	8	8	26	11	12	7	46	10
NOREG+M6	121	5	20	3	3	2	9	0
NOREG+M6+RDI	64	1	13	3	1	1	1	0
WMCSF+M6	106	6	39	5	2	44	58	2
WMCSF+M6+RDI	37	4	25	7	1	26	4	1
GSREG+M6	20	32	31	108 (1)	23	52	16	29
GSREG+M6+RDI	19	15	29	94	19	53	20	22
COMPCOR+M6	59	5	39	66	25	5	62 (1)	13
COMPCOR+M6+RDI	17	4	37	41	9	6	30	12
SAT36	20	38	34	85	22	43	17	33
SAT36+RDI	21	15	39	69	20	44	13	34

Number of connections significantly ($p<0.01$) differing between groups. Voxel-wise displacement-related group comparisons corresponding to given ρ_{WD} are presented in columns. Rows correspond to the nine nuisance regression methods and their +RDI variants. Number of differences surviving the $q<0.05$ false discovery rate criterion (if any) is indicated in parentheses.

In Fig. 15, the number of significantly ($p<0.01$) differing connections is plotted against the group-defining mean FD threshold for each nuisance signal regression method. Results show that, for less extensive nuisance regression methods (NOREG, NOREG+M6, WMCSF, WMCSF+M6), when the voxel-wise displacement maps between groups are more different (lower between-group mean voxel-wise displacement map correlations), more group differences appear. These findings seem to confirm that group comparisons may be biased when groups show different tendencies in voxel-wise motion. Results, in conjunction with the results of the F-test based model comparisons Fig. 14., also show that *the inclusion of RDI covariates seems to decrease these artifactual group differences, especially by moderate nuisance regression methods.*

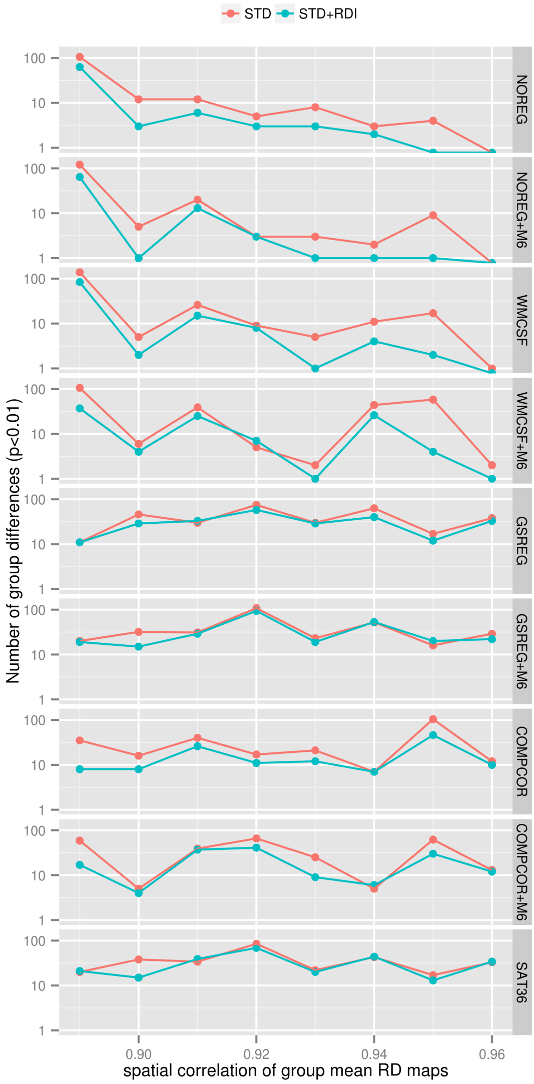

Figure 15. The effect of RDI on motion-related group differences

The number of significantly ($p<0.01$) differing connections is plotted against the spatial correlation coefficient of group-mean voxel-wise displacement maps for RD-based group-pairs for each nuisance signal regression method. The number of significant group differences is plotted on logarithmic axis.

The change in the corresponding connectivity pattern is visualized in Fig. 15. for the nuisance signal regression methods NOREG, COMPCOR, and GSREG, and for each motion-related group comparison defined by ρ_{WD}. Results with the STD and STD+RDI second-level regression models are presented in the upper and lower rows on each panel, respectively. Group differences with probability ($p>=0.01$) are not visualized.

As predicted by the F-test-based model comparisons (Fig. 14.), the reduction of false group differences caused by voxel-wise motion most markedly improved in the NOREG, WMCSF and COMPCOR methods. Regressing out six motion parameters did not seem to be highly efficient but may be beneficial when no other nuisance signal regression covariate is applied (NOREG+M6).

However, the small number of differences surviving the $q<0.05$ false discovery rate criterion implies that - when utilizing a proper second-level model - all the investigated methods are able to reduce motion-related group comparison artifacts to a decent extent. With the RDI correction, no FDR significant group differences remained in any of the comparison cases.

We note, that, in contrast to most prior studies, here, we performed more than a single pair of group comparisons, thus avoiding that results reflect only the random effects of the grouping condition.

Including RDI as a covariate in second-level regression preserves autism-related group differences

To test the efficiency of the proposed correction method, we performed group comparisons where both motion-related artifacts [30, 75] and real neuronal differences [16, 72, 118] were expected to be present. We compared the functional networks of autistic and control patients.

The correlation between the group-mean voxel-wise correlation map (ρ_{WD}) between the autistic and the normal control groups was found to be 0.98. It suggests that this grouping condition should

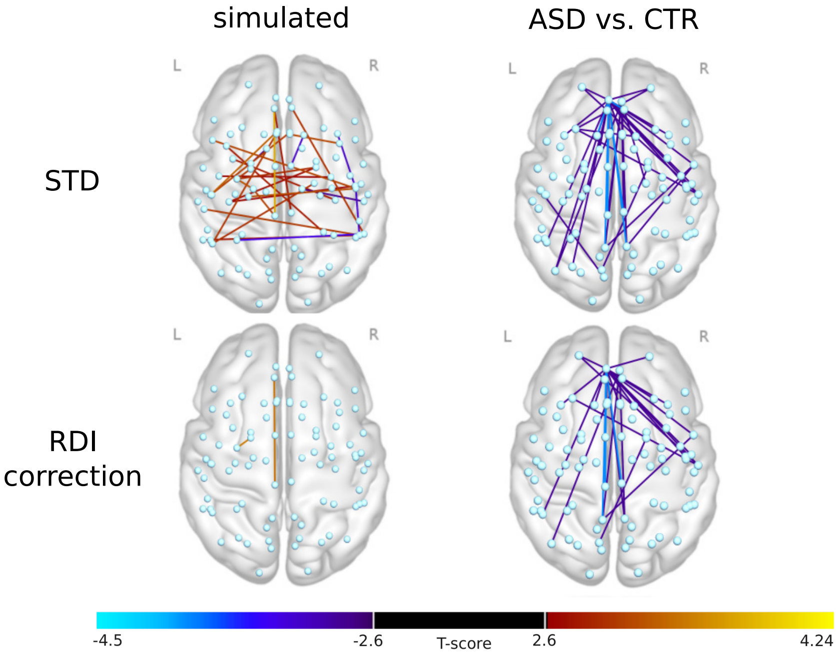

Figure 16. The effect of the proposed correction technique
Results of group comparisons between (left column) simulated groups with $\rho(DVARS, RD) = 0.89$ (extremely different voxel-wise motion patterns between groups) and (right column) the autism and control groups, with (bottom row) and without (top row) modeling RDI (FDR corrected statistical threshold).

be only slightly biased by the effect of regional displacement on the measured connectivity strength. Thus, as predicted by voxel-wise displacement pattern-related group comparisons, utilizing the RDI correction method should introduce only minor changes in the differential connectivity patterns.

Results are presented in Fig. 16. and Table 5.

More than 200 connectivity differences survived the q<0.05 false discovery rate criterion in NOREG and COMPCOR (both with and without RDI) and none survived in GSREG+RDI, GSREG+M6, GSREG+M6+RDI, SAT36 and SAT36+RDI. As predicted above, the inclusion of RDI introduces only slight changes in the pattern of autism-related group differences.

All the evaluated signal regression approaches revealed presumably autism-linked impairments of functional connectivity. Autism was mainly characterized by decreased synchronicity, i.e., underconnectivity. This finding is in line with the majority of intrinsic functional connectivity studies. The spatial predisposition, along with the 30 most significant differences, is presented in Fig. 16. and Table 5.

While including RDI significantly reduced (presumably artifactual) differences between voxel-wise displacement-related subject cohorts, differences in the autism-related comparison were more or less preserved. These results suggest that the proposed correction method, while effectively reducing motion artifacts in group comparisons, preserves the sensitivity to neural differences.

A critical interpretation of our autism-linked findings in this study is not directly possible. This mainly stems from the lack of ground truth information about the basic neuropathology of the disease. Furthermore, larger-scale, multi-centric comparisons would be optimal to test the reproducibility of any finding.

Table 5. Autism-related group differences (without nuisance signal regression of six motion parameters)

Connection	NOREG	+RDI	WMCSF	+RDI	GSREG	+RDI	COMPC	+RDI
L-CUN - L-STG	-3.73 ***	-3.52 ***	-2.79 *	-2.56	-2.67 *	-2.19	-5.03 ***	-4.57 ***
L-OCCFUS - R-TFUS	-3.64 ***	-3.98 ***	-3.88 **	-4.03 ***	-3.26 *	-3.17 *	-4.88 ***	-4.62 ***
L-FMEDC - R-PARCING	-4.30 ***	-4.11 ***	-4.16 **	-4.06 ***	-3.02 *	-3.09 *	-4.86 ***	-4.77 ***
L-FMEDC - R-CINGPOST	-4.54 ***	-4.23 ***	-3.94 **	-3.86 ***	-1.92	-1.94	-4.83 ***	-4.55 ***
R-MFG - R-PARHIPC	-3.14 ***	-3.63 ***	-4.54 ***	-4.67 ***	-3.70 **	-3.85 **	-3.55 ***	-3.47 ***
L-SMARGP - L-MTGANT	-3.38 ***	-3.54 ***	-2.66 *	-2.79 *	-2.48	-2.54	-4.65 ***	-4.49 ***
R-TFUS - R-TOFUS	-3.35 ***	-4.13 ***	-2.92 *	-3.48 ***	-1.57	-1.75	-4.43 ***	-4.59 ***
L-FMEDC - L-CINGPOST	-4.30 ***	-3.97 ***	-3.52 **	-3.40 ***	-1.83	-1.84	-4.19 ***	-3.95 ***
L-HIP - L-THAL	-0.28	-0.06	2.2	2.03	4.53 ***	4.21 **	-0.15	0.45
L-SFG - L-MTGANT	-3.71 ***	-3.97 ***	-2.84 *	-3.00 *	-3.00 *	-2.97 *	-4.49 ***	-4.30 ***
L-FMEDC - R-FRONT	-4.49 ***	-3.98 ***	-4.03 **	-3.61 ***	-2.78 *	-2.45	-4.00 ***	-3.63 ***
L-CUN - L-PLAN	-3.24 ***	-2.96 ***	-2.27	-2.01	-1.72	-1.18	-4.47 ***	-3.96 ***
L-STG - R-CUN	-3.19 ***	-2.97 ***	-2.47	-2.24	-2.82 *	-2.45	-4.46 ***	-4.02 ***
L-TEMP - L-THAL	0.28	0.48	2.03	2.16	4.45 ***	4.07 **	0.02	0.13
R-PARHIPC - R-HIP	0.99	0.52	2.33	2.17	4.44 ***	4.29 **	0.34	0.29
L-MTGANT - R-SFG	-3.33 ***	-3.50 ***	-2.82 *	-2.89 *	-1.85	-1.73	-4.44 ***	-4.25 ***
R-FMEDC - R-PRECUN	-4.43 ***	-4.35 ***	-3.12 *	-3.10 *	-0.89	-1.03	-3.55 ***	-3.67 ***
L-FMEDC - L-PRECUN	-4.02 ***	-3.83 ***	-3.54 **	-3.55 ***	-1.22	-1.35	-4.40 ***	-4.28 ***
L-FMEDC - L-SFG	-4.16 ***	-3.87 ***	-3.51 **	-3.39 ***	-2.21	-2.31	-4.38 ***	-4.17 ***
L-FMEDC - R-PRECUN	-4.17 ***	-3.99 ***	-3.65 **	-3.62 ***	-1.1	-1.22	-4.34 ***	-4.29 ***
L-INS - R-MTGTEMPOC	-3.12 ***	-3.10 ***	-1.88	-2.02	-2.34	-2.36	-2.36	-1.84
L-FMEDC - R-MTGANT	-4.33 ***	-3.95 ***	-2.76 *	-2.45	-1.69	-1.47	-3.26 ***	-3.20 ***
L-ANG - L-MTGANT	-3.76 ***	-3.91 ***	-3.48 **	-3.68 ***	-3.02 *	-3.14 *	-4.29 ***	-4.26 ***
L-PARHIPC - R-SFG	-2.79 ***	-2.63 ***	-2.81 *	-2.51	-0.67	-0.89	-4.26 ***	-3.87 ***
L-FMEDC - L-PARCING	-3.93 ***	-3.62 ***	-3.59 **	-3.45 ***	-2.74 *	-2.74 *	-4.23 ***	-4.05 ***
R-SFG - R-PARHIPC	-3.03 ***	-3.59 ***	-3.47 **	-3.66 ***	-1.14	-1.34	-4.23 ***	-4.13 ***
L-OCCFUS - L-TFUS	-2.66 ***	-2.67 ***	-3.20 *	-3.14 *	-2.16	-2.3	-4.23 ***	-4.18 ***
L-FMEDC - L-FRONT	-4.23 ***	-3.49 ***	-3.33 *	-2.73 *	-1.83	-1.43	-3.41 ***	-2.79 ***
L-TEMP - R-SFG	-2.90 ***	-2.99 ***	-2.56	-2.44	-0.79	-0.78	-4.21 ***	-3.88 ***
R-OCCFUS - R-TFUS	-3.74 ***	-4.21 ***	-3.15 *	-3.49 ***	-2.14	-2.3	-3.66 ***	-3.57 ***

The overall 30 most significant autism-related group differences in order of significance level. The first column lists the short names of the region pairs (See Table 7. for full names and other information). The corresponding T-value estimated from the STD and STD+RDI models are shown for all investigated nuisance signal regression methods. Significance level is implied by asterisks: * $p<0.01$, ** $p<0.001$, *** FDR $q<0.05$.

5.5 Relation to Other Correction Strategies

Contrasting the impact of head motion and nuisance signal regression strategies

The efficiency of nuisance signal regression techniques in the context of rs-fcMRI motion artifacts analysis has been intensively investigated in the last few years; however, a significant part of these studies did not apply second-level regression covariates [39–41, 43] in population-level analysis. Their overall conclusion was that global signal regression, high-parameter nuisance signal regression, scrubbing, and de-spiking are potentially beneficial. However, recent studies have questioned some of these conclusions. In the following, we summarize the latest findings in the literature in contrast to our results.

Effect of global signal regression

In our analysis, patterns of group differences become extremely different when regressing out the whole-brain signal from regional BOLD time courses (GSREG, GSREG+M6 and SAT36). Most of the above-mentioned studies, which did not utilize second-level correction, applied GSREG in their analysis pipeline. Recent studies using mean FD as a second-level regressor [45, 46] also concluded that GSREG mitigates the effects of motion-related differences among subjects, but warns that investigators must weigh up the pros and cons of GSREG when deciding whether to employ it in the context of testing specific hypotheses.

Our results show that, after the correction of group-wise differences in head movement in the autism-control comparison, over-connectivity and under-connectivity can simultaneously appear. However, global signal regression in the processing pipeline appears to bias results toward over-connected differential networks. In addition to under-connectivity, many authors suggested short-distance over-connectivity (in the frontal lobe or globally) as a possible finding in autism spectrum disorders [119]. This theory was then questioned on the grounds that head-movement could induce similar effects [30]. As reported in [120], correlation estimates obtained after GSREG are more susceptible to the presence of motion and exacerbate distance-dependent bias. Moreover, as reported in [75,76], correlation patterns and group differences may become distorted after GSREG (depending on, e.g., region size or the underlying true connectivity structure). According to Müller et al. [121], pre-processing strategies greatly affect the spatial patterns of autism-linked connectivity traits, although under-connectivity is the most prevalent across studies. It is, therefore, safe to conclude that GSREG not only introduces anti-correlations in the functional connectome [122], but can also confound case-control comparisons in autism.

Effect of including motion parameters

In the case of voxel-wise motion pattern-related group comparisons, inclusion of the six motion parameters in first-level nuisance signal regression showed no obvious improvement in motion-artifact reduction. However, the inclusion of these parameters had a pronounced effect in autism-related group comparisons, especially in NOREG, WMCSF and COMPCOR techniques: the number of significant group differences decreased. Whether this phenomenon is due to improved motion-artifact reduction in the special case of autistic group comparisons, or due to overfitting and the removal of real brain signal, remains a question. However, evidence that spatial realignment-based estimation of motion parameters may yield poor results in periods of small movements [34] point toward the conclusion that motion parameter estimates should be applied carefully. As a possible solution, we suggest utilizing thresholded motion estimates and avoiding the use of motion parameters in periods of relatively small movements.

Optimal choice of individual-level motion-correction technique

In some cases, it is not clear whether various high-parameter nuisance regression techniques eliminate group differences due to increased specificity or decreased sensitivity. Considering most significant autism-related group differences, minimal nuisance regression techniques (NOREG, NOREG+M6) show a high consensus with moderate (WMCSF, WMSCF+M6) and more complex (COMPCOR, COMPCOR+M6) methods. This points to the conclusion that when analyzing a sufficiently large sample and utilizing an appropriate second-level model, the choice of individual-level signal nuisance regression technique becomes less crucial. However, when analyzing small samples and also with individual analysis, the role of these techniques is unquestionably important.

5.6 The Role of Confounds Not Related to Subject Motion

This article focused on motion-related artifacts, which are only one, although a conspicuous source of confounding effects in functional MRI. In this context, the performance of NOREG and NOREG+M6 methods in motion-related comparisons deserves attention. One possible explanation is that, although artifacts of other sources are obviously present in the data, their individual spatio-temporal pattern is more constant and their population-level distribution is more similar among the investigated subpopulations compared to motion-related confounds. Thus, these artifacts may have only a moderate disturbing effect in large-sample group comparisons. However, by grouping conditions in relation to physiological conditions, like blood pressure and blood oxygenation (or artifacts of scanner-related sources in multi-center studies), non-motion originated artifacts can appreciably affect the results. Thus in such experimental designs, nuisance regression methods may have a more important role.

This is also suggested by the results of autism-related group comparisons, where pronounced differences were experienced among various nuisance signal regression techniques. A potential explanation for these deviations is that, although the proposed motion-correction technique successfully reduces motion-related erroneous group differences, artifacts of other physiological and scanner-related sources affect autism-related group comparisons and these phenomenon is handled differently by various signal regression techniques.

6 Conclusion

In this thesis, we demonstrated that small movements during scanning can cause different displacements in various locations of the brain, and, accordingly, motion-related BOLD signal changes also depend on location. We characterized the effect of this spatio-temporally complex BOLD artifact pattern on functional connectivity. We proposed RDI, a set of regression covariates for the population-level correction of motion artifacts arising from local head motion. As shown with comparisons of groups with differing average voxel-wise motion pattern, the proposed correction technique efficiently reduces artifacts caused by differences in voxel-wise motion patterns in population-based connectivity analysis; and meanwhile, as demonstrated by comparing autistic and control groups, preserves differences corresponding to neural origin.

Our findings suggest that, especially by moderate nuisance correction methods, the inclusion of RDI as second-level nuisance covariates is generally appropriate and may become increasingly necessary when the variable of interest is interrelated with altered subject kinetics.

A limitation of the proposed method is that it cannot be effectively applied in case of individual studies or small sample sizes. Nevertheless, one should note that, in situations where the variable of interest is correlated with motion, second-level regression-based, motion-correction approaches can be conservative, as they remove common variation among regressors. Furthermore, the proposed method is based only on a simplified measure of motion and does not handle rapid sub-TR displacements, which may play an important role in regional motion artifact interactions.

The question of what is the optimal individual-level signal regression technique for motion correction remains open, but, seems less crucial for large-sample, group-level studies using a proper second-level correction method.

This thesis focused on motion-related artifacts, which are only one, although a conspicuous source, of confounding effects in functional MRI. In-scanner head motion is relatively easy to measure, and thus, corresponding artifacts are actively investigated. However, as suggested by the observed differences among nuisance signal regression techniques, physiological and scanner-related artifacts may also have an essential impact on fc-MRI studies.

The work was based on intensive software development efforts to establish a proper research and development framework for brain connectivity analysis studies. It had a significant contribution in several other neuroimaging studies. The system also provides novelties in the filed of neuroimaging: the adaptation of data-driven segmentation technique to connectivity analysis, the parallelized procedures in BrainNetTools and the novel visualization techniques in BrainCON can be considered as appreciable steps in the evolution of computer methods in brain connectivity analysis.

Summary

In the present thesis, we analyzed in-scanner subject motion during fMRI measurements and its effect on motion artifacts in functional brain connectivity analysis.

We demonstrated that small in-scanner movements detected by image co-registration methods causes different displacement in different parts of the brain. Accordingly, motion artifacts in the measured signal have also a complex spatial predisposition. As a potential solution, we proposed RDI, a novel population-level Generalized Linear Model-based motion artifact correction technique. The RDI technique is based on an interaction term incorporated into the population-based statistical analysis, which models the difference in the displacement of regions participating in a connection. Our results show that the proposed technique effectively reduces spurious group differences originating from regional motion differences.

According to our aims, we investigated an important issue recently brought up in the scientific literature stating that in certain pathological conditions, for instance in Autism Spectrum Disorders (ASD), in-scanner locomotion shows a significant alteration compared to Healthy Normal Control (HNC) subjects, and therefore, brain connectivity findings in ASD might have spurious artifactual sources, besides neural correlates. Our analysis on a large sample did not confirm this assumption. Accordingly, we have found that the proposed correction technique causes only minor changes in the differential connectivity pattern. Nevertheless, we demonstrated the existence of the phenomenon. Therefore, this effect still needs to be investigated in patient populations with other pathological conditions that might be related to altered kinetics.

Due to the disagreement about the optimal first-level nuisance signal regression methods, we performed the analysis with multiple techniques. Our results confirmed that first-level nuisance signal regression methods might have a complex unpredictable effect on second-level analysis results.

The research was based on intensive software development efforts, which resulted in a modular brain network analysis software framework (contribution of the candidate can be seen in Table 6.). To solve the issue of functional network node definition, a state-of-art Markov Random Field-based segmentation method was implemented. The standard approach was extended with a novel energy constraint regulating the volume of the regions and is therefore well-suited for brain connectivity analysis. To support interdisciplinary collaborations, we developed several novel brain network visualization techniques. The developed software system, besides aiding clinical research collaborations, also facilitates further methodological research and development in neuroimaging and brain connectivity analysis.

Table 6. Contribution of the candidate

TASK	section	effort	implement.	lines	publ.	user
M3I	3.2	10%	C++,Qt	50000		
BRAINLOC	3.5	100%	M3I	8000	[77,85]	DBLIS KEMP
FPARC	3.6	70%	M3I	1200		KEMP
BRAINMOD	3.7	90%	M3I	20000	[78,91]	DBLIS, KEMP, DDO
BRAINNETT.	3.8	50%	M3I	5000	[16–21]	DBLIS, KEMP, KEN
BRAINCON	3.9	90%	M3I	4000	[16, 18–21,79,92]	DBLIS, KEMP, KEN
RDI	4.5	100%	M3I, R	600	[17,123]	

Contribution of the candidate to the software components introduced in this thesis (with section number). The degree of effort (effort) is estimated, lines of code written (lines) is based on code statistics and revision control system (monotone) logs. The last row (user) lists institutes where the software is actively used.
KEMP: Kempenhaeghe Expertise Centre for Epileptology, Neurocognition and Sleep Medicine, Heeze, The Netherlands;
DBLIS: Department of Biomedical Laboratory and Imaging Science, University of Debrecen;
KEN: Department of Neurology, Kenézy Hospital Ltd.,
DDO: Department of Diagnostics and Oncoradiology, University of Kaposvár

Összefoglaló (Summary in Hungarian)

A jelen PhD disszertációban bemutatott munka során elemeztük a vizsgálati alanyok fMRI mérések alatti mozgása és a funkcionális agyi hálózatanalízis során jelentkező mozgási műtermékek közötti kapcsolatot.

Eredményeink szerint a vizsgálat alatti kis mértékű, képillesztéssel detektált elmozdulások eltérő mértékben érintik az agy egyes területeit, és ennek következtében a mért jelben keletkező mozgási műtermékek helyfüggőek. Ezen jelenségnek a populációs szintű funkcionális hálózatanalízist érintő hatásainak csökkentésére egy új Általánosított Lineáris Modell alapú korrekciós módszert, a Regionális Elmozdulás Interakció (Regional Displacement Interaction, RDI) technikát javasoltuk. Az RDI egy, a populációs statisztikai modellezés során használható interakciós magyarázó változó halmaz, mely modellezi a kapcsolatban lévő agyi régiópárok elmozdulásbeli eltéréseit, és eredményeink szerint hatékonyan csökkenti a térbeli mozgásmintázat szisztematikus eltéréseiből fakadó fals pozitív csoportkülönbségeket.

Célkitűzésünknek megfelelően megvizsgáltuk azon szakirodalmi felvetést, mely szerint egyes patológiás állapotokban, így pl. az autizmus spektrum zavarban (ASD) szenvedő páciensek esetén a felvétel alatti mozgási mintázat szisztematikus módon eltér az egészséges normál kontrol (HNC) alanyokhoz viszonyítva, és ennek következményeként az észlelt hálózati eltérések a neurális okok mellett részben műtermékekből fakadhatnak. Nagy esetszámon alapuló vizsgálataink alapján ASD esetén alaptalanak mutatkozott a felvetés. Ennek megfelelően azt tapasztaltuk, hogy az ajánlott korrekciós módszer csupán minimális mértékben változtatja meg az ASD és a HNC alanyok funkcionális agyi hálózati összevetésének kimenetelét. A műtermék individuális megjelenését azonban demonstráltuk, így a probléma egyéb pácienspopulációk esetében továbbra is vizsgálandónak tekinthető.

A szakirodalmi cikkek módszertani heterogenitására való tekintettel vizsgálatainkat több idősor szintű műtermék regressziós mo-

dell alkalmazása mellett is elvégeztük. Eredményeink megerősítették azon irodalmi adatokat, melyek szerint ezen első-szintű technikák alkalmazása több esetben nem jósolható módon befolyásolja a hálózatanalízis kimenetét.

Az analízist egy intenzív szoftverfejlesztési folyamat tette lehetővé, melynek során kifejlesztésre került egy moduláris agyi hálózatanalízis keretrendszer (a jelölt hozzájárulásának mértéke a 6. táblázatban látható). A funkcionális agyi hálózatanalízis régiókijelölési problémájának megoldására implementáltunk egy korszerű, Markov Véletlen Mező alapú szegmentációs eljárást, mely az általunk javasolt volumenmegszorítás alkalmazásával jól illeszkedik a hálózatanalízis követelményeihez. Az interdiszciplináris kollaborációk segítése érdekében több agyi hálózatvizualizációs technika is bevezetésre és implementálásra került. A kidolgozott szoftverrendszer a klinikai kutatások aktív támogatása mellett elősegíti a további módszertani kutatás-fejlesztést az idegtudományi képalkotás és így az agyi hálózatanalízis területén.

Acknowledgements

I am grateful to my supervisor ***Miklós Emri*** for the encouragement and guidance.

I am thankful for the Department of Nuclear Medicine and the Doctoral School of Informatics, University of Debrecen for providing the opportunity to conduct this interdisciplinary research and write the thesis.

I am also thankful for *Ervin Berényi* and *András Jakab* from the Department of Biomedical Laboratory and Imaging Science, University of Debrecen, for *Béla Clemens* from the Department of Neurology, Kenézy Hospital Ltd. and for *Pauly Ossenblok* form the Kempenhaeghe Expertise Centre for Epileptology, Neurocognition and Sleep Medicine, Heeze, The Netherlands for their collaboration, clinical support and participation in software testing.

I was honored to work with my colleagues at the Department of Nuclear Medicine and I am especially thankful for *László Balkay*, *Sándor Atilla Kis*, *Gábor Opposits*, *László Pohubi* and *Imre Lajtos* for their support.

This thesis could not have been written without the manifold support from my family and friends. Special thanks go to my English language editor: my Father.

Some tasks described in this thesis were supported by the ENIAC CSI project (No.120209), the European Union, the European Social Fund and the State of Hungary through grants ”National Excellence Program” (TÁMOP-4.2.4.A/2-11/1-2012-00001), ”National Brain Research Program” (”Charting the normal and pathological macro-scale brain connectome by in-vivo neuroimaging”, KTIA_13 AP-A:II/3), ”Basic and applied research to assist the development of speech for the deaf” (TÁMOP-4.2.2.C-11/1/KONV), ”Supercomputer, the national virtual lab” (TÁMOP-4.2.2.C-11/1/KONV-2012-0010). The funders had no role in study design, data collection or software development.

References

1. Aristotle (Met. 10f-1045a) Methaphysica.
2. Munakata Y, Stedron JM (2001) Neural network models of cognitive development. Handbook of developmental cognitive neuroscience : 159.
3. Lehn JM (2002) Toward self-organization and complex matter. Science 295: 2400–2403.
4. Milgram S (1967) The small world problem. Psychology today 2: 60–67.
5. Watts DJ, Strogatz SH (1998) Collective dynamics of 'small-world'networks. nature 393: 440–442.
6. Barabási AL, Albert R (1999) Emergence of scaling in random networks. science 286: 509–512.
7. Boccaletti S, Latora V, Moreno Y, Chavez M, Hwang DU (2006) Complex networks: Structure and dynamics. Physics reports 424: 175–308.
8. Ebel H, Mielsch LI, Bornholdt S (2002) Scale-free topology of e-mail networks. Physical review E 66: 035103.
9. Kim H, Kim I, Lee Y, Kahng B (2002) Scale-free network in stock markets. Journal-Korean Physical Society 40: 1105–1108.
10. Cohen R, Erez K, Ben-Avraham D, Havlin S (2001) Breakdown of the internet under intentional attack. Physical review letters 86: 3682.
11. Albert R (2005) Scale-free networks in cell biology. Journal of cell science 118: 4947–4957.

12. He Y, Evans A (2010) Graph theoretical modeling of brain connectivity. Current opinion in neurology 23: 341–350.

13. Leavitt VM, Wylie G, Genova HM, Chiaravalloti ND, DeLuca J (2012) Altered effective connectivity during performance of an information processing speed task in multiple sclerosis. Multiple Sclerosis Journal 18: 409–417.

14. Tian L, Meng C, Yan H, Zhao Q, Liu Q, et al. (2011) Convergent evidence from multimodal imaging reveals amygdala abnormalities in schizophrenic patients and their first-degree relatives. PloS one 6: e28794.

15. Lewis JD, Theilmann RJ, Fonov V, Bellec P, Lincoln A, et al. (2013) Callosal fiber length and interhemispheric connectivity in adults with autism: brain overgrowth and underconnectivity. Human brain mapping 34: 1685–1695.

16. Jakab A, Emri M, Spisak T, Szeman-Nagy A, Beres M, et al. (2013) Autistic traits in neurotypical adults: correlates of graph theoretical functional network topology and white matter anisotropy patterns. PloS one 8: e60982.

17. Spisák T, Jakab A, Kis SA, Opposits G, Aranyi C, et al. (2014) Voxel-wise motion artifacts in population-level whole-brain connectivity analysis of resting-state fmri. PloS one 9: e104947.

18. Clemens B, Puskás S, Bessenyei M, Emri M, Spisák T, et al. (2011) Eeg functional connectivity of the intrahemispheric cortico-cortical network of idiopathic generalized epilepsy. Epilepsy research 96: 11–23.

19. Clemens B, Puskás S, Besenyei M, Spisák T, Opposits G, et al. (2013) Neurophysiology of juvenile myoclonic epilepsy: Eeg-based network and graph analysis of the interictal and immediate preictal states. Epilepsy research 106: 357–369.

20. Clemens B, Puskás S, Besenyei M, Spisák T, Emri M, et al. (2013) Remission of benign epilepsy with rolandic spikes: An eeg-based connectivity study at the onset of the disease and at remission. Epilepsy research 106: 128–135.

21. Piros P, Puskas S, Emri M, Opposits G, Spisak T, et al. (2014) Uppermost synchronized generators of spike–wave activity are localized in limbic cortical areas in late-onset absence status epilepticus. Seizure 23: 213–221.

22. de Haan W, van der Flier WM, Wang H, Van Mieghem PF, Scheltens P, et al. (2012) Disruption of functional brain networks in alzheimer's disease: what can we learn from graph spectral analysis of resting-state magnetoencephalography? Brain connectivity 2: 45–55.

23. Wang K, Liang M, Wang L, Tian L, Zhang X, et al. (2007) Altered functional connectivity in early alzheimer's disease: A resting-state fmri study. Human brain mapping 28: 967–978.

24. Tessitore A, Esposito F, Vitale C, Santangelo G, Amboni M, et al. (2012) Default-mode network connectivity in cognitively unimpaired patients with parkinson disease. Neurology 79: 2226–2232.

25. Bullmore E, Sporns O (2009) Complex brain networks: graph theoretical analysis of structural and functional systems. Nature Reviews Neuroscience 10: 186–198.

26. Smith SM (2012) The future of fmri connectivity. Neuroimage 62: 1257–1266.

27. Horwitz B (2003) The elusive concept of brain connectivity. Neuroimage 19: 466–470.

28. van den Heuvel MP, Stam CJ, Boersma M, Pol HH (2008) Small-world and scale-free organization of voxel-based

resting-state functional connectivity in the human brain. Neuroimage 43: 528–539.

29. Behrens T, Johansen-Berg H, Woolrich M, Smith S, Wheeler-Kingshott C, et al. (2003) Non-invasive mapping of connections between human thalamus and cortex using diffusion imaging. Nature neuroscience 6: 750–757.
30. Deen B, Pelphrey K (2012) Perspective: brain scans need a rethink. Nature 491: S20–S20.
31. Friston KJ, Williams S, Howard R, Frackowiak RS, Turner R (1996) Movement-related effects in fmri time-series. Magnetic resonance in medicine 35: 346–355.
32. Kim B, Boes JL, Bland PH, Chenevert TL, Meyer CR (1999) Motion correction in fmri via registration of individual slices into an anatomical volume. Magnetic Resonance in Medicine 41: 964–972.
33. Glover GH, Li TQ, Ress D (2000) Image-based method for retrospective correction of physiological motion effects in fmri: Retroicor. Magnetic Resonance in Medicine 44: 162–167.
34. Freire L, Mangin JF (2001) Motion correction algorithms may create spurious brain activations in the absence of subject motion. NeuroImage 14: 709–722.
35. Jenkinson M, Bannister P, Brady M, Smith S (2002) Improved optimization for the robust and accurate linear registration and motion correction of brain images. Neuroimage 17: 825–841.
36. Behzadi Y, Restom K, Liau J, Liu TT (2007) A component based noise correction method (compcor) for bold and perfusion based fmri. Neuroimage 37: 90–101.

37. Lemieux L, Salek-Haddadi A, Lund TE, Laufs H, Carmichael D (2007) Modelling large motion events in fmri studies of patients with epilepsy. Magnetic resonance imaging 25: 894–901.

38. Jo HJ, Saad ZS, Simmons WK, Milbury LA, Cox RW (2010) Mapping sources of correlation in resting state fmri, with artifact detection and removal. Neuroimage 52: 571–582.

39. Satterthwaite TD, Wolf DH, Loughead J, Ruparel K, Elliott MA, et al. (2012) Impact of in-scanner head motion on multiple measures of functional connectivity: relevance for studies of neurodevelopment in youth. Neuroimage 60: 623–632.

40. Satterthwaite TD, Elliott MA, Gerraty RT, Ruparel K, Loughead J, et al. (2013) An improved framework for confound regression and filtering for control of motion artifact in the preprocessing of resting-state functional connectivity data. Neuroimage 64: 240–256.

41. Power JD, Barnes KA, Snyder AZ, Schlaggar BL, Petersen SE (2012) Spurious but systematic correlations in functional connectivity mri networks arise from subject motion. Neuroimage 59: 2142–2154.

42. Fair DA, Nigg JT, Iyer S, Bathula D, Mills KL, et al. (2012) Distinct neural signatures detected for adhd subtypes after controlling for micro-movements in resting state functional connectivity mri data. Frontiers in systems neuroscience 6.

43. Van Dijk KR, Sabuncu MR, Buckner RL (2012) The influence of head motion on intrinsic functional connectivity mri. Neuroimage 59: 431–438.

44. Power JD, Barnes KA, Snyder AZ, Schlaggar BL, Petersen SE Steps toward optimizing motion artifact removal in functional connectivity mri; a reply to carp. Neuroimage 76: 439–441.

45. Yan CG, Cheung B, Kelly C, Colcombe S, Craddock RC, et al. (2013) A comprehensive assessment of regional variation in the impact of head micromovements on functional connectomics. Neuroimage 76: 183–201.
46. Yan CG, Craddock RC, He Y, Milham MP (2013) Addressing head motion dependencies for small-world topologies in functional connectomics. Frontiers in human neuroscience 7: 910.
47. Westbrook C, Roth CK (2011) MRI in Practice. John Wiley & Sons.
48. Pakkenberg B, Gundersen HJ (1997) Neocortical neuron number in humans: effect of sex and age. The Journal of comparative neurology : 312–20.
49. Buxton RB (2009) Introduction to functional magnetic resonance imaging: principles and techniques. Cambridge university press.
50. McCulloch WS, Pitts W (1943) A logical calculus of the ideas immanent in nervous activity. The bulletin of mathematical biophysics 5: 115–133.
51. Attwell D, Laughlin SB (2001) An energy budget for signaling in the grey matter of the brain. Journal of Cerebral Blood Flow & Metabolism 21: 1133–1145.
52. Iadecola C (2004) Neurovascular regulation in the normal brain and in alzheimer's disease. Nature Reviews Neuroscience 5: 347–360.
53. Pauling L, Coryell CD (1936) The magnetic properties and structure of hemoglobin, oxyhemoglobin and carbonmonoxyhemoglobin. Proceedings of the National Academy of Sciences of the United States of America 22: 210.

54. Weisskoff RM, Kiihne S (1992) Mri susceptometry: Image-based measurement of absolute susceptibility of mr contrast agents and human blood. Magnetic Resonance in Medicine 24: 375–383.

55. Niblack W (1985) An introduction to digital image processing. Strandberg Publishing Company.

56. Fazekas A, Kormos J (2004) Digitális képfeldolgozás matematikai alapjai. mobiDIÁK, Debreceni Egyetem, Informatikai Intézet.

57. Ryali S, Chen T, Supekar K, Menon V (2013) A parcellation scheme based on von mises-fisher distributions and markov random fields for segmenting brain regions using resting-state fmri. Neuroimage 65: 83–96.

58. Smith SM (2002) Fast robust automated brain extraction. Human brain mapping 17: 143–155.

59. Zhang Y, Brady M, Smith S (2001) Segmentation of brain mr images through a hidden markov random field model and the expectation-maximization algorithm. Medical Imaging, IEEE Transactions on 20: 45–57.

60. Woods RP, Grafton ST, Watson JD, Sicotte NL, Mazziotta JC (1998) Automated image registration: Ii. intersubject validation of linear and nonlinear models. Journal of computer assisted tomography 22: 153–165.

61. Dimou S, Battisti R, Hermens D, Lagopoulos J (2013) A systematic review of functional magnetic resonance imaging and diffusion tensor imaging modalities used in presurgical planning of brain tumour resection. Neurosurgical review 36: 205–214.

62. Logothetis NK (2003) The underpinnings of the bold functional magnetic resonance imaging signal. The Journal of Neuroscience 23: 3963–3971.

63. Biswal B, Zerrin Yetkin F, Haughton VM, Hyde JS (1995) Functional connectivity in the motor cortex of resting human brain using echo-planar mri. Magnetic resonance in medicine 34: 537–541.

64. Van Den Heuvel MP, Pol HEH (2010) Exploring the brain network: a review on resting-state fmri functional connectivity. European Neuropsychopharmacology 20: 519–534.

65. Lu H, Zuo Y, Gu H, Waltz JA, Zhan W, et al. (2007) Synchronized delta oscillations correlate with the resting-state functional mri signal. Proceedings of the National Academy of Sciences 104: 18265–18269.

66. Golumbic MC (2004) Algorithmic graph theory and perfect graphs, volume 57. Elsevier.

67. Van Essen DC (2002) Windows on the brain: the emerging role of atlases and databases in neuroscience. Current opinion in neurobiology 12: 574–579.

68. Blumensath T, Jbabdi S, Glasser MF, Van Essen DC, Ugurbil K, et al. (2013) Spatially constrained hierarchical parcellation of the brain with resting-state fmri. Neuroimage 76: 313–324.

69. Smith SM, Miller KL, Salimi-Khorshidi G, Webster M, Beckmann CF, et al. (2011) Network modelling methods for fmri. Neuroimage 54: 875–891.

70. Friston KJ, Holmes AP, Worsley KJ, Poline JP, Frith CD, et al. (1994) Statistical parametric maps in functional imaging: a general linear approach. Human brain mapping 2: 189–210.

71. Fox MD, Zhang D, Snyder AZ, Raichle ME (2009) The global signal and observed anticorrelated resting state brain networks. Journal of neurophysiology 101: 3270–3283.

72. Di Martino A, Yan C, Li Q, Denio E, Castellanos F, et al. (2013) The autism brain imaging data exchange: towards a large-scale evaluation of the intrinsic brain architecture in autism. Molecular psychiatry 19: 659–667.

73. Cordes D, Haughton VM, Arfanakis K, Carew JD, Turski PA, et al. (2001) Frequencies contributing to functional connectivity in the cerebral cortex in “resting-state” data. American Journal of Neuroradiology 22: 1326–1333.

74. Van Someren E, et al. (2011) Spectral characteristics of resting state networks. Slow Brain Oscillations of Sleep, Resting State and Vigilance 193: 259.

75. Gotts SJ, Saad ZS, Jo HJ, Wallace GL, Cox RW, et al. The perils of global signal regression for group comparisons: a case study of autism spectrum disorders. Frontiers in human neuroscience 7: 356.

76. Saad ZS, Gotts SJ, Murphy K, Chen G, Jo HJ, et al. (2012) Trouble at rest: how correlation patterns and group differences become distorted after global signal regression. Brain connectivity 2: 25–32.

77. Spisák T, Koselák M, Opposits G, Kis SA, Trón L, et al. (2011) Region management toolkit for atlas-space image processing. Magn Reson Mat Phys Biol Med 24: 543.

78. Spisák T, Kis S, Opposits G, Lajtos I, Balkay L, et al. (2012) Brainmod:4-dimensional multimodal medical image analysis software. Magn Reson Mat Phys Biol Med 25: 619.

79. Spisák T, Kis S, Opposits G, Lajtos I, Balkay L, et al. (2012) Braincon: Software tool for graph theory based multimodal brain connectivity analysis and visualization. Magn Reson Mat Phys Biol Med 25: 616.

80. Smith SM, Jenkinson M, Woolrich MW, Beckmann CF, Behrens TE, et al. (2004) Advances in functional and structural mr image analysis and implementation as fsl. Neuroimage 23: S208–S219.

81. Woolrich MW, Jbabdi S, Patenaude B, Chappell M, Makni S, et al. (2009) Bayesian analysis of neuroimaging data in fsl. Neuroimage 45: S173–S186.

82. Neelin P (1998) The minc file format: from bytes to brains. NeuroImage 7: P–0786.

83. Damasio H (1995) Human brain anatomy in computerized images. Oxford university press.

84. Hammers A, Allom R, Koepp MJ, Free SL, Myers R, et al. (2003) Three-dimensional maximum probability atlas of the human brain, with particular reference to the temporal lobe. Human brain mapping 19: 224–247.

85. Spisák T, Koselák M, Opposits G, Kis SA, Trón L, et al. (2011) Digital brain atlas assisted localization software for individual and population analysis of spect and pet data. Eur J Nucl Med Mol Imaging 38: 258.

86. Banerjee A, Dhillon IS, Ghosh J, Sra S (2005) Clustering on the unit hypersphere using von mises-fisher distributions. In: Journal of Machine Learning Research. pp. 1345–1382.

87. Geman S, Geman D (1984) Stochastic relaxation, gibbs distributions, and the bayesian restoration of images. Pattern

Analysis and Machine Intelligence, IEEE Transactions on : 721–741.

88. Bishop CM, et al. (2006) Pattern recognition and machine learning, volume 4. springer New York.
89. Boykov Y, Veksler O, Zabih R (2001) Fast approximate energy minimization via graph cuts. Pattern Analysis and Machine Intelligence, IEEE Transactions on 23: 1222–1239.
90. Percival DB, Walden AT (2006) Wavelet methods for time series analysis, volume 4. Cambridge University Press.
91. Spisák T, Opposits G, Kis S, Lajtos I, Krizsán A, et al. (2013) Brainmod: multimodal medical image analysis software. In: Electronic presentation online system: ECR Congress 2013 ECR2013: C2568.
92. Spisák T, Opposits G, Kis SA, Clemens B, Emri M (2012) Braincon: Software tool for graph theory based multimodal brain connectivity analysis and visualization. Magn Reson Mat Phys Biol Med 25: 616.
93. Rubinov M, Sporns O (2010) Complex network measures of brain connectivity: uses and interpretations. Neuroimage 52: 1059–1069.
94. Latora V, Marchiori M (2001) Efficient behavior of small-world networks. Physical review letters 87: 198701.
95. Bassett DS, Bullmore E (2006) Small-world brain networks. The neuroscientist 12: 512–523.
96. Dijkstra EW (1959) A note on two problems in connexion with graphs. Numerische mathematik 1: 269–271.
97. Floyd RW (1962) Algorithm 97: shortest path. Communications of the ACM 5: 345.

98. Bullmore E, Sporns O (2012) The economy of brain network organization. Nature Reviews Neuroscience 13: 336–349.

99. Schindler KA, Bialonski S, Horstmann MT, Elger CE, Lehnertz K (2008) Evolving functional network properties and synchronizability during human epileptic seizures. Chaos: An Interdisciplinary Journal of Nonlinear Science 18: 033119.

100. Ginestet CE, Nichols TE, Bullmore ET, Simmons A (2011) Brain network analysis: separating cost from topology using cost-integration. PloS one 6: e21570.

101. Imperati D, Colcombe S, Kelly C, Di Martino A, Zhou J, et al. (2011) Differential development of human brain white matter tracts. PloS one 6: e23437.

102. Koyama MS, Di Martino A, Zuo XN, Kelly C, Mennes M, et al. (2011) Resting-state functional connectivity indexes reading competence in children and adults. The Journal of Neuroscience 31: 8617–8624.

103. Jenkinson M, Beckmann CF, Behrens TE, Woolrich MW, Smith SM (2012) Fsl. NeuroImage 62: 782–790.

104. Jenkinson M, Smith S (2001) A global optimisation method for robust affine registration of brain images. Medical image analysis 5: 143–156.

105. Desikan RS, Ségonne F, Fischl B, Quinn BT, Dickerson BC, et al. (2006) An automated labeling system for subdividing the human cerebral cortex on mri scans into gyral based regions of interest. Neuroimage 31: 968–980.

106. Smyser CD, Inder TE, Shimony JS, Hill JE, Degnan AJ, et al. (2010) Longitudinal analysis of neural network development in preterm infants. Cerebral Cortex 20: 2852–2862.

107. Dobson AJ (2010) An introduction to generalized linear models. CRC press.

108. Ginestet CE, Simmons A (2011) Statistical parametric network analysis of functional connectivity dynamics during a working memory task. Neuroimage 55: 688–704.

109. Stine RA (1995) Graphical interpretation of variance inflation factors. The American Statistician 49: 53–56.

110. R Core Team (2013) R: A Language and Environment for Statistical Computing. R Foundation for Statistical Computing, Vienna, Austria. URL `http://www.R-project.org/`. R package version 3.1.0.

111. Venables WN, Ripley BD, Venables W (1994) Modern applied statistics with S-PLUS, volume 250. Springer-verlag New York.

112. Klaus B, Strimmer K (2013) fdrtool: Estimation of (Local) False Discovery Rates and Higher Criticism. URL `http://CRAN.R-project.org/package=fdrtool`. R package version 3.1.0.

113. Strimmer K (2008) fdrtool: a versatile r package for estimating local and tail area-based false discovery rates. Bioinformatics 24: 1461–1462.

114. Heiberger RM, Holland B (2004) Statistical Analysis and Data Display: An Intermediate Course with Examples in S-Plus, R, and SAS. Springer-Verlag, New York, first edition. URL `http://springeronline.com/0-387-40270-5`.

115. Breheny P, Burchett W (2012) Visualization of Regression Models Using visreg. URL `myweb.uiowa.edu/pbreheny/publications/visreg.pdf`. R package version 3.1.0.

116. Zotev V, Yuan H, Phillips R, Bodurka J (2012) Eeg-assisted retrospective motion correction for fmri: E-remcor. NeuroImage 63: 698–712.

117. Allison PD (1977) Testing for interaction in multiple regression. American Journal of Sociology 83: 144.

118. Belmonte MK, Allen G, Beckel-Mitchener A, Boulanger LM, Carper RA, et al. (2004) Autism and abnormal development of brain connectivity. The Journal of Neuroscience 24: 9228–9231.

119. Courchesne E, Pierce K (2005) Why the frontal cortex in autism might be talking only to itself: local over-connectivity but long-distance disconnection. Current opinion in neurobiology 15: 225–230.

120. Jo HJ, Gotts SJ, Reynolds RC, Bandettini PA, Martin A, et al. (2013) Effective preprocessing procedures virtually eliminate distance-dependent motion artifacts in resting state fmri. Journal of applied mathematics 2013: 9.

121. Müller RA, Shih P, Keehn B, Deyoe JR, Leyden KM, et al. (2011) Underconnected, but how? a survey of functional connectivity mri studies in autism spectrum disorders. Cerebral Cortex 21: 2233–2243.

122. Murphy K, Birn RM, Handwerker DA, Jones TB, Bandettini PA (2009) The impact of global signal regression on resting state correlations: are anti-correlated networks introduced? Neuroimage 44: 893–905.

123. Spisák T, Jakab A, Kis SA, Opposits G, Berényi E, et al. (2013) Lost in translation: voxel-wise motion artifacts in population-level whole brain connectivity analysis of resting-state fmri. Magn Reson Mat Phys Biol Med 26: 302-404.

List of Publications

Peer-reviewed publications

1. Spisák, T., Jakab, A., Kis, S.A., Opposits, G., Aranyi, C., Berényi, E., Emri, M.: Voxel-Wise Motion Artifacts in Population-Level Brain Connectivity Analysis of Resting-State fMRI. PLOS ONE. 9 (9), e10494, 2014. EISSN: 1932-6203. DOI: http://dx.doi.org/10.1371/journal.pone.0104947
IF:3.534 (2014)

2. Jakab, A., Emri, M., **Spisák, T.**, Szemán-Nagy, A., Béres, M., Kis, S.A., Molnár, P., Berényi, E.: Autistic Traits in Neurotypical Adults: Correlates of Graph Theoretical Functional Network Topology and White Matter Anisotropy Patterns. PLoS One. 8 (4), e60982, 2013. EISSN: 1932-6203. DOI: http://dx.doi.org/10.1371/journal.pone.0060982
IF:3.534 (2013)

3. Clemens, B., Puskás, S., Besenyei, M., **Spisák, T.**, Opposits, G., Hollódy, K., Fogarasi, A., Fekete, I., Emri, M.: Neurophysiology of juvenile myoclonic epilepsy:EEG-based network and graph analysis of the interictal and immediate preictal states. Epilepsy Res. 106 (3), 357-369, 2013. ISSN: 0920-1211. DOI: http://dx.doi.org/10.1016/j.eplepsyres.2013.06.017
IF:2.19

4. Clemens, B., Puskás, S., Besenyei, M., Kovács, N.Z., **Spisák, T.**, Kis, S.A., Emri, M., Hollódy, K., Fogarasi, A., Kondákor, I., Fekete, I.: Valproate treatment normalizes EEG functional connectivity in successfully treated idiopathic generalized epilepsy patients. Epilepsy Res. 108 (10), 1896-1903, 2014. ISSN: 0920-1211.
DOI: http://dx.doi.org/org/10.1016/j.eplepsyres.2014.09.032
IF:2.19 (2014)

5. Clemens, B., Puskás, S., Bessenyei, M., Emri, M., **Spisák, T.**, Koselák, M., Hollódy, K., Fogarasi, A., Kondákor, I., Füle, K., Fekete, I.: EEG functional connectivity of the intrahemispheric cortico-cortical network of idiopathic generalized epilepsy. Epilepsy Res. 96 (1-2), 11-23, 2011. ISSN: 0920-1211.
DOI: http://dx.doi.org/10.1016/j.eplepsyres.2011.04.011
IF:2.29 (2011)

6. Piros, P., Puskás, S., Emri, M., Opposits, G., **Spisák, T.**, Fekete,

I., Clemens, B.: Uppermost synchronized generators of spike-wave activity are localized in limbic cortical areas in late- onset absence status epilepticus. Seizure. 23 (3), 213-221, 2014. ISSN: 1059-1311.
DOI: http://dx.doi.org/10.1016/j.seizure.2013.11.017.
IF:2.059 (2014)

7. Clemens, B., Puskás, S., Besenyei, M., **Spisák, T.**, Emri, M., Fekete, I.: Remission of benign epilepsy with rolandic spikes: An EEG-based connectivity study at the onset of the disease and at remission. Epilepsy Res. 106 (1-2), 128-135, 2013. ISSN: 0920-1211.
DOI: http://dx.doi.org/10.1016/j.eplepsyres.2013.04.006
IF:2.19

Conference proceedings

8. **Spisák, T.**, Ossenblok, P., Colon, A., Compagner, W., Kis SA., Opposits, G., Emri, M.: Individual functional statistical parametric networks related to interictal epileptic EEG discharges: a dynamic sliding-window study In: Electronic presentation online system : ECR Congress 2014 Ed.: ESR, European ociety of Radiology, [S. l.] C-2088, 2014. 10.1594/ecr2014/C-2088

9. **Spisák, T.**, Opposits, G., Kis, S.A., Pohubi, L., Jakab, A., Puskás, S., Clemens, B., Emri, M.: BrainCON: Graph theory based multimodal brain connectivity analysis and visualization software. In: Electronic presentation online system: ECR Congress 2013. Ed.: ESR, European Society of Radiology, [S. l.], C-2588, 2013.
DOI: http://dx.doi.org/10.1594/ecr2013/C-2588

10. **Spisák, T.**, Opposits, G., Kis, S.A., Lajtos, I., Krizsán, Á., Pohubi, L., Balkay, L., Emri, M.: BrainMOD:4-dimensional multimodal medical image analysis software. In: Electronic presentation online system: ECR Congress 2013. Ed.: ESR, European Society of Radiology, [S. l.], C-2586, 2013. DOI: http://dx.doi.org/10.1594/ecr2013/C-2586

Publication in Hungarian

11. Lajtos I., Emri M., Trón L., Kis S.A., Opposits G., Márián T., Trencsényi G., Mikecz P., **Spisák T.**, Krizsán Á.K.: A debreceni kisállat

PET program eredményei: A MiniPET-1, MiniPET-2 és a MiniPET-3 kamerák leképezési tulajdonságai. IME. 12 (különszám), 33-38, 2013. ISSN: 1588-6387.

Conference abstracts

12. Ossenblok, P., Hermans, K., **Spisak, T.**, de Munck, J., van Houdt, P., Colon, A., Boon, P. Clinical value of simultaneous EEG and functional MRI for Epilepsy Diagnosis and treatment EPILEPSIA 55:(2) p. 232. 1 p. (2014) 11th European Congress on Epileptology.

13. **Spisák, T.**, Jakab, A., Opposits, G., Kis, S.A., Berényi, E.L., Emri, M.: Lost in translation: Voxel- wise confounding effects of motion in resting-state fMRI and whole brain connectivity analysis. Magn. Reson. Mat. Phys. Biol. Med. 26 (S1), 302-404, 2013. ISSN: 0968-5243. DOI: http://dx.doi.org/10.1007/s10334-013-0384-5

14. Jakab, A., **Spisák, T.**, Berényi, E.L., Emri, M.: Graph theoretical analysis of brain network efficiency and centrality in autism spectrum disorders: A multi-center study. Magn. Reson. Mat. Phys. Biol. Med. 26 (S1), 337, 2013. ISSN: 0968-5243. DOI: http://dx.doi.org/10.1007/s10334-013-0384-5

15. **Spisák, T.**, Opposits, G., Kis, S.A., Clemens, B., Emri, M.: BrainCON: Software tool for graph theory based multimodal brain connectivity analysis and visualization. Magn. Reson. Mat. Phys. Biol. Med. 25 (S1), 616, 2012. ISSN: 0968-5243.

16. **Spisák, T.**, Koselák, M., Opposits, G., Kis, S.A., Trón, L., Jakab, A., Berényi, E., Emri, M.: Digital brain atlas assisted localization software for individual and population analysis of SPECT and PET data. Eur. J. Nucl. Med. Mol. Imaging. 38 (Suppl. 2), S258. p., 2011. ISSN: 1619-7070. DOI: http://dx.doi.org/10.1007/s00259-011-1910-1

17. Koselák, M., **Spisák, T.**, Kis, S.A., Lajtos, I., Opposits, G., Galuska, L., Hascsi, Z., Szabó, P., Emri, M.: Development of a multiparametric surface model for interventions supported by virtual bronchoscopy. Eur. J. Nucl. Med. Mol. Imaging. 38 (Suppl. 2), S280, 2011. ISSN: 1619-7070. DOI: http://dx.doi.org/10.1007/s00259-011-1911-0

18. Kis, S.A., Opposits, G., Lajtos, I., **Spisák, T.**, Balkay, L., Kovács, G., Trón, L., Emri, M.: Comparative analysis of image processing algorithms on quadratic and hexagonal grids. Eur. J. Nucl. Med. Mol. Imaging. 38 (Suppl. 2), S275. p., 2011. ISSN: 1619-7070. DOI: http://dx.doi.org/10.1007/s00259-011-1911-0

19. Opposits, G., **Spisák, T.**, Lajtos, I., Pohubi, L., Galuska, L., Jakab, A., Berényi, E., Emri, M.: Automated region analysis of brain PET examinations. Eur. J. Nucl. Med. Mol. Imaging. 38 (Suppl. 2), S333. p., 2011. ISSN: 1619-7070. DOI: http://dx.doi.org/10.1007/s00259-011-1911-0

20. **Spisák, T.**, Kis, S.A., Opposits, G., Lajtos, I., Pohubi, L., Balkay, L., Emri, M.: Surfaces, atlases, and other advanced imaging techniques in the ervice of nuclear medicine. Nucl. Med. Rev. Cent. E. Eur. 16 (Suppl. A), A16-A16, 2013. ISSN: 1506-9680.

21. Kis, S.A., Vincze, C., Opposits, G., Lajtos, I., Balkay, L., **Spisák, T.**, Galuska, L., Emri, M.: Methodology development of FDG-PET/CT based diagnosis of crohn disease. Nucl. Med. Rev. Cent. E. Eur. 16 (Suppl. A), A12-A12, 2013. ISSN: 1506-9680.

22. **Spisák, T.**, Kis, S.A., Opposits, G., Lajtos, I., Balkay, L., Emri, M.: BrainMOD:4-dimensional multimodal medical image analysis software. Magn. Reson. Mat. Phys. Biol. Med. 25 (S1), 619, 2012. ISSN: 0968-5243.

23. Jakab, A., **Spisák, T.**, Szemán-Nagy, A., Dobrai, D., Molnár, P., Berényi, E., Emri, M.: Pathological patterns of functional and structural brain connectivity in high functioning autistic adults. Magn. Reson. Mat. Phys. Biol. Med. 25 (S1), 27, 2012. ISSN: 0968-5243.

24. Opposits, G., **Spisák, T.**, Koselák, M., Pohubi, L., Galuska, L., Jakab, A., Berényi, E., Emri, M.: Methodological developments for automated region analysis of brain SPECT and PET examination. Nucl. Med. Rev. 14 (Suppl. A), A22, 2011. ISSN: 1506-9680.

25. Jakab, A., Béres, M., **Spisák, T.**, Kis, S.A., Emri, M., Berényi, E.: Handedness and interhemispheric differences in the anatomical connectivity of perisylvian language areas: A network-based approach. Magn. Reson. Mater. Phy. 24 (Suppl. 1), 276. p., 2011. ISSN: 0968-5243.

26. **Spisák, T.**, Koselák, M., Opposits, G., Kis, S.A., Trón, L., Jakab, A., Berényi, E., Emri, M.: Region management toolkit for atlas-space image processing. Magn. Reson. Mater. Phy. 24 (Suppl. 1), 543-543, 2011. ISSN: 0968-5243.

27. Spisák, T., Opposits, G., Jakab, A., Koselák, M., Kis, S.A., Trón, L., Berényi, E., Emri, M.: Anatomical localization software for individual and population analysis of PET data. Nucl. Med. Rev. Cent. East. Eur. 14 (Suppl. A.), A15. p., 2011. ISSN: 1506-9680.

28. Spisák, T., Koselák, M., Opposits, G., Kis, S.A., Galuska, L., Emri, M.: Registration of low-dose and diagnostic chest CT scans based on skeletal and bronchus surface models. Nucl. Med. Rev. Cent. East. Eur. 14 (Suppl. A.), A21. p., 2011. ISSN: 1506-9680.

29. Koselák, M., **Spisák, T.**, Opposits, G., Kis, S.A., Pohubi, L., Galuska, L., Hascsi, Z., Szabó, P., Emri, M.: Towards the clinical application of bronchoscopy supported by virtual planning: First results. Nucl. Med. Rev. Cent. East. Eur. 14 (Suppl. A.), A14-A15, 2011. ISSN: 1506-9680.

30. Emri, M., Kis, S.A., Koselák, M., Opposits, G., Mikecz, P., **Spisák, T.**, Trón, L.: Graph theoretical modeling of brain connectivity using perfusion PET data. Nucl. Med. Rev. Cent. East. Eur. 14 (Suppl. A.), A15. p., 2011. ISSN: 1506-9680.

31. Megyesi, Z., **Spisák, T.**, Kis, S.A., Opposits, G., Balkay, L., Trón, L., Emri, M.: Anatomical localization in PET brain receptor studies. Nucl. Med. Rev. 12 (1), 48, 2009. ISSN: 1506-9680.

Manuscript under consideration

32. Spisák T., Pozsgay Zs., Dávid Sz., Kocsis P., Nyitrai G., Gajári D., Hegedűs N., Czurkó A., Complete Freund's adjuvant-induced central sesnitization in rats: an fMRI study, Pain (IF.:5.83), submitted, 2015..

Science Metrics

- Impact factor: 17,987
- Citations: 30
- Hirsch-index: 3

Appendix

A*I*. List of Brain Atlas Regions

Table 7. Brain atlas regions (left hemisphere)

ID	long name	side	short name	H-O atlas regions merged
1	Left Caudate	left	l-caud	Caudate,Accumbens
2	Cingulate Gyrus anterior division	left	l-cinga	
3	Frontal Medial Cortex	left	l-fmedc	
4	Operculum	left	l-operc	front-cent-pariet.
5	Frontal Orbital Cortex	left	l-forbc	
6	Frontal Pole	left	l-front	
7	Inferior Frontal Gyrus pars opercularis	left	l-inffrontgop	
8	Inferior Frontal Gyrus pars triangularis	left	l-inffrontgtri	
9	Juxtapositional Lobule Cortex	left	l-juxlob	
10	Middle Frontal Gyrus	left	l-mfg	
11	Paracingulate Gyrus	left	l-parcing	
12	Pre-frontal	left	l-prefront	
13	Subcallosal Cortex	left	l-subcall	
14	Superior Frontal Gyrus	left	l-sfg	
15	Insular Cortex	left	l-ins	
16	Cuneal Cortex	left	l-cun	
17	Calcarine Cortex	left	l-calc	intra-, suprac.
18	Lateral Occipital Cortex inferior division	left	l-latocinf	
19	Lingual Gyrus	left	l-ling	
20	Occipital Fusiform Gyrus	left	l-occfus	
21	Occipital Pole	left	l-occ	
22	Angular Gyrus	left	l-ang	
23	Cingulate Gyrus posterior division	left	l-cingpost	
24	Lateral Occipital Cortex superior division	left	l-latoccsup	
25	Postcentral Gyrus	left	l-postcent	
26	Precuneous Cortex	left	l-precun	
27	Superior Parietal Lobule	left	l-supparl	
28	Supramarginal Gyrus anterior division	left	l-smarga	
29	Supramarginal Gyrus posterior division	left	l-smargp	
30	Lentiform	left	l-lent	put. pall.
31	Superior Temporal Gyrus	left	l-stg	post, ant, Heschl
32	Inferior Temporal Gyrus	left	l-itg	post, ant
33	Inferior Temporal Gyrus temporooccipital	left	l-itgtempoc	
34	Amygdala	left	l-amyg	
35	Hippocampus	left	l-hip	
36	Middle Temporal Gyrus anterior division	left	l-mtgant	
37	Middle Temporal Gyrus posterior division	left	l-mtgpost	
38	Middle Temporal Gyrus temporooccipital	left	l-mtgtempoc	
39	Parahippocampal Gyrus	left	l-parhipc	post, ant.
40	Planum	left	l-plan	temporale, polare
41	Temporal Fusiform Cortex	left	l-tfus	ant, post
42	Temporal Occipital Fusiform Cortex	left	l-tofus	
43	Temporal Pole	left	l-temp	
44	Left Thalamus	left	l-thal	

Lateralization, and long and short names of brain atlas-based ROIs used for estimating regional BOLD and motion related measures. The sources of brain regions are the Harvard-Oxford Cortical and Subcortical brain atlases [105].

A*II.* Group Formation

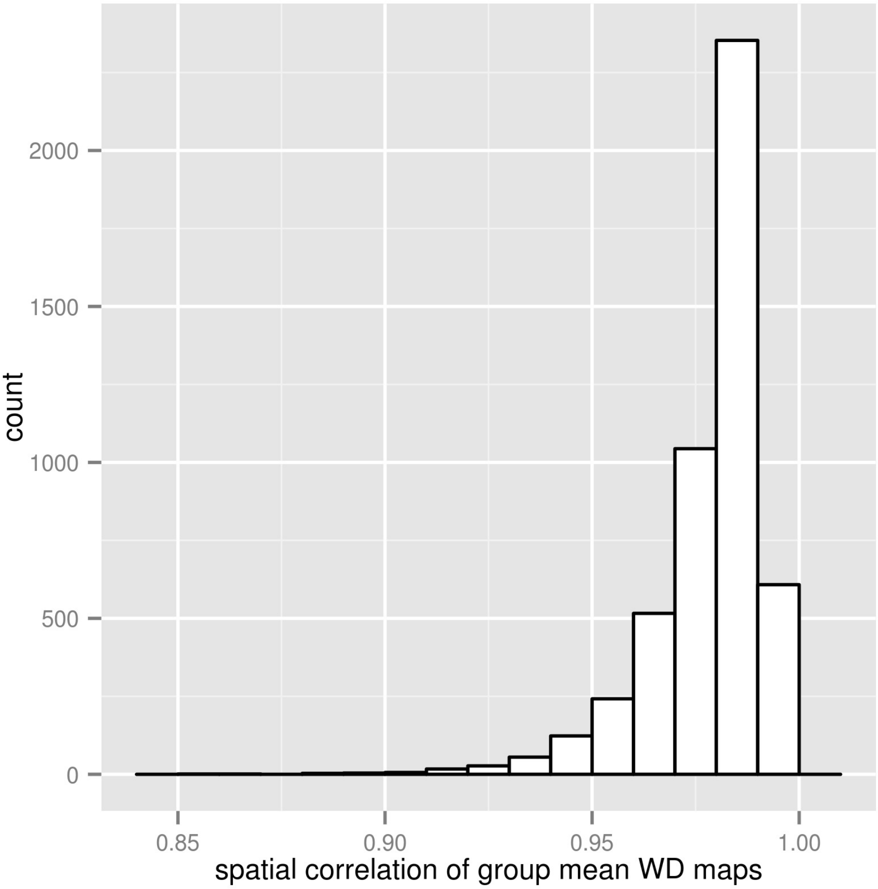

Figure 17. Histogram of group averaged voxel-wise displacement correlations based on 5000 random permutations

Temporally averaged standard-space voxel-wise displacement maps were averaged across the subjects of two randomly assigned groups. Spatial Pearson correlation was calculated between these group-mean voxel-wise displacement maps (ρ_{WD})). The histogram of this inter-group voxel-wise displacement correlation was computed based on 5000 random group formulation. Group-pairs with extrem inter-group differences in voxel-wise displacement were chosen for further analysis.

A*III.* BrainMOD software specification (ENIAC CSI project)

Goal of the software

The main goal of the software specified in this document is the interactive state of the art 2D and 3D visualization of post-processed multi-modal medical imaging data with aid of user-friendly graphical user interface. The imaging modalities involved are: PET, MRI, EEG, EIT. The visualization functionality should focus on techniques that can take advantage of multi-source post-processed data and help interpreting intra-modal relationships. Besides 2D and 3D visualization techniques, BrainMOD should also explicitly manage 4D datasets.

Relation to ENIAC CSI project

The above described purposes of BrainMOD are completely coherent with the Work Package Tasks 4.2.1, 4.3.1 and 4.3.3 of the ENIAC CSI project. The software will be developed as part of this project by the University of Debrecen (UNIDEB). The corresponding deliverable are: D4.2.2, D4.3.1 and D4.3.3. By it's dedicated components, BrainMOD is planned to integrate these tasks, deliverable and milestones and thus provide a general 3D smart system and create a decent connection between WPT1-3 and WPA1. Being an important element of the data processing pipeline of the project, below the points of contact (input and output) are clarified in details.

Input data

The input data of the software is produced by the image post-processing algorithms developed in WPT 1-3. Below we discuss the emerging input data formats in a logical grouping that reflects the functional architecture of the software. The necessary contributions with other consortium members are also highlighted.

Data exchange among project members In certain phases of the software development UNIDEB will need specific sample data for software design and testing. These data-sets can partly be substituted with data from the retrospective image database of UNIDEB but, in several cases, data exchange with project partners will be necessary. For this purpose UNIDEB offers it's on-line data tracking system available on the website *www.minipetct.com*.

Static volumetric data

Suggested file formats for static volumetric image data: Minc, **NIfTI**. DICOM file format is generally not supported. The conversion should be performed using command line utilities.

MR The software should support the input of T1 and T2 weighted MR images in the above mentioned file formats. The sample data needed under the development can be substituted from UNIDEB image database, except one case: for the simultaneous visualization of MR and EEG/EIT, data in common space is needed which will be provided by the University of Bologna **(UNIBO)** (WPT ?, WPT 4.3.1). [see also 6]

PET File input for reconstructed static PET volumetric image data. The data is assumed to be registered into the MR-space. The data needed by development can be substituted from UNIDEB image database.

fMRI activation map The software should provide a file input component dedicated for fMRI activation maps created with General Linear Model (GLM) and Independent Component Analysis (ICA). In case of GLM-based parametric maps, the type of statistical analysis and the degree-of-freedom can also be loaded into the software

	Format	**UNIDEB**	**UNIBO**
static vol.	NIfTI	PET, struct. MR, fMRI/GLM activation map	struct MR fitted with EEG space, segmented MRI label map, EIT (if frequency dependent, put it to vol. series)
vol. series	NIfTI	dyn PET,fMRI time-series,fMRI/ICA	fMRI time-series
	?		LORETA, sLORETA
curves	csv	dynPET tissue, ICA time-course	-
VOI	M3I::Voi	BrainMOD output	-
	NIfTI	-	label map generated by segmentation algorithm
Surface	M3I::Surf	BrainMOD output	-
	ply	-	-
Marker	csv	-	EEG marker file

	Format	**KEMP**	**ST**	**AIT**
static vol.	NIfTI	fMRI/GLM activation map	-	seizure localization map
vol. series	NIfTI	fMRI time-series, fMRI/ICA	-	source localization 4D
	?		-	-
curves	csv	ICA time-course	-	-
VOI	M3I::Voi	-	-	-
	NIfTI		label map generated by segmentation algorithm	
Surface	M3I::Surf	-	-	-
	ply	-	MR-based brain surface	-
Marker	csv	-	-	-

Table 8. Partner I/O data requirements

for statistical thresholding of functional parametric maps. In case of ICA-based component maps the software should load and manage the components together, as a serial volumetric image-series [6]. The time-courses corresponding to the components should also be able to load as simple text files [6]. The data needed for the development can be partly substituted from UNIDEB image database. Additionally, data may be needed from **UNIBO** and Kempenhaeghe **(KEMP)**.

EEG/EIT-based static functional maps Input of functional map images derived from EEG measurements. For image fusion functionality, the data is excepted to be in the same space as the MRI data sets. [see 6] LORETA and sLORETA sample data needed from **UNIBO** and source localization maps needed from **AIT**.

Volumetric series data Suggested file formats for dynamic volumetric image data: **4D NIfTI**, set of 3D NIfTI or Minc files. DICOM file format is generally not supported. The conversion should be performed using command line utilities.

Dynamic PET Input of dynamic PET data as a single 4D volumetric image file or as set of 3D volumetric image files. The data needed for development can be substituted from UNIDEB image database.

fMRI time-series Input of fMRI time-series data as a single 4D volumetric image file or as set of 3D volumetric image files. The data needed for development can be substituted from UNIDEB image database. Additionally, data may be needed from **UNIBO** and **KEMP**.

ICA component maps See 6.

LORETA, sLORETA More information needed from **UNIBO**.

Curves

Time-courses of ICA components The software should be able to load time courses of ICA components in simple text files [6] being part of an ICA-analysis.

Other curves Input of various curves generated by other applications as text files (comma separated values, csv). Input of curves generated within the BrainMOD.

Volumes-of-Interests

Labeled volumetric data The software should be able to load the results of segmentation algorithms developed by STMicroelectronics (**ST**), **UNIBO**, Politechnico di Torino **(POLITO)** in WPT 4. as labeled volumetric data in Minc or NIfTI file formats. Based on these, the software should be able to generate polygon based Regions- and Volumes-of Interests.

M3I Voi data format Volumes-of-Interests created in BrainMOD should be able to save [6] and re-load later in the software's own format.

Three-dimensional surfaces

The software should be able to load three-dimensional surfaces in .ply file format and in it's own format. The surfaces to load must be triangle-based. For the .ply input components, sample data is needed from **ST**.

Markers

Input of three-dimensional marker points stored in some simple text format. Marker points can represent electrode positions for EEG/EIT visualization, thus sample data from **UNIBO** is needed for clarifying the attributes describing such markers.

Output data

According to the requirements, the most important output of the software is it's visualization feature. The 2D and 3D views processed by the software should be able to be saved as .png, .tiff and .jpg file format. The opportunity for generating .pdf report regarding certain visualization features should also be available. BrainMOD should be able to save Volume-of-Interests based statistical image parameters as comma separated values (.csv) files. A Volume-of-Interests itself should be able to be saved either in the software's own format (.voi) or as binary volume mask in NIfTI format. The software should have an output for curves generated from 4D image data. The suggested file formats are: csv (for export) and the software's own format.

Functional requirements

2D image display

The software should provide a triplanar drawport for visualizing the axial, coronal and sagittal planes of static volumetric image data. The image data can be displayed in color-index mode using different color palettes. (grayscale, blue, red, hotmetal, spectral) Two-tailed palettes can also be used to simultaneously highlight negative and positive activation patterns. The color-index identification can be changed by setting the minimal and maximal palette thresholds to the appropriate values. These thresholds define intensity windows which can be saved for further use in the software. The palettes can be inverted and also switched into 'print mode' when creating screenshots or exporting pdf report for printing. The cursor position is displayed in voxel and world coordinates.

The software should also be able to display the fusion view of two images being in the same space, with a changeable blending.

Volume-of-Interests toolkit

The Volume-of-Interests toolkit should provide means for manually (freehand, polygon, circle, etc) and automatically (isocontour) delineate Volumes-of-Interests (VOIs) and display them with different colors, line widths and text labels. Binary volume masks and label volumes can also be transformed to VOIs and vica versa. Contours delineated on the axial plane can be displayed on the coronal and sagittal plane, as well. Set operations like union, intersection etc. can also be performed on VOIs.

Marker toolkit

The software should visualize 3D marker points in 2D and 3D mode, as well. The marker points can be easily loaded, created and deleted within the software. A marker point, aside of it's three-dimensional coordinates, can have several other attributes, like name and various (temporal) parameters.

Toolkit for serialized volumetric data

4D volumetric image (eg. frequency dependent LORETA, fMRI time-series, ICA component maps) data sets can be loaded and visualized within the software. The actual frame currently displayed can be changed independently for every data set. The temporal/frequency/model dimension of the data can be plotted as curve diagram. The spatial source of the curves can be a single voxel, a voxel environment (eg. sphere) or a VOI. The mean and standard deviation of the source is computed on the whole 4D series and plotted as a curve. Various curves of different data-sets can be plotted simultaneously. Basic operations on curves (like sum, resampling, smoothing, filters, correlation) can also be performed.

3D surface visualization

BrainMOD should be able to visualize 3D surfaces represented as polyhedra. Organizing the surfaces into layers should provide an easy management of surface sets. Enhanced blending and shading techniques ensure the easy discovering of overlapping elements. VOIs can be transformed to polyhedra and visualized in 3D. Marker points can be displayed in 3D space as spheres with variable radius.

Surfaces can be split with axial, coronal, sagittal and oblique cutting planes where the corresponding 2D slices of volumetric image data can be observed, too. All types of surfaces and markers can be displayed with arbitrary solid color.

Multiparametric surfaces

Using surfaces, structural properties and boundaries can be effectively visualized, however, functional properties being located under the surface are hard to observe. Here we suggest a multiparametric surface coloring technique which for every surface vertex, performs a 3D sampling in the direction of the normal vector or it's negative. After arbitrary computations, parameters of multiple samples can be visualized on the surface. Surface parameters can have a temporal dimension extracted from dynamic volumetric data. Using this approach, dynamic properties can be visualized effectively in 3D. Considering the vast number of vertices in a detailed, smooth surface, the parallelization of the surface parametrization algorithm should be necessary for effective real-time visualization.

Hardware requirements

The minimal (optimal) hardware requirements for the software are:

- 2Gb (4Gb) RAM
- GPU (Nvidia GPU) with OpenGL 2.0 support

- 2GHz (¿2GHz) processor
- 50 Mb (100 Mb) free disk space

Implementation details

The software will be developed based on the MultiModal Medical Imaging (M3I, www.minipetct.com/m3i) software library system in ANSI ISO C++. The 2D and 3D visualization components will be developed based on OpenGL 2.0. The user-friendly graphical user interface components will be developed using Qt. The development will be performed in 64-bit LINUX environment, o`n PCs` supplied with Nvidia GPUs. The testing will be performed on LINUX, Windows Xp and Windows 7 operating systems both on 32 and 64-bit architectures.

Release details

The software will be released as Linux Debian package and as InnoSetup-based install kit for Windows Xp and Windows 7. Install kits and packages for these operating systems will be available for both 32 and 64-bit architectures. Release data will be available on the Institutional (UNIDEB) R&D website: www.minipetct.com/brainmod for consortium partners.